Organic Light Emitting Diodes: Electron Injection Layers for Advanced Solution Processed Device Architectures

Zur Erlangung des akademischen Grades eines

DOKTOR-INGENIEURS

von der Fakultät für

Elektrotechnik und Informationstechnik

des Karlsruher Instituts für Technologie (KIT)

genehmigte

Dissertation

von

M.Sc. Min Zhang

geb. in Shandong, China

Tag der mündlichen Prüfung:	29.Mai 2018
Hauptreferent:	Priv.-Doz. Dr.-Ing. Alexander Colsmann
Korreferent:	Prof. Dr. rer. nat. Michael Siegel

Kurzfassung

Organische Leuchtdioden (OLEDs) drängen heutzutage mit kommerziellen Produkten wie Smartphones und Fernsehern auf den Markt. Die Herstellungskosten der Bildschirme sind jedoch immer noch relativ hoch aufgrund von vielfachen Vakuumdepositionsschritten. Aus diesem Grund werden Prozesse für die flüssigprozessierte Herstellung, z.B. mittels Rolle-zu-Rolle Druckverfahren, benötigt. Ein solcher Druckprozess gilt als geeigneter für die Massenproduktion und Herstellung von großflächigen Geräten. Neben der Emissionsschicht benötigen effiziente OLEDs Ladungsträgerinjektionsschichten. Solche Schichtstapel mittels Flüssigprozessierungsverfahren herzustellen ist jedoch schwierig, da die Lösemittel, die zur Herstellung einer Schicht verwendet werden, in die darunterliegende Schicht gelangen und diese teilweise auflösen können. So ist insbesondere die Auswahl von flüssigprozessierbaren Elektroneninjektionsschichten (EILs) begrenzt, da Materialien mit niedriger Austrittsarbeit nicht in Umgebungsatmosphäre stabil sind.

In dieser Arbeit werden drei Typen von flüssigprozessierten EILs demonstriert, welche fortschrittliche OLED-Architekturen ermöglichen. Eine Doppelschicht mit niedriger Austrittsarbeit, bestehend aus einem Metalloxid (ZrO_2:Y) und einem Oberflächenmodifikator (PEI), ermöglicht effiziente Single-Junction OLEDs. Aufgrund ihrer Stabilität in schwach sauren Umgebungen wird darüber hinaus eine ZrO_2:Y/PEI Mischschicht in einer universellen Ladungsträgergenerationsschicht (CGL) in Tandem OLEDs, die wiederum aus zwei lichtemittierenden Einheiten bestehen, untersucht. Tandem OLEDs sind sehr vielversprechende Bauteilarchitekturen da diese die externe Quanteneffizienz verdoppeln können und es erlauben, zwei verschiedene Farben miteinander zu kombinieren. Um die gleiche Leuchtdichte zu erreichen wird in der Tandem OLED nur der halbe Strom benötigt wie in einer entsprechenden Single-Junction OLED. Der verringerte Strom führt in der Tandem OLED zu einer Verlangsamung der Degradation und damit zu einer verlängerten Lebensdauer. Durch geschickte Wahl der funktionellen Materialien und Lösemittel wurden invertierte und reguläre Tandem OLED Architekturen mit bis zu 11 flüssigprozessierten Schichten entwickelt. Neben kommerziell verfügbaren fluoreszenten Polymeren werden phosphoreszente Kleinmoleküle und TADF Kupfer(I) Komplexe erfolgreich in diese Architekturen integriert.

Zusätzlich zur Entwicklung von ausgefeilten Tandem OLED Architekturen mit ZrO_2:Y/PEI Mischschichten wird eine simple Methode zur Herstellung eines Materials

mit niedriger Austrittsarbeit demonstriert bei der CsF zu den Metalloxiden ZnO, ZrO_2 und ZrO_2:Y hinzugegeben wird. Diese einfachen EILs ermöglichen effiziente Ladungsträgerinjektion in alle untersuchten Emissionsschichten.

Aufgrund der geringen Stabilität von CsF wird ein weiterer Ansatz untersucht EILs mit geringer Austrittsarbeit herzustellen. Dabei wird PEI mit den Metalloxiden ZnO und ZrO_2 gemischt. Die Eignung dieser Mischungen als Elektroneninjektoren wird in verschiedenen OLED-Architekturen überprüft, unter anderem in transparenten OLEDs in denen Anoden mit hoher Austrittsarbeit, bestehend aus PEDOT:PSS und PFI verwendet werden. Durch die geringen benötigten Prozesstemperaturen wird darüber hinaus die Bauteilherstellung auf mechanisch flexiblen Kunststoffsubstraten erfolgreich demonstriert.

Abstract

These days organic light emitting diodes (OLEDs) enter the market with commercial products such as smartphones or TV displays. The fabrication costs of the displays, however, are still rather high due to multiple thermal vacuum deposition steps. Therefore, processes for OLED displays to be fabricated from solution, e.g. by roll-to-roll printing, are needed. Printing process is considered more facile for mass production and fabrication of large-area devices which could significantly reduce the production costs. Besides the emission layer, efficient OLEDs require charge carrier injection layers. Fabricating such layer stacks by solution processes, however, is difficult since the solvents used for the following layers might penetrate into the previously deposited layers, and partially dissolve them. In particular, the choices of solution processable electron injection layers (EILs) are limited since low work function materials are not stable in ambient atmosphere.

In this thesis, three types of solution processed EILs are proposed, which enable advanced OLED architectures. A low work function bilayer formed from a metal oxide (ZrO_2:Y) and a surface modifier (PEI) enables efficient single junction OLEDs. Due to its stability in weak acidic environments, ZrO_2:Y/PEI bilayer is also investigated in a universal charge carrier generation layer (CGL) in tandem OLEDs with two light emitting units. Tandem OLEDs are promising architectures due to the doubled external quantum efficiencies and the possibility to combine two different colors. To obtain the same luminance, the current in the tandem OLED is only half of the current of the single junction OLED. The lower current in the tandem OLED slows down the device degradation and enhances the lifetime of the tandem OLED. By carefully choosing the functional materials and solvents, inverted and regular tandem OLED architectures with up to 11 solution-processed layers are developed. Besides commercially available fluorescent polymers, phosphorescent small molecules and TADF copper(I) complexes are successfully incorporated into these architectures.

In addition to the development of the sophisticated tandem OLED architectures with the ZrO_2:Y/PEI bilayer, a facile method to produce a low work function material is proposed by adding CsF into the metal oxides, ZnO, ZrO_2 and ZrO_2:Y. These simple EILs enable efficient charge carrier injection into all investigated emission layers.

Due to the poor stability of CsF, another approach to produce low work function EILs is investigated, where PEI is blended with the metal oxides, ZnO and ZrO_2. The electron

injection ability of the mixtures is verified in various OLED architectures, including transparent OLEDs, in which a high work function anode comprising PEDOT:PSS and PFI is incorporated. Due to the low annealing temperatures of all fabrication steps, the device fabrication on plastic substrates is also successfully demonstrated.

Contents

1 Introduction

Organic semiconductors have the electronic properties of semiconductor materials as well as chemical and mechanical flexibilities of organic compounds. Like other semiconductor materials, organic semiconductors are capable of absorbing photons, conducting charges and emitting light. Meanwhile, the chemical structures can be adjusted to render desired properties, for instance, to emit at a desired wavelength or to be soluble in specific solvents. These characteristics of organic semiconductors have driven investigations towards their applications in organic solar cells, organic filed effect transistors (OFETs), organic lasers and organic light emitting diodes (OLEDs). Ever since C.W. Tang and S.A. VanSlyke observed electroluminescence from amorphous film in 1987, development of OLEDs has never been stopped.[1]

Most cellphones and TVs on the market still incorporate liquid crystal displays (LCDs). Yet, LCDs require a constant backlight illumination with a high energy consumption. On the other hand, the pixels within an active matrix OLED (AMOLED) displays are self emitting. Therefore OLED displays can be more energy efficient. Additionally, such active matrix displays exhibit a superior white-to-black contrast. The thicknesses of all functional layers in the device are in the nanometer range, hence, the whole display can be ultra-thin and lightweight. All these benefits of OLEDs over the traditional LCD panels have facilitated their commercialization. As the new generation of lighting technology, analysts are optimistic about OLEDs. A market prediction from IHS Markit, shown in Figure 1.1, clearly demonstrates the strong faith in the OLED display market. They believe in further revenue increase of AMOLED displays, driven by the high demand of smartphones in the following years.[2] Another unique advantage of OLEDs is that they can be fabricated on flexible substrates. Therefore they enable flexible and foldable smartphones and televisions. One example is demonstrated in Figure 1.2a.[3] Other than OLED displays, general luminaire with customized designs can also be realized with OLEDs (Figure 1.2b).[4]

At present, most OLED panels, incorporated into smartphones and TVs, are fabricated via thermal evaporation. This traditional fabrication process enables the sequential deposition of functional layers. Yet, this manufacturing approach suffers from some disadvantages. For instance, part of the material is wasted on the evaporation chamber during deposition. Another shortcoming is that usually a high vacuum is required for the
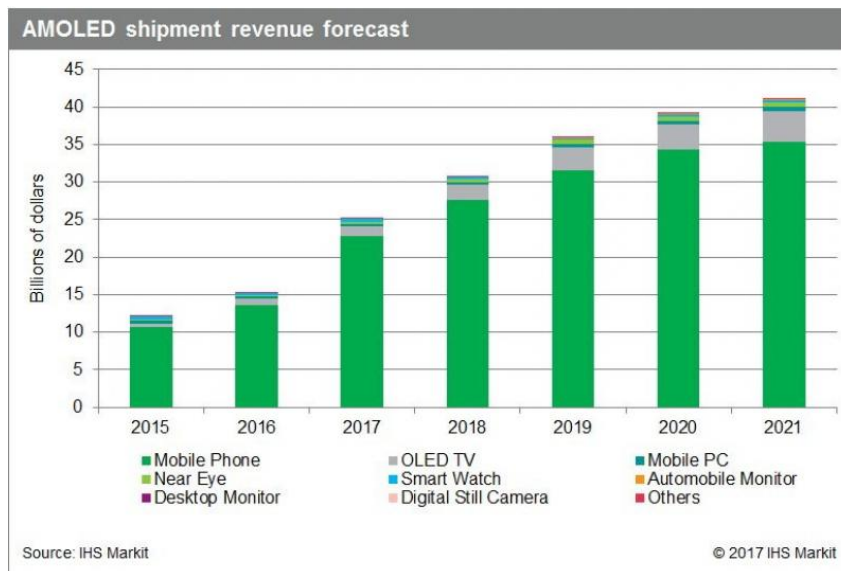
Figure 1.1: IHS Markit forecast on AMOLED revenue until 2021. It clearly indicates the increase of AMOLED market in the following years.[2]
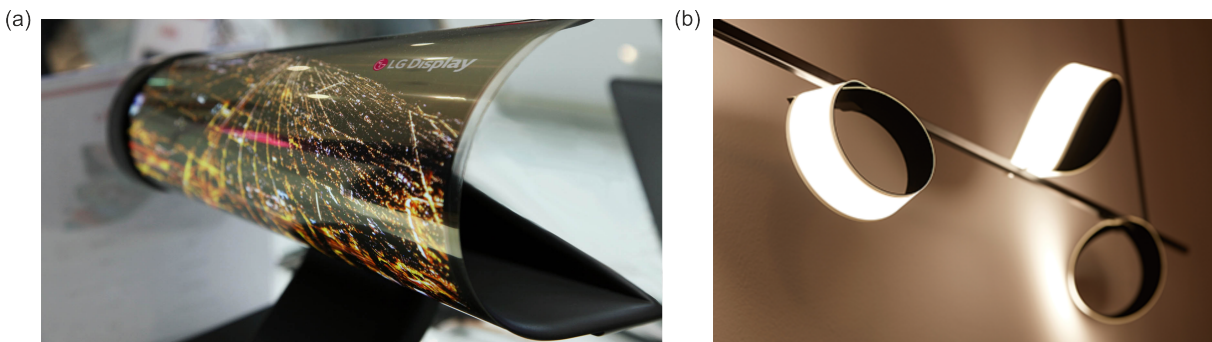

Figure 1.2: (a) LG demonstrated foldable TVs in 2016 at Consumer Electronics Show. (b) Commercially available OLED luminaires on flexible substrates.[3, 4]

layer deposition, increasing the fabrication costs. Difficulties in upscaling the devices to mid-sized and large devices arise due to, for example, the fineness of evaporation mask and film uniformity.

Another approach for OLED panel fabrication is to apply OLED materials onto the substrate via printing technique, such as reel-to-reel coating, which can be adapted from the fabrication of plastic foil or ink-jet printing. Due to the simplicity of this fabrication method, it can be easily applied for various sizes of OLED production. It is also widely considered as a low-cost manufacturing process since the material loss is significantly reduced. In addition, no need for a vacuum chamber and high temperatures reduce the production lead time. With all the advantages, one significant challenge of the printing process is that all materials must be soluble in solvents and the solvent used for the following layer must not dissolve the previously deposited film. The options for solution processed electron injection layers are limited because of the poor stability of low work

function materials in air. In this work, three approaches are demonstrated to form efficient electron injection layers, therefore enabling more advanced device architectures, such as tandem OLEDs and transparent flexible OLEDs.

One critical issue of OLED panels is their rather short lifetime. One approach to solve this issue is to develop tandem OLED architectures, where two sub-OLEDs are connected in series using a charge generation layer.[5, 6] Yet, the layer deposition in solution processed tandem architectures is challenging due to the high number of layers. In this work, inverted and regular tandem OLEDs, with up to eleven solution deposited layers are demonstrated by employing a novel electron injection layer. Through incorporation of various emitters, the universality of these OLED architectures is proven. The lifetime of the tandem device clearly exceeds that of the single junction OLED.

Efficient OLEDs usually require many functional layers, which increases the complexity of the fabrication. A way to solve this dilemma is to employ simplified functional layers. Two simple approaches to produce efficient electron injection materials are proposed here. Additionally, a simplified method to inject holes into the emitter without any hole injection material is presented. Consequently, simplified all-solution processed transparent OLEDs on flexible substrates are demonstrated with altogether four layers being spincoated on the substrate. Their efficiencies are among the best reported OLEDs with the same emissive layer.

2 Fundamentals of Organic Semiconductors

2.1 Electronic States

Organic compounds are materials which mostly consist of carbon and hydrogen atoms, sometimes oxygen, nitrogen or sulfur atoms are also included. Thus understanding the electronic structure of carbon is essential for organic electronics. Atomic carbon has six valence electrons in the ground state and its atomic orbitals are referred to as s and p orbitals depending on their angular momentum quantum number. The way to describe how electrons are distributed over orbitals is called configuration. The ground-state configuration of a carbon atom can be written as $1s^2 2s^2 2p_x^1 2p_y^1$, denoting that two electrons can be found in the 1s orbital, two in the 2s orbital, one in the $2p_x$ orbital and the last one in the $2p_y$ orbital. Therefore, carbon can form two covalent bonds. If other atoms such as hydrogen or another carbon approach one carbon atom, the external force is sufficient to compensate the energy difference between s and p orbitals, leading to the degeneration of s and p orbitals. Consequently new hybrid orbitals, which are linear combination of the s and p orbitals, are formed.[7]

If one 2s orbital mixes with three 2p orbitals, then the four identical sp^3 hybrid orbitals are formed. As demonstrated in Figure 2.1a, the hybridized sp^3 orbitals point to the four corners of a tetrahedron, with an angle of 109.5° between them. Like in Figure 2.1b, the mixing of one 2s orbital and two 2p orbitals result in three sp^2 orbitals on one plane. The angle between them is 120°, while the remaining 2p orbital is oriented perpendicular to this plane. There is also the situation that only one 2p orbital is mixed with the 2s orbital, then two hybrid sp orbitals at an angle of 180° are generated (see Figure 2.1c).

The hybrid orbitals and the remaining p orbitals in the carbon atom determine the bonds it can form. Taking methane (CH_4) as an example, four valence electrons are distributed over the four identical sp^3 hybrid orbitals. When the four sp^3 orbitals overlap with the s orbitals from four hydrogen atoms, each of the carbon's electrons can be paired with an electron from hydrogen. Then the paired electrons no longer belong to the single atom,
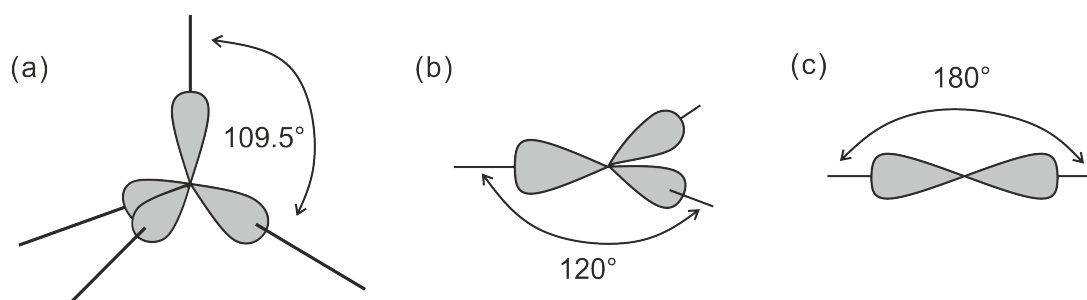
Figure 2.1: (a) In the sp^3 hybrid orbitals, the four orbitals are equivalent, pointing at the four corners of a tetrahedron. (b) Three hybrid sp^2 orbitals are in one plane with 120° between each other. (c) Two sp orbitals at an angle of 180° are formed from one s and one p orbitals.[7]

instead they are shared between the carbon and hydrogen atoms. The bond between the carbon and hydrogen atom is called C-H σ bond.

As demonstrated in Figure 2.2a, there are two carbon atoms and six hydrogen atoms in the ethane (C$_2$H$_6$) molecule. Each electron from a carbon atom can be paired with an electron from hydrogen or an electron from the other carbon's sp^3 orbital, resulting in six C-H σ bonds and one C-C σ bond.

In an ethylene (H$_2$C=CH$_2$) molecule (see Figure 2.2b), each carbon atom has three sp^2 and one remaining p orbitals. These two sp^2 orbitals overlap with the s orbitals from the two hydrogen atoms, resulting in two C-H σ bonds. The remaining sp^2 orbital from one carbon atom combines with the hybrid orbital from the other carbon, leading to one C-C σ bond. Thus one electron is still left in the unhybridized p orbital in each carbon atom. These two remaining p orbitals do sideways overlap, generating one new C-C π bond. Therefore the two carbon atoms are bound by one σ bond and one π bond. In acetylene (HC≡CH), two carbon atoms are joined by one σ and two π bonds.

Nevertheless, organic molecules consist of more than one atom, therefore molecular orbitals (MO) instead of atomic orbitals must be considered. The wavefunction of a molecular orbital can be estimated by the linear combination of atomic orbitals. Suppose that Φ_A and Φ_B represent the wavefunctions of two 1s atomic orbitals from two hydrogen atoms, when the atoms approach each other, the resulting molecular orbital of H$_2$ can be considered as a constructive interference of the two electron wavefunctions

$$\Phi_+ = c_A \Phi_A + c_B \Phi_B \tag{2.1}$$

where c_A and c_B are the respective weighting factors. The enhanced charge density between the atomic nuclei associated with this orbital leads to a bonding character, therefore it is also called bonding orbital. Yet, it is also possible that two wavefunctions
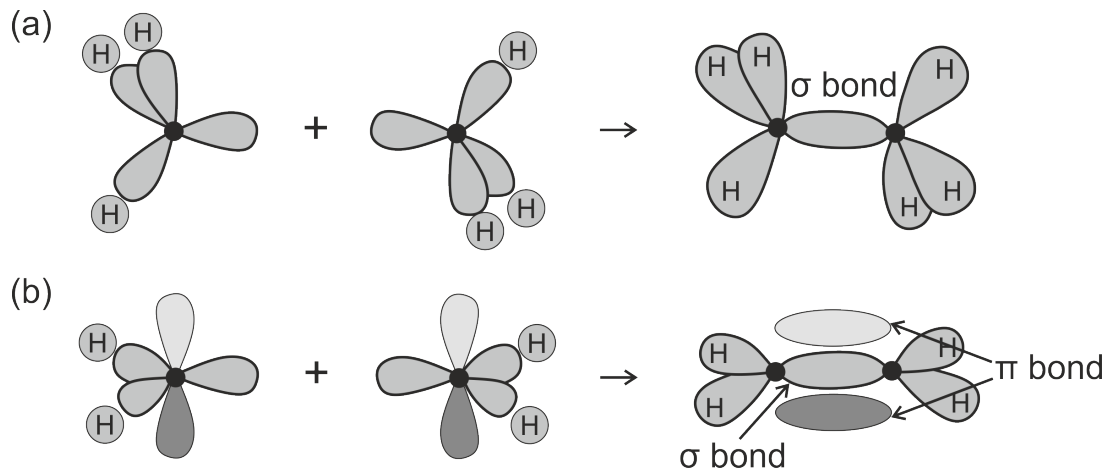
Figure 2.2: (a) In an ethane molecule (C_2H_6), three sp^3 hybrid orbitals of each carbon atom form three C-H σ bonds with three hydrogen atoms. The fourth sp^3 orbital from each carbon atom overlaps with its neighbor and form one C-C σ bond. (b) Each carbon atom in the ethylene ($H_2C=CH_2$) owns three sp^2 hybrid orbitals and one remaining p orbital. Two of three sp^2 orbitals form C-H σ bonds with hydrogen. The third hybrid orbital from each carbon atom leads to one C-C σ bond. The remaining p orbital of each carbon atom overlaps sideways to build a C-C π bond.[7]

interfere destructively with reduced charge carrier density between two nuclei. The new MO can be written as

$$\Phi_- = c_A \Phi_A - c_B \Phi_B \qquad (2.2)$$

This is referred to as antibonding orbital. The energy levels of the resulting molecular orbitals are different from the energies of Φ_A or Φ_B, with the orbital Φ_+ being at lower energy than Φ_-.[8]

In ethylene (C_2H_4) each carbon atom contains three degenerated $2sp^2$ orbitals and one remaining $2p_z$ orbital. The two carbon $2sp^2$ hybrid orbitals generate the bonding and the antibonding orbitals with two hydrogen 1s orbitals. The rest $2sp^2$ orbitals from each carbon generate σ and σ^* orbitals. The interaction of the remaining $2p_z$ orbitals takes place at some distance from the nuclei, thus leading to a weaker splitting between the bonding π and the antibonding π^* orbitals.[7] As shown in Figure 2.3, each carbon atom comprises one electron in $2p_z$ orbital, therefore these two electrons from two carbon atoms occupy the molecular orbitals with lower energy. Hence, π orbital is filled first and π^* orbital is left unoccupied. The full π orbital is therefore called highest occupied molecular orbital (HOMO) while the empty π^* orbital is referred to as the lowest unoccupied molecular orbital (LUMO). LUMO and HOMO of one molecule correspond to the conduction band and valence band in inorganic semiconductor, the gap between LUMO and HOMO is equivalent to the bandgap.

There are many compounds which contain bonding orbitals that spread over three or more atoms. In this case, such a bonding is delocalized. In benzene (C_6H_6), for example, two
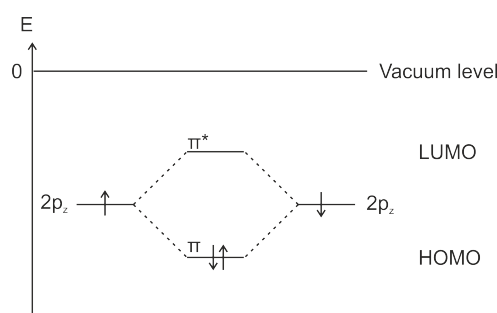
Figure 2.3: In ethylene molecule (C_2H_4), one of three hybridized sp^2 orbitals interacts with one sp^2 orbital from the other carbon atom, resulting in one σ and one σ^* orbitals. The two p_z orbitals from each carbon atom overlap and generate one π and one π^* orbitals. The bonding orbital always owns lower energy than the antibonding orbital. Since the electrons occupy the molecular orbitals with lower energy first, the π^* and σ^* orbitals formed from the 2p orbitals are left unoccupied. The filled π orbital is called HOMO and the vacant π^* orbital is referred to as LUMO.[7]

out of three sp^2 hybrid orbitals in each carbon atom form bonds with two other carbon atoms and the other sp^2 hybrid orbital builds bond with a hydrogen atom. The remaining p_z orbital in each carbon atom can overlap with the two adjacent p_z orbitals equally to form a π bonding, which means that this π orbital spreads over more atoms. This is called π conjugation. In benzene, these six electrons used to build π orbitals are delocalized and belong to six atoms. Therefore, a conjugated electron system is built.

2.2 Optical Properties

In the ground state, electrons occupy the energy levels at or below the HOMO, however, after absorbing a certain amount of energy, electrons can be promoted to higher energy levels. Accordingly, the electrons can transit from the HOMO or lower orbitals to the LUMO or higher orbitals. This electron transition leads to the molecule transition from the ground state to the excited state. The amount of energy to excite the molecule needs to be higher than the energy difference between the HOMO and LUMO. Therefore, if the photon energy equals the bandgap of the molecule, the light can be absorbed to promote electrons. The energy of a photon with wavelength λ can be calculated via

$$E = h\nu = hc/\lambda \tag{2.3}$$

where $\nu = c/\lambda$ is the frequency of light and h is Planck's constant.

Even for the same electronic state, there are various vibrational and rotational states since a molecule also vibrates and rotates. The energy difference between two adjacent vibrational states is much smaller than that between two adjacent electronic states. Rotational transitions are in orders of a few cm^{-1} and can not be resolved in line-narrowing
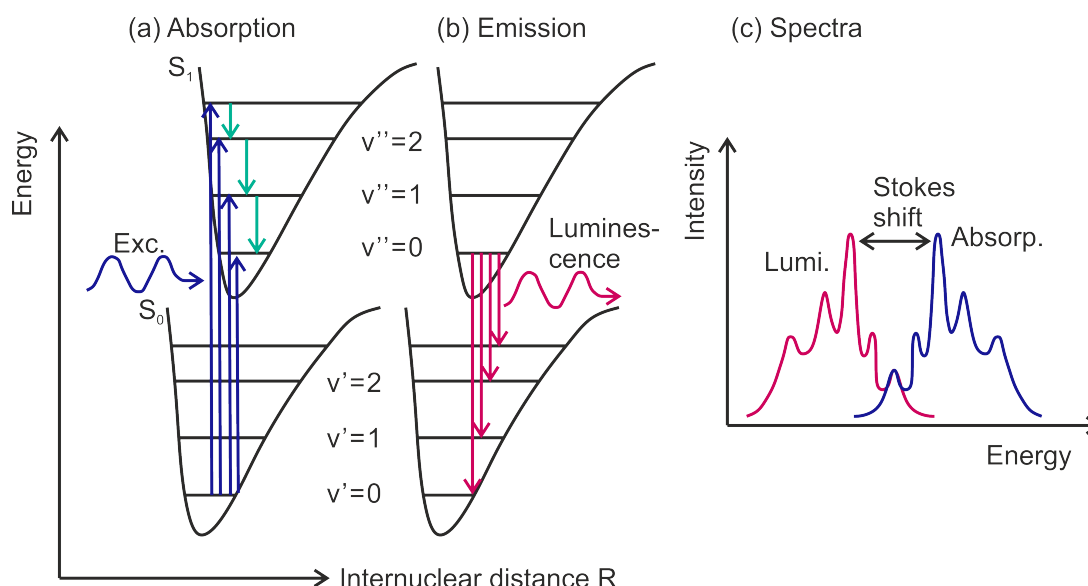
Figure 2.4: The state diagram shows the energy levels of the ground state S_0 and the first excited state S_1 in a molecule. There are different vibrational states at the same electronic state. (a) Absorption occurs between v' = 0 at S_0 and several vibrational states at S_1, followed by the vibrational relaxations. (b) The relaxations from the zeroth vibrational state of S_1 to the different vibrational states of ground state S_0 lead to luminescence. (c) The resulting absorption and emission intensity versus energy. The difference between the maximum of absorption and emission is the Stokes shift.[9]

methods and gas phase spectroscopy, therefore they are not indicated here.[7] The state diagram is depicted in Figure 2.4. Before the electronic transitions take place, vibrational relaxations from the excited vibrational states to the ground vibrational state occur. These processes are indicated by the green arrows in Figure 2.4a. Due to the existence of various vibrational and rotational states, the light with different wavelengths can be absorbed in one molecule.

As illustrated by the blue arrows in Figure 2.4a, the incident excitation light with various wavelengths results in molecular state transitions from the ground electronic state S_0 to the first excited state S_1. At room temperature, molecules often stay at the ground vibrational state of v' = 0. After absorbing energy, it can transit to different vibrational states in the first excited state, v' = 0 → v" = 0, v' = 0 → v" = 1 and v' = 0 → v" = 2. Thus in Figure 2.4c, there are various peaks in the absorption spectrum corresponding to different absorption.

Emission only happens from the zeroth vibrational level of S_1. The state transitions from S_1 to S_0 leads to light emission, including v" = 0 → v' = 0, v" = 0 → v' = 1 and v" = 0 → v' = 2. Thus, there are also several peaks in the emission spectrum associated with different vibrational states in S_0 (Figure 2.4c). The most probable transition causes the highest intensity peak in the spectra. There is an energy difference between the maximum of absorption and emission spectra and it is referred to as Stokes shift.[8]
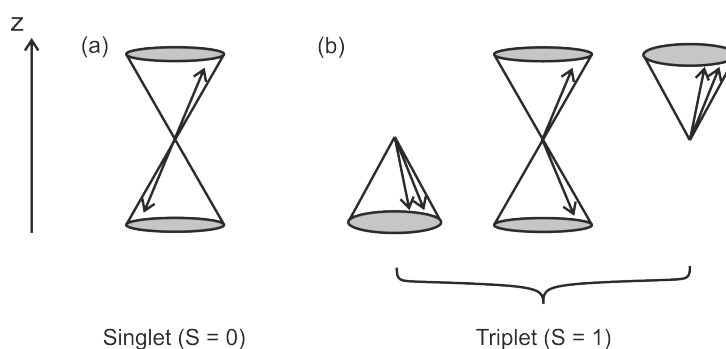
Figure 2.5: The relative spin orientations of two electrons around a local magnetic field in z-direction. In the singlet state, the electron spins are 180° out of phase with a total spin of S = 0. There are three possible configurations for triplet states with a total spin of S = 1, where the spin directions are in phase.[7]

To fully describe a state, the spin of a state should also be considered, and it is determined by the total spin of all electrons in all orbitals. According to the Pauli exclusion principle, electrons in filled orbitals are paired with anti-parallel spins, therefore contributing zero to the total spin. Yet, if one of the paired electrons is promoted to orbital with higher energy, the two electrons do not share the same orbital anymore. Thus these two electrons could have parallel or anti-parallel spins. If the two electrons hold opposite spin directions, it is referred to as singlet state with a total spin of S = 0 and a multiplicity of M = 2S + 1 = 1 (Figure 2.5a). If the two unpaired electrons have the same spin orientations, the molecule is referred to have a triplet state with a total spin of S = 1 and a multiplicity of M = 2S + 1 = 3 (Figure 2.5b).[8] Figure 2.5 represents the possible spin directions of the singlet and triplet states around a local magnetic field in z-direction. The spins in the triplet state are always in phase, while in the singlet state they are 180° out of phase. There is only one possible spin orientation combination in the singlet state, yet three possibilities in the triplet state. So upon electrical excitation, the chance to create a triplet state is three times higher than a singlet state.

The Jablonski diagram in Figure 2.6 describes the scheme of the relative energy levels and the possible transition processes in a molecule. When absorption happens, one electron is promoted from the HOMO to the LUMO, creating excited electronic state. Generally, the excited state S_2 has shorter lifetime than the S_1, so when the state S_2 is created by an electrical excitation. When the transition from S_2 to S_1 takes place very rapidly. This conversion process is non-radiative and it is called internal conversion (IC). All the electrons at the ground state have antisymmetric spin directions owing to Pauli exclusion principle, and therefore the state has a total spin of S = 0. Hence the relaxation from first singlet excited state to the vibrational states of the ground state is allowed. This process usually happens within a few nanoseconds and the emission is fluorescent.[10]
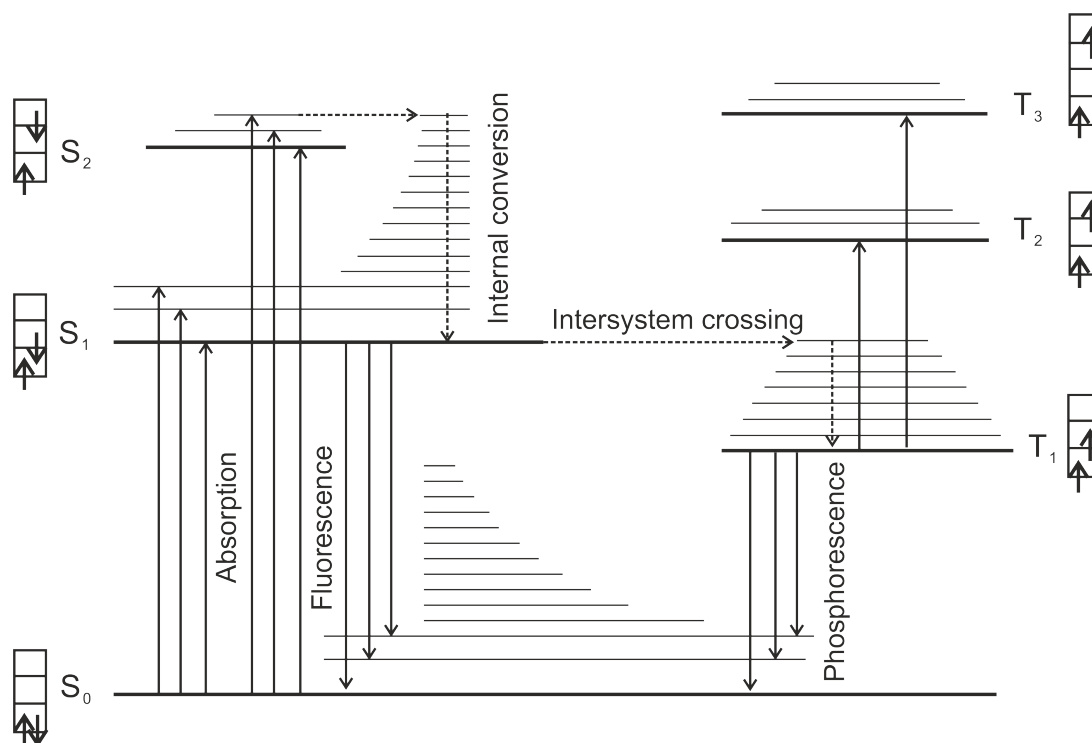
Figure 2.6: The Jablonski diagram describes the energy levels of different states in one molecule. It also shows the processes of absorption, fluorescence, intersystem crossing, internal conversion and phosphorescence. "S" represents singlet state, while "T" means triplet state. The relative spin directions of each state are also indicated.[13]

Although the first triplet state (T_1) has less energy than the first excited singlet state (S_1), the transition from S_1 to T_1 is highly improbable. As mentioned above, the singlet state has a spin of S = 0, while for the triplet state, S = 1 indicates that this transition will violate the angular momentum conservation. The same applies to the relaxation from triplet state to the ground state.[11] However, if heavier atoms, such as platinum (Pt) or iridium (Ir), are contained in the molecule, the spin-orbit interaction becomes stronger, allowing for the intersystem crossing (ISC).[12] In this case, the molecule transits from the S_1 state to the vibrational state of T_1, followed by a rapid vibrational relaxation to the lowest vibrational state of T_1. Under this circumstance, a molecule in the T_1 state could also transit to S_0 by emitting phosphorescence. Due to the angular momentum difficulty, the phosphorescence process is relatively slow and it generally happens within μs to hours.[8]

2.3 Material Classes

Organic materials can be divided into three classes: Molecular crystals, polymers, and small molecules. Molecules of the acene family, such as naphthalene or anthracene, can form the basis of a crystal structure that is held together by van der Waals
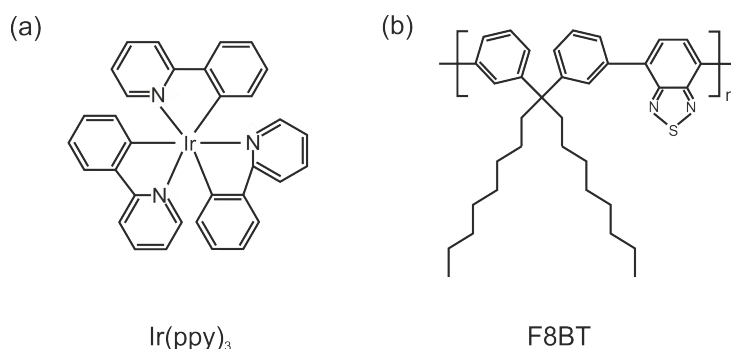
Figure 2.7: One representative small molecule and one polymer that are widely investigated as OLED emitters.(a) Ir(ppy)$_3$ and (b) F8BT.

forces. The charge carrier mobilities in the molecular crystals are usually higher than in the noncrystalline organic semiconductors, therefore they are widely applied in the transistors.[7] In the OLED applications, small molecules and polymers are more common. Hence they will be discussed further.

Small Molecules

Small molecule materials usually do not have many repeat units, thus sharing rather low molecular weights. The small molecules can be deposited as an amorphous film via thermal evaporation or solution processes, and in commercial OLED panels, they are the most common types of organic materials. Generally, it is nearly impossible to chemically optimize the energy levels in a molecule so that it is suitable to transport holes, electrons, emit light, and absorb light efficiently in the desired wavelength range. Thus normally one small molecule is only designed to fulfill one task. The molecular structure of a representative small molecule emitter, tris[2-phenylpyridinato-C2,N]iridium(III) (Ir(ppy)$_3$), is provided in Figure 2.7.

Polymers

Polymers consist of many repeating units, which are also called monomer units. It can be considered as a chain of covalently coupled molecular repeat units. Thus the molecular weights of polymers are usually high. Accordingly, it is impossible to evaporate them. On the other hand, their film forming ability from solution are favorable, hence they are deposited from solutions. A representative green-emitting polymer for OLED, poly(9,9-dioctylfluorene-alt-benzothiadiazole) (F8BT), is shown in Figure 2.7a.
Depending on the variations of the repeating monomer units, homopolymers or copolymers can be formed. Copolymers can further be divided into three subclasses,

depending on the sequences of the different repeat units. Alternating copolymers, statistical copolymers and block copolymers correspond to the situations where various monomer units are alternating, follow in a random way, or appear as blocks respectively.[7] There are conjugated and nonconjugated polymers. But a conducting or semiconducting polymer requires a conjugated π-electron system.[14] In conjugated polymers, π electrons are delocalized, allowing charge carriers to move on the polymers. The conjugation length can influence the polymers' optoelectronic properties, such as the mobilities and the emission spectrum. In most semiconducting polymers, the electronically relevant parts combine to form the polymer backbone, and this kind of polymer is called main chain polymer. Nevertheless, the semiconducting polymers with π conjugated electron system as side chains also exist.

In order to dissolve the polymers in common organic solvents, many polymers contain the side chains that facilitate the solubility. Nevertheless, the side chains separate the electronic active backbone from each other once the polymer is deposited as a film. Thus, it is critical to choose the suitable side chains for the polymers during polymerization.

3 Organic Light Emitting Diodes

3.1 Charge Carrier Injection

The most simplified OLED architecture (Figure 3.1a) comprises two electrodes, which are responsible for the charge carrier injection, and an emissive layer (EML), where the photon emission takes place. An additional electron in LUMO of the emitter is realized via electron injection, while hole injection indicates the removal of an electron from HOMO. Electrons tend to occupy lower energy levels, yet holes aim to move upwards on an energy scale. Hence, to achieve ideal charge carriers injection without any injection barrier, the work function, i.e. the minimum energy to extract one electron into vacuum, of the anode should be equal or larger than ionization energy (I_p) of the organic material. Conversely, the work function of a cathode needs to be the same or smaller than electron affinity (E_A) of the organic semiconductor.[15] Under these circumstances, the contact between the electrode and the organic material is Ohmic.

Figure 3.2 depicts the energy level alignment of the simplified OLED architecture. Before the materials get into contact, the vacuum level is flat and the Fermi levels are not aligned.
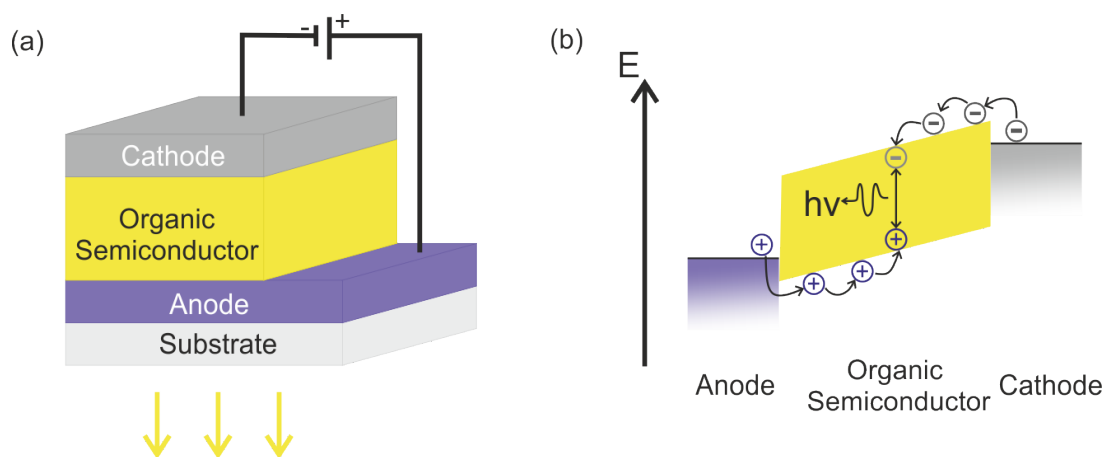
Figure 3.1: (a) An OLED essentially involves a cathode, an anode and an organic semiconductor which emits light when an operating voltage is applied. The OLED is built on a transparent substrate, such as glass or plastic foil (e.g. polyethylene terephthalate (PET)). (b) Holes are injected from the anode into the organic semiconductor and transported towards the cathode, while electrons are injected from the cathode and transported towards the anode. An electron and a hole are bound to form an exciton which decays to the ground state by releasing the energy (hν) with form of a photon.

When they are connected, the electrons flow from one electrode to the other through the organic semiconductor, so that the potential difference between two electrodes is eliminated and the Fermi energies equilibrate. In this case, the vacuum level is shifted and the HOMO and LUMO levels through the film are tilted. Thus a built-in potential (V_{bi}), equal to the work function difference of the electrodes, is built. It can be calculated by

$$V_{bi} = \frac{1}{e}(\Phi_{anode} - \Phi_{cathode}) \qquad (3.1)$$

where Φ_{anode} and $\Phi_{cathode}$ are the work functions of the electrodes. If $\Phi_{cathode} > E_A$, when an electron is injected from the cathode into the LUMO of the organic semiconductor, it will promptly return to the cathode since electrons tend to stay at low energy levels.[7] However, when an external voltage ($V = V_{bi}$) is applied to the device, the built-in electric field can be compensated, therefore the HOMO and LUMO levels are flat. Further increase of the applied voltage changes the tilt direction of the energy levels in the organic layer, allowing for electron and hole injection.

If an injection barrier exists at the metal-organic semiconductor interface, three mechanisms occur (Figure 3.3) for the charge carriers to overcome the injection barrier and reach the organic semiconductor, namely thermionic emission, tunneling and hybrid transition. If the electron injection barrier between the metal and the organic material is Φ_B and the charge carriers can obtain sufficient thermal energy to overcome this potential barrier, then the injected electrons remain on the surface of the organic layer at a certain distance from the metal-organic interface. As a consequence, an equivalent amount of holes, which are referred to as image charges, will be induced in the metal layer. Consequently, the barrier of the charge injection at the metal-organic interface is reduced by the image potential due to the Coulomb attraction between the electrons and the holes. This lowering of the barrier by the image potential is called Schottky effect. Charge carriers will be injected once they acquire enough energy to cross over the potential barrier (Figure 3.3a). This Richardson-Schottky thermionic emission is dominant if a low voltage is applied on the device. At presence of a strong electric field, the energy barrier becomes smaller and permits electrons to tunnel into the organic semiconductor (Figure 3.3b). This tunneling is also referred to as field emission or Fowler-Nordheim (FN) tunneling.[16] The most common injection mechanism is a hybrid process as illustrated in Figure 3.3c, which is in principle a combination of Richardson-Schottky thermionic emission and tunneling.

The simplified electroluminescence process is illustrated by Figure 3.1b. Upon an external electrical field applied to this device, charge carriers are injected from two electrodes into the LUMO and HOMO levels of organic semiconductor before they are transported
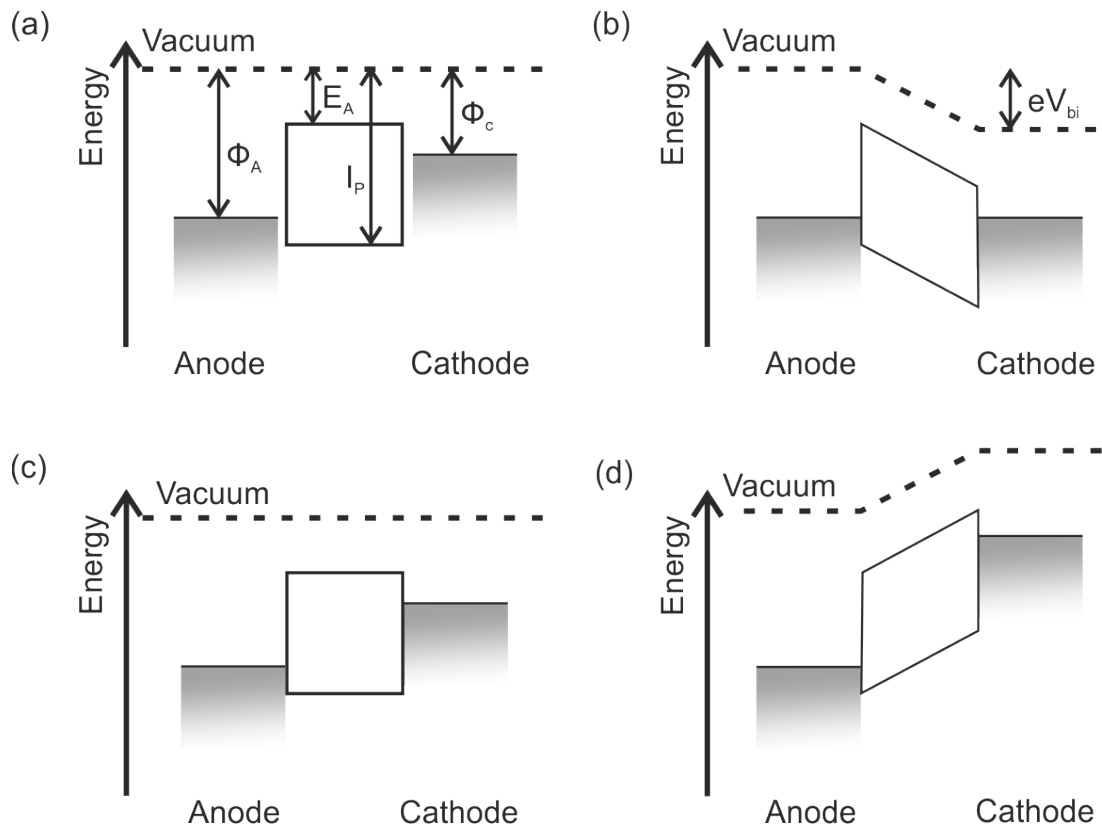
Figure 3.2: The cathode and the anode have work functions of Φ_{cathode} and Φ_{anode} respectively. The organic semiconductor between the two electrodes has an electron affinity of E_A and an ionization energy I_p. (a) The two electrodes and the organic material are not in contact. (b) When they are brought into contact, the Fermi levels of the two electrodes are aligned and the vacuum level is also shifted. The built-in potential (V_{bi}) inside the device is the work function difference between the two electrodes. (c) An external voltage ($V = V_{bi}$) is applied to compensate the built-in electric field, and the vacuum level is flat again. (d) An external voltage $V > V_{bi}$ is applied, enabling the charge carrier injection.

towards each other. The recombination of electrons and holes results in energy relaxation in form of photons. Then the photons can be emitted through the transparent substrate.

3.2 Electrodes and Injection Layers

In order to couple light out from the device, at least one electrode has to be transparent at the emission wavelength, and often it is the bottom electrode. Despite the existence of top-emitting and transparent OLEDs, the working principles are the same as the bottom-emitting OLEDs. Thus for simplicity, only bottom-emitting OLEDs with transparent anodes are discussed further. OLEDs for flat-panels and solid-state lightings are required to emit at visible wavelengths, thus the transmittance of the bottom electrode is supposed to be high from 380 nm to 780 nm. Another essential as pect that should be taken into consideration is the work function. As discussed in chapter 3.1, the work function of the
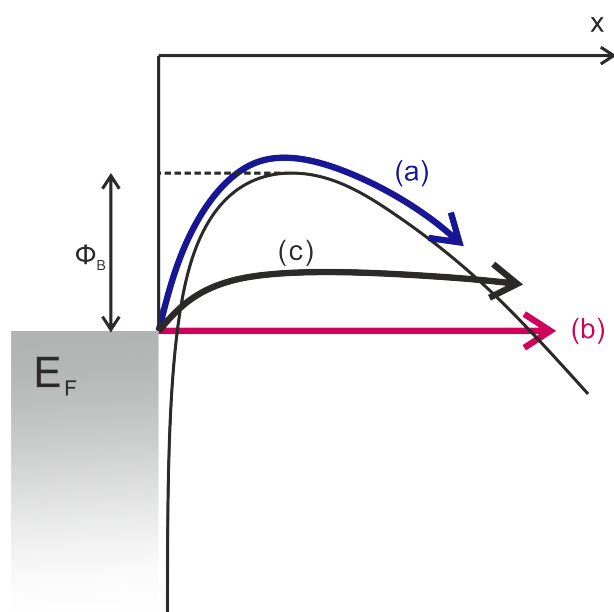
Figure 3.3: The charge carrier is injected from a metal with Fermi level of E_F into an organic material, an injection barrier of Φ_B exists. It takes place either via (a) Richardson-Schottky thermionic emission, (b) Fowler-Nordheim (FN) tunneling or (c) hybrid transition of thermionic emission and tunneling.

electrode should match the energy levels of the organic material for efficient charge carrier injection, indicating the cathode with a low work function while the anode with a high work function.

The most common transparent anode in organic electronic devices is a n-doped semiconductor indium tin oxide (ITO). As an electrode, there is a trade off between transmittance and resistance, and its optimized resistance is usually quoted as $10^{-4} \, \Omega \, cm$.[17] The transmittance over visible spectrum is around 90% with a film thickness of d = 120 nm.[18] Its work function is about $\Phi = 4.9 \, eV$, but with appropriate time of oxygen (O_2) plasma treatment, its work function can be further increased, thus facilitating the hole injection.[19–22] Another alternative to ITO transparent electrode is aluminum doped zinc oxide (AZO). With a thickness of d = 130 nm, the sheet resistance can be as low as $R_\square = 27 \, \Omega$.[23] Besides the metal oxides, there have also been various reports on transparent electrodes based on graphene, carbon nanotubes or silver nanowires.[24–26] Notably, another common conductive polymer mixture poly(3,4-ethylenedioxythiophene) polystyrene sulfonate (PEDOT:PSS) has been widely used as transparent electrode in the organic devices due to its unique advantages of flexibility and solubility.[27–29] To further increase the conductivity of PEDOT:PSS, AgNWs have been demonstrated to combine with PEDOT:PSS at the cost of transparency.[29, 30]

Although ITO has a rather high work function, hole injection barriers still exist when the HOMO levels of the organic semiconductors are below $-5 \, eV$. Accordingly, to enhance the hole injection, a so-called hole injection layer (HIL) is generally inserted between the
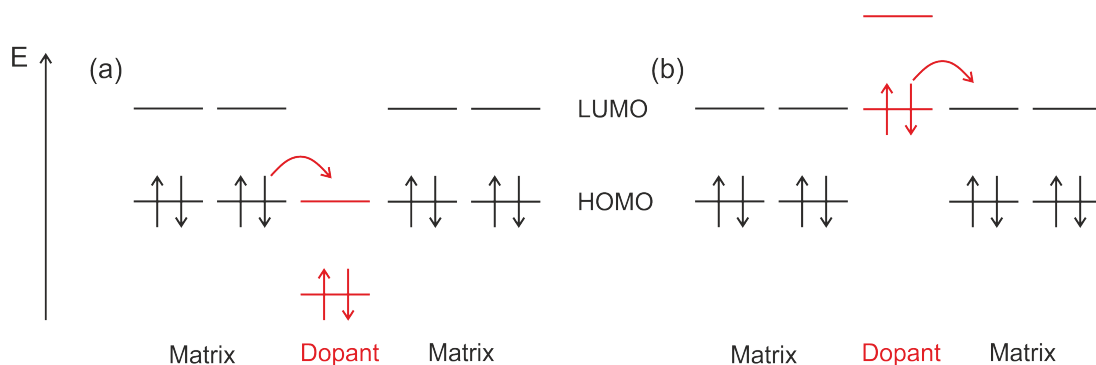
Figure 3.4: Schematic demonstration of (a) p-type and (b) n-type doping. In p-type doping, the dopant accept electrons from matrix, while n-type dopant donate electrons to the matrix.

anode and the emission layer. The injection layer can be p-doped organic semiconductor, intrinsically doped metal oxide, or self-assembled molecules.

The conductivity of a doped layer can be increased by several orders of magnitude, well above the intrinsic conductivity of pure materials or the arbitrary conductivity caused by background impurities.[31] Similar to doping in inorganic semiconductors, there are n-type and p-type doping materials. To achieve p-type doping, the dopant extracts electrons from the HOMO state of the matrix, therefore creating holes in matrix as shown in Figure 3.4a. Thus a proper p-type dopant should have a LUMO level lying below the HOMO level of the organic material. Besides of being used as electrode, PEDOT:PSS is comprised as HIL in most OLED architectures, owing to its high work function of $\Phi = 5.2\,\text{eV}$.[32] Lee et al. presented that by adding a self-organized molecule perfluorinated ionomer (PFI) into PEDOT:PSS, the work function of the mixed layer is further increased. Accordingly, hole injection barrier to the HOMO of the organic semiconductor is smaller and the lifetime of the device turned out to be enhanced.[33]

Transition metal oxides, such as molybdenum oxide (MoO_3), vanadium oxide (V_2O_5) and tungsten oxide (WO_3), exhibit excellent hole injection abilities in OLEDs.[34, 35] The work functions turned out match the HOMO levels of many fluorescent emitters, such as F8BT.[36, 37] The traditional approach to deposit these transition metal oxides is thermal evaporation. Recently, papers reported on solution processed metal oxide from precursor or nanoparticle dispersions.[38–41]

For the cathode, a rather low work function is critical to efficiently inject electrons. Hence, materials with low work functions, such as calcium (Ca, $\Phi = 2.9\,\text{eV}$) or barium (Ba, $\Phi = 2.5\,\text{eV}$), are widely used as cathode.[42, 43] But they are unstable in air and tend to react with water and oxygen. Therefore they are often covered by another rather stable metal, such as Al or Ag with work functions of $\Phi = 4.3\,\text{eV}$.[36, 42, 44–47]

Alternatively, a low work function cathode can be achieved by depositing an ultrathin metal salt, for instance lithium fluoride (LiF) or cesium fluoride (CsF), between emissive

layer and metals.[48] LiF or CsF is believed to allow favorable dipole- or bias-induced realignment of the Fermi levels of the metals and the LUMO energy levels of the organic layers. As a consequence, the electron injection barrier is reduced.[44]

An electron injection layer (EIL) is essential if the electron injection barrier is substantial. The EIL can be a n-doped organic material or metal oxide. Unlike in p-doping, the dopant in n-type doping has to donate electrons to the LUMO level of the organic matrix (Figure 3.4b). Thus n-type doping is more challenging than p-doping, since the HOMO level of the dopant has to be higher than the LUMO of the matrix material. However, a high HOMO level generally leads to the instability of the dopant against oxidation.[49] Hence, organic semiconductors doped with alkali metals (lithium (Li), cesium (Cs)) or alkali compound such as LiF, CsF or cesium carbonate (Cs_2CO_3) are often incorporated as EIL.[50–52] If the doping concentration is high enough, then the charge carriers at the contact can tunnel from the metal into the organic layer, leading to a quasi-Ohmic contact.

Owing to their energy alignment capabilities, zinc oxide (ZnO), titanium oxide (TiO_2) and zirconium oxide (ZrO_2) have been used as electron injection layers.[43, 44, 53, 54] Zhou et al. proposed a universal approach to generate low work function electrodes and electron injection layers for organic electronic devices by employing a surface modifier, namely polyethylenimine ethoxylated (PEIE) or branched polyethylenimine (PEI). The modifier effectively builds dipole moments at the interface, resulting in a low work function surface.[55] If this modifier is deposited on top of a metal oxide, e.g. ZnO, its work function can be further decreased, which is beneficial for effective electron injection.[22]

3.3 Charge Carrier Transport

Once the charge carriers are injected into organic semiconductor, electrons and holes have to be transported inside the organic material in order to recombine radiatively. Unlike crystalline semiconductors, most organic semiconductors are amorphous and disordered. The band structure used to describe inorganic semiconductors is therefore not applicable. Thus, a different model is applied to depict the charge carrier transport in disordered organic semiconductors. In disordered organic semiconductors, molecules interact with each other only via weak van der Waals forces. The lattice thermal vibration is so strong that the energetic widths of the HOMO and LUMO are small and the bandgap is large. In organic semiconductors, excitations and interactions are localized on the individual molecules. Therefore, free propagation of the charge carriers does not exist and discrete energy levels dominate the bulk.[56]

In a real system, inevitable impurities, structural defects, like chain kinks or twists, always exist. Hence the energy levels can be perturbed by lattice vibrations. Organic
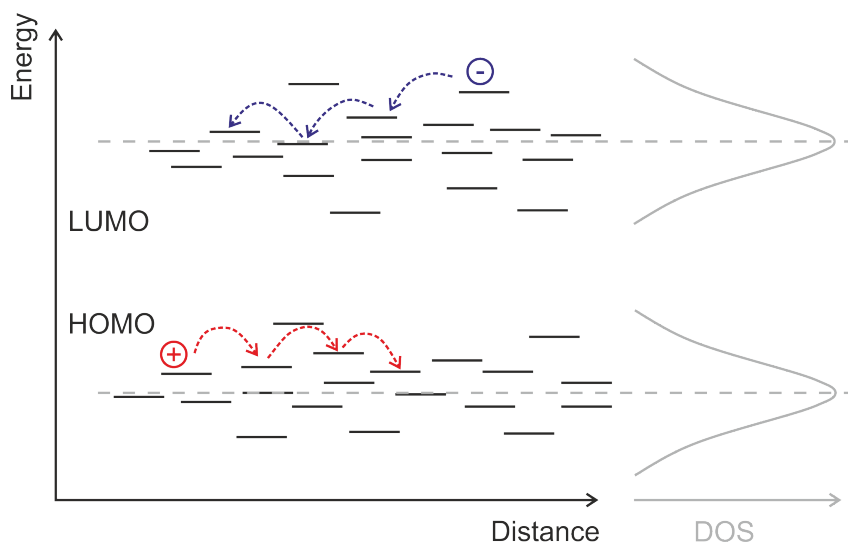
Figure 3.5: Charge transport in organic disordered semiconductors is caused by incoherent hopping of charge carriers via localized states. These sites are randomly distributed with a Gaussian energy spectrum. Electrons hop from one site to another site in LUMO, while holes transit from one site to another in HOMO.[62]

semiconductors do not simply have two delocalized energy levels separated by a forbidden energy gap, instead, an energetic spread of charge carrier transport sites is involved. In this system, one charge is localized at one site, and it hops to the adjacent molecule as demonstrated in Figure 3.5. The energy spread in the HOMO and LUMO can be described by a Gaussian density of states (DOS), which reflects the disorder of the system. The Gaussian distribution of energy levels can be described as

$$\mathrm{DOS(E)} = \frac{\mathrm{N}}{\sqrt{2\pi}\sigma}\mathrm{exp}\left[-\left(\frac{\mathrm{E}}{\sigma}\right)^2\right] \tag{3.2}$$

where σ is the energy scale of the density of states and N is the concentration of randomly distributed localized sites.[57] The so-called hopping process in organic semiconductors limits the charge carrier mobilities in organic materials. In addition, sometimes sites with low energy can act as traps for electrons, and sites with high energy act as traps for holes, further hindering the charge carrier transport. Typical organic semiconductors have mobilities below 10^{-2} cm^2/Vs.[58–60] For comparison, a typical inorganic semiconductor such as silicon has much higher electron mobility of 1450 cm^2/Vs at room temperature.[61] In the DOS model, the mobility depends on the applied electric field, the concentration of localized sites, the concentration of charge carriers as well as the temperature. Its dependence on the temperature can be described by

$$\mu(\mathrm{T}) = \mu_0 \cdot \mathrm{exp}[-(\frac{2\sigma}{3\mathrm{kT}})^2] \tag{3.3}$$

where μ_0 is the zero-field mobility $(T \to \infty)$.[63] By combining the dependency on the temperature, the relation between mobility and the applied electric field (F), the mobility can be written as

$$\mu = \mu_0 \exp\left[-\left(\frac{2\sigma}{3k_BT}\right)^2\right]\begin{cases} \exp\left[C\left(\left(\frac{\sigma}{k_BT}\right)^2 - \sum^2\right)\sqrt{F}\right] & \text{for } \sum \geq 1.5 \\[2ex] \exp\left[C\left(\left(\frac{\sigma}{k_BT}\right)^2 - 2.5\right)\sqrt{F}\right] & \text{for } \sum < 1.5 \end{cases} \tag{3.4}$$

where C is a constant that depends on the site spacing, $\sum$ is the degree of positional disorder.[64] When an electric field is applied, the trap potential will be deformed into an asymmetric shape, so that the electric field assists the detrapping of the charge carriers, thus facilitating the charge carrier transport.[16]

3.4 Transport Layers

Transport layers are generally introduced between emission and injection layers. With a transport layer between the injection and emission layers, the distance between electrode and emission layer can be modified by variating the thickness of the transport layer. Via this adjustment, the outcoupling efficiency can be modified as will be discussed in Chapter 3.9.2. Unlike injection layers, charge carrier transport layers are often made of undoped organic semiconductors with moieties which are in favor to transport either electrons or holes.

In the ideal case, the HOMO of the HIL, the hole transport layer (HTL), and the emitter should have identical values so that no extra energy barrier is raised by introducing the HTL. In order to confine the charge carriers in the emission layer, an HTL which is able to block electrons is preferable. In other words, the LUMO level of the HTL should be higher than the LUMO of the emitter, so that the electrons encounter a barrier when trying to escape the emission layer without recombining. Therefore it is also referred to as an electron blocking layer (EBL). Likewise, the electron transport layer (ETL), the EIL and the emitter should have similar LUMO levels. The ETL can be considered as a hole blocking layer (HBL) if its HOMO lies below the HOMO of the emitter (Figure 3.6). Nevertheless, the blocking layer and the transport layer are not necessarily to be the identical layer. It is also possible to employ extra blocking layers in addition to the transport layers.[65, 66]

As discussed in Chapter 2.2, triplet excitons have longer excited state lifetime than the singlet excitons. Therefore the triplet excitons in the emitter are more likely to diffuse to the adjacent layers without releasing photons. Thus exciton blocking layers are of

(a)

(b)
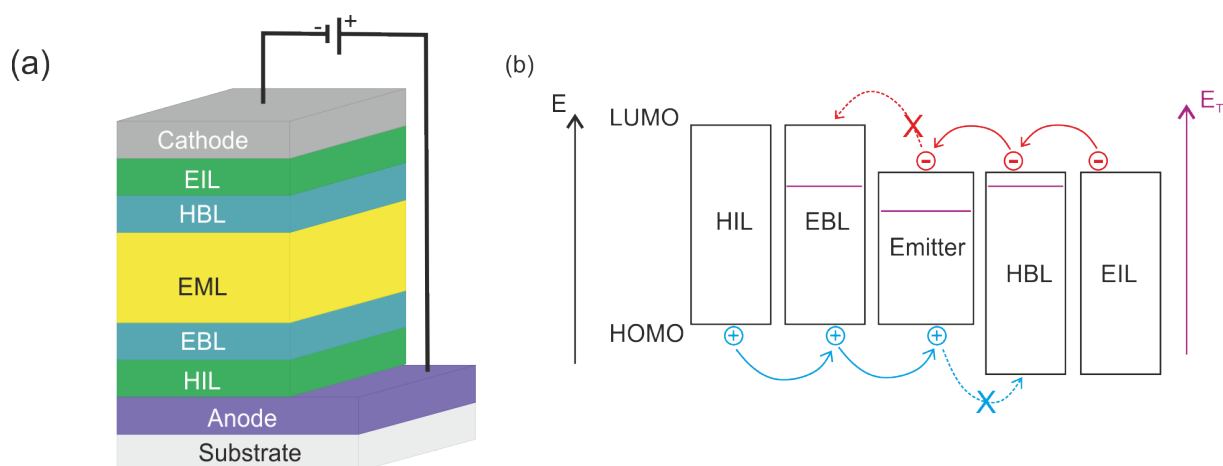
Figure 3.6: (a) In the OLED architecture, various functional layers, such as injection layers, transport layers/blocking layers are introduced between the electrodes and the emission layer to facilitate the device efficiency. (b) The energy diagram of an ideal OLED with charge carrier injection and blocking layers adjacent to the emitter. The HOMO levels of the HIL, EBL and the emitter are identical. Likewise, the LUMO levels of the EIL, HBL and the emitter are the same. The EBL has a higher LUMO than the emitter so that electrons cannot propagate to the anode. Likewise, the HBL has a lower HOMO level so that holes are confined in the emitter. The right axis (purple) represents the triplet energy axis. In this case, both the EBL and HBL exhibit higher triplet energy levels than the emitter. Therefore, the triplet excitons formed in the emitter cannot transfer to the adjacent layers.

paramount importance if triplet excitons are supposed to contribute to the emission. This can be fostered by charge blocking layers if the HBL and EBL exhibit higher triplet energy levels than the emitter.[67, 68] In Figure 3.6, both the electron and hole blocking layers exhibit higher triplet energy levels than the emitter, indicating an effective exciton confinement.

3.5 Excitons

When an electron is excited from the HOMO level to the LUMO level, a hole is created on the HOMO. The bound pair of an electron and a hole which are attracted by Coulomb forces is referred to as exciton, and it can be treated as a neutral particle which can diffuse.

In inorganic semiconductors, the dielectric constant is large and the Coulomb interactions between the electrons and holes are small. Yet, it is still possible to form excitons if the incident photon energy is smaller than the minimum energy to promote an electron from valence band to conduction band. So the electron is still influenced by the Coulomb potential of the hole. This generates large-sized Wannier-Mott type exciton, or Wannier exciton, which is much larger than the typical lattice spacing (Figure 3.5a). The exciton binding energy (E_B), the essential energy to dissociate an exciton into uncorrelated

Figure 3.7: (a) In inorganic semiconductors, the binding energy of an excited Wannier exciton is so small that the thermal energy is large enough to dissociate it. The distance between the electron and the hole is much larger than the lattice constant. (b) Frenkel excitons are usually small-sized, and the electron and the hole are localized on the same molecule. (c) Charge transfer excitons can exist in molecular crystals, if the electron is promoted to an adjacent molecule, leaving one hole behind. Its size is between the size of Wannier and Frenkel excitons.[12]

electron and hole, is generally small ($E_B < 0.01\,eV$). Hence the thermal energy at room temperature ($26\,meV$) is already enough to dissociate the exciton. The spin directions of the electrons at conduction band and valence band are not relevant anymore. Thus the free electrons and holes in inorganic semiconductors can be considered as directly generated from photon excitations at room temperature.[15] The radiative recombination of the free electrons and holes, which is responsible for electroluminescence, can be treated as a direct process as well.[9]

In most organic semiconductors, the dielectric constant is small and the interactions between the electrons and holes of excitons are strong. Figure 3.5b demonstrates this smaller-sized exciton which is commonly referred to as Frenkel exciton. Such an electron-hole is localized on the same molecule. It can either recombine or dissociate into free carriers. As the binding energy E_B is relatively large (in the range of $0.5\,eV$ to $1\,eV$), the thermal energy at room temperature is not sufficient to dissociate the exciton.[9] Therefore, an additional energy coming from externally applied electric fields or extra thermal energy is required to dissociate the exciton.[15]

In organic crystals, in addition to small-sized Frenkel excitons, it is also possible that the promoted electron escapes into the adjacent molecule, but still remains bound to the hole left behind. As depicted in Figure 3.5c, the resulting exciton is called charge transfer exciton. It is also neutral but polar. Its size and binding energy are between Frenkel exciton and the Wannier exciton.[12]

3.6 Light Emitting Materials

The emission layer, where the excitons radiatively decay, is decisive for the OLED performance. As discussed in Chapter 2.2, after excitation, 75% of the excitons
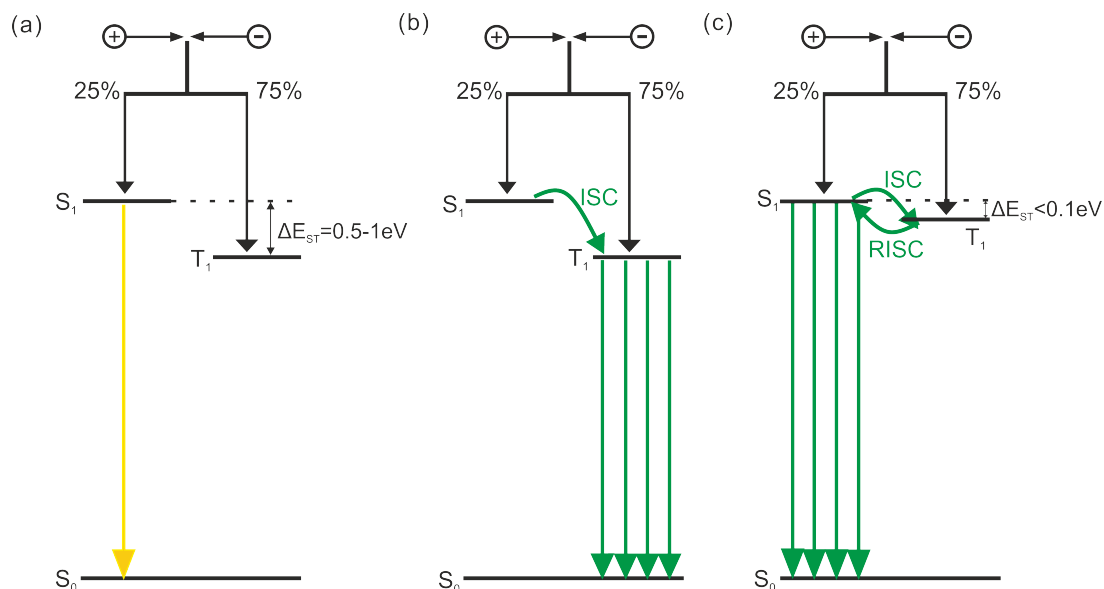
Figure 3.8: (a) In fluorescent emitters, only 25% singlet excitons can be exploited for the emission, and the radiation from the singlet state S_1 to the ground state S_0 is fluorescent. (b) In the phosphorescent emitters, intersystem crossing (ISC) is possible. Therefore the singlet excitons are transferred to the triplet state T_1 and then decay to S_0, utilizing all excitons. The radiation is phosphorescent. (c) In thermally activated delayed fluorescence (TADF) emitters, due to the small energy difference between S_1 and T_1, the reverse intersystem crossing (RISC) is also permitted. Consequently the triplet excitons transfer to the S_1 state by absorbing thermal energy. Then they decay to S_0 by emitting fluorescence.

formed are triplet excitons and only 25% are singlet excitons.[36] Based on the emission mechanisms, there are mainly three kinds of emitters applied in OLEDs, namely fluorescent, phosphorescent and thermally activated delayed fluorescent (TADF) emitters. They are schematically depicted in Figure 3.8.

Fluorescent Emitters

The research on OLEDs was started on the fluorescent OLEDs reported by Tang and Van Slyke using tris(8-hydroxyquinoline)aluminum (Alq$_3$) as the emitter and electron transport material.[1] Fluorescent OLEDs are therefore considered as the first generation OLEDs, in which the radiation from the singlet state S_1 to the ground state S_0 is utilized. As in Figure 3.8a, with electron-hole pairs injected into the fluorescent molecule, statistically 25% singlet excitons and 75% triplet excitons are formed. The singlet excitons can decay to the ground state S_0 by emitting fluorescence, but no photon emission is observed from the triplet excitons under standard conditions, because the rate constant of the emission is too low compared to the rate of the nonradiative processes, e.g. the energy transfer to vibrations or reactions with quenchers such as oxygen molecules.[36] Thus, in conventional fluorescent OLEDs, only 25%

excitons can be utilized. A typical singlet exciton possesses a lifetime shorter than 10 ns.[69] In contrast, in photoluminescence, only the singlet excitons are populated after absorbing photons according to the spin-selection rule $\Delta S = 0$. Therefore a fluorescent emitter can achieve a quantum yield of 100% under photoluminescence. In the conventional fluorescent OLEDs, fluorescent emitters are mostly directly applied as emission layers, but it can also be mixed with a host matrix with wider bandgap.[70, 71]

Phosphorescent Emitters

After understanding the intrinsic limitations of fluorescent emitter, research efforts focused on the development of efficient phosphorescent devices to take advantage of the 75% triplet excitons.[72, 73] It is known that spin-orbit coupling is necessary to break down the rule of $\Delta S = 0$ and to enhance the triplet radiative rate constant. The magnitude of the spin-orbit coupling constant is proportional to Z^4, where Z represents the atomic number. Hence heavy elements such as iridium and platinum are beneficial for introducing strong spin-orbit coupling.[74] Spin-orbit interactions enable intersystem crossing from the excited singlet state S_1 to the excited triplet state T_1 and the emission from T_1 to S_0. As illustrated in Figure 3.8b, in the ideal case, 25% singlet excitons are also transferred to T_1 and all the excitons decay via phosphorescent emission. Thus the potential quantum yield of a phosphorescent emitter can be 100%. By incorporating such phosphorescent compounds into the emission layer, the emission from the triplet exciton decay can be harvested. Triplet excitons have rather long lifetimes ($\sim 1\,\mu s$) compared to fluorescent excitons, therefore undesired annihilation processes are more likely to happen in phosphorescent emitters.[69, 75] Hence, to accomplish high quantum yields, it is critical in phosphorescent OLEDs that the triplet excitons are not in vicinity of each other. Consequently host-guest systems are often introduced in the emission layers of phosphorescent devices, with the ratio of the phosphorescent dye to the host being relatively low.[11, 76] The host matrix does not necessarily have to be one single material, it can consist of several compounds with different properties. Sometimes, to balance the charge carriers in the emissive layer, double emissive layers are introduced, where the emitter is doped in two adjacent hosts. Usually one of two hosts has superior hole transport ability and the other exhibits better electron transport.[77–80]

TADF Emitters

Although phosphorescent materials are widely applied in commercial OLED displays, the blue emitting phosphorescent OLEDs are still inferior in the stability and efficiency. Lately, TADF materials have become attractive with a booming development since Tanaka

et al. reported the first high-performance TADF OLEDs.[81, 82] As illustrated in Figure 3.6c, the energy difference between S_1 and T_1 is small ($\Delta E_{ST} < 0.1\,eV$) which facilitates reverse intersystem crossing (RISC) with the aid of thermal energy. Therefore triplet excitons can be converted from T_1 to S_1, and consequently all the excitons can decay from S_1 to S_0 by emitting fluorescent light. The prompt fluorescence happens in ns, while the delayed fluorescence takes place in µs.[81]

In TADF materials, it is critical that (i) the nonradiative channels for S_1 and T_1 are suppressed, and (ii) the energy difference between S_1 and T_1 is small. The rate of reverse intersystem crossing (k_{RISC}) is related to the energy difference between the singlet and triplet states (ΔE_{ST}), and it can be written as

$$k_{RISC} \propto \exp(\frac{\Delta E_{ST}}{k_B T}) \tag{3.5}$$

where k_B is Boltzmann's constant and T is the temperature.[83] Importantly, ΔE_{ST} is proportional to the exchange integral (K) between electrons in HOMO and LUMO

$$\Delta E_{ST} = E_S - E_T = 2K \tag{3.6}$$

The exchange integral is in turn decided by

$$K = \iint \Phi_{HOMO}(\boldsymbol{r}_1)\Phi_{LUMO}(\boldsymbol{r}_2)\frac{1}{|\boldsymbol{r}_2 - \boldsymbol{r}_1|}\Phi_{HOMO}(\boldsymbol{r}_2)\Phi_{LUMO}(\boldsymbol{r}_1)\,d\boldsymbol{r}_2\,d\boldsymbol{r}_1 \tag{3.7}$$

where Φ_{HOMO} and Φ_{LUMO} are spatial distributions of HOMO and LUMO, $\boldsymbol{r}_1$ and $\boldsymbol{r}_2$ are two position vectors. If the overlap of Φ_{HOMO} and Φ_{LUMO} is small, K is also small, and so is the energy difference between T_1 to S_1.[84] Because the first-order mixing coefficient between singlet and triplet states (α) is inversely proportional to ΔE_{ST}

$$\alpha \propto \frac{H_{SO}}{\Delta E_{ST}} \tag{3.8}$$

where H_{SO} is the spin-orbit interaction. Thus, even in purely organic molecules without any heavy elements, ISC and RISC become likely if ΔE_{ST} is sufficiently small. Therefore the molecule structure should be designed in a way that HOMO and LUMO are located on different moieties of the molecule, resulting in a small overlap between the LUMO and HOMO.[85, 86] Thus in all efficient TADF emitters, the HOMOs and LUMOs are spatially separated on a donor and an acceptor part of the molecule.[87]

Recently, there are also many reports on copper(I) complexes utilizing TADF mechanisms. In these compounds, the central copper atom induces moderate spin-orbit coupling, mixing the excited singlet and triplet states and resulting in small energy split between

S_1 and T_1. Hence ISC and RISC rates are high in these molecules. That is also the major difference between copper(I) complexes and all-organic molecules.[87]

Since triplet excitons are essential in TADF OLEDs as well, a host-guest system in the emission layer is common, where the host has higher triplet energy level than the TADF emitter.[85, 88] Nevertheless, emission layers consist of neat TADF molecules without any host have also been reported.[89, 90]

3.7 Energy Transfer

As the excited state is generally localized on one molecule in organic material, the transfer from one molecule (energy donor D) to another (energy acceptor A) occurs via two ways, namely Förster and Dexter transfer, depending on whether the energy transfer takes place by emission and reabsorption of photons, or by quantum chemical coupling.

Förster-type Energy Transfer

The Förster transfer is a dipole-dipole coupling of the donor and acceptor molecules. It is facilitated by the overlap of the donor's emission spectrum and the acceptor's absorption spectrum. The released energy from the donor is absorbed immediately by the acceptor, exciting the acceptor molecule. It can take place when the distance between two molecules is large ($40\,\text{Å}$-$100\,\text{Å}$) compared to their sizes. Förster energy transfer only occurs when the transitions between ground states and excited states of both donor and acceptor molecules are allowed. Singlet to singlet energy transfer is dominated by this process with low concentrations of acceptors. It can be described as

$$^1D^* \rightarrow {}^1D + h\nu$$
$$^1A + h\nu \rightarrow {}^1A^*$$

(3.9)

or in short,

$$^1D^* + {}^1A \rightarrow {}^1D + {}^1A^*$$

(3.10)

where superscription "1" denote the singlet state, and "$*$" depicts excited state. It is also illustrated in Figure 3.9a. In this scheme, the excited donor D^* releases an electron to the ground state, while exciting an electron from the ground state of acceptor A to a higher energy level. In the Förster energy transfer frame, the rate $k_{\text{Förster}}$ can be described as

$$k_{\text{Förster}} = k_D \left[\frac{R_0}{R_{\text{DA}}} \right]^6$$

(3.11)
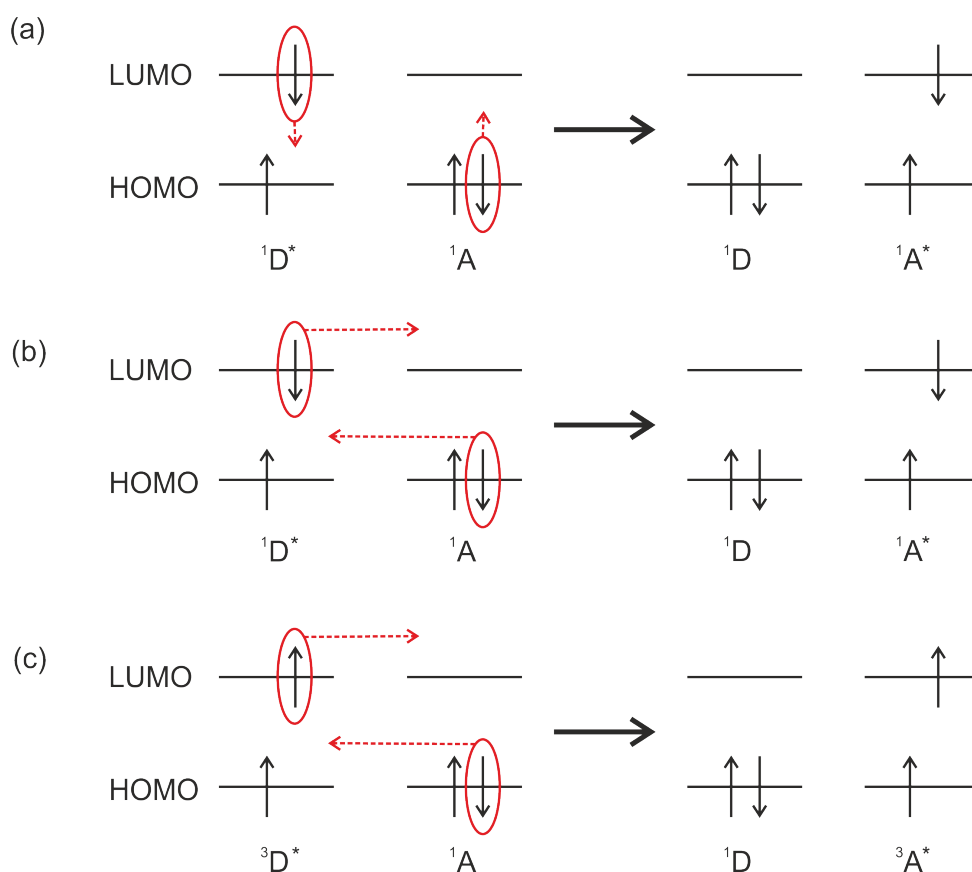
Figure 3.9: Graphic illustrations of Föster and Dexter energy transfer. (a) Föster singlet-singlet energy transfer takes place when singlet state in donor releases the energy which can be absorbed by acceptor, therefore exciting the acceptor molecule. (b) Dexter singlet-singlet energy transfer occurs via exchange coupling. (c) Dexter triplet-triplet energy between donor and acceptor molecules.[36]

where k_D is the rate constant of excited donor in absence of an acceptor, R_{DA} is the intermolecular distance between donor and acceptor, and R_0 is the critical quenching radius or Förster radius. It refers to the distance where the rate constant for energy transfer and k_D are equal, so that energy transfer and spontaneous decay of the excited donor are equally probable.[91]

Föster energy transfer generally forbids transition from a triplet state to a singlet state, since this would require two simultaneous intersystem crossing steps. However, as described above, if the molecule contains heavy metals, intersystem crossing becomes possible and transitions from the triplet state to the ground state are not prohibited. Therefore,

$$^3D^* + \,^1A \rightarrow \,^1D + \,^1A^* \tag{3.12}$$

is also allowed if phosphorescent donors are incorporated, where the transfer between the triplet state (with subscription "3") and the singlet state (with subscription "1")

is allowed. Yet there is almost no fluorescent emission from the singlet excited state in phosphorescent molecules, hence $^1A^*$ will eventually be converted to $^3A^*$ state.[11, 69]

Dexter-type Energy Transfer

Dexter energy transfer requires an orbital overlap of donors and acceptors. Excitons can then transfer from the donor to the acceptor via intermolecular electron exchange. Therefore this process occurs in short range with typically up to $1\,\mathrm{nm}$. The rate can be expressed as

$$k_{\mathrm{Dexter}} = \frac{2\pi}{\hbar} K^2 J e^{-2R_{\mathrm{DA}}/L} \tag{3.13}$$

K is a constant in units of energy. The exponential dependence on the intermolecular distance R_{DA} accounts for the necessity of molecular orbital overlap.[69] It attenuates exponentially with distance. This process also requires spectral overlap between the donor and the acceptor molecules, since the energy of both molecules should match. Most importantly, the total spin of the donor and the acceptor is conserved during the transfer process. Hence singlet-singlet and triplet-triplet energy transfers can take place.[72, 92] They can be described by

$$\begin{aligned} ^1D^* + {}^1A &\rightarrow {}^1D + {}^1A^* \\ ^3D^* + {}^1A &\rightarrow {}^1D + {}^3A^* \end{aligned} \tag{3.14}$$

The singlet-singlet and triplet-triplet transitions are graphically illustrated in Figure 3.9b and c.

3.8 Tandem OLEDs

The lifetime of OLED device is still a limiting factor for panel applications. In the OLED, a current driven light source, the luminance usually increases with the current density, and the current density is also related to the lifetime of the device. Higher currents are more likely to induce electrochemical side-reactions of organic compounds and to foster faster degradation.[93–95] Thus it is challenging to simultaneously obtain high luminance and long lifetime. One approach to overcome this limitation is the concept of tandem OLEDs, in which two OLEDs are stacked on top of each other.[5, 6, 96, 97] The schematic of a typical tandem OLED architecture is depicted in Figure 3.10. The two sub-OLEDs are connected in series via a so-called charge generation layer (CGL).

As shown in Figure 3.10, an electron and a hole are generated in the CGL. Under an external electric filed, the generated electron is transported to the bottom OLED and recombines with the injected hole from the anode, generating one photon. On the other hand, the generated hole is transported to the top emitter. Upon recombining with an
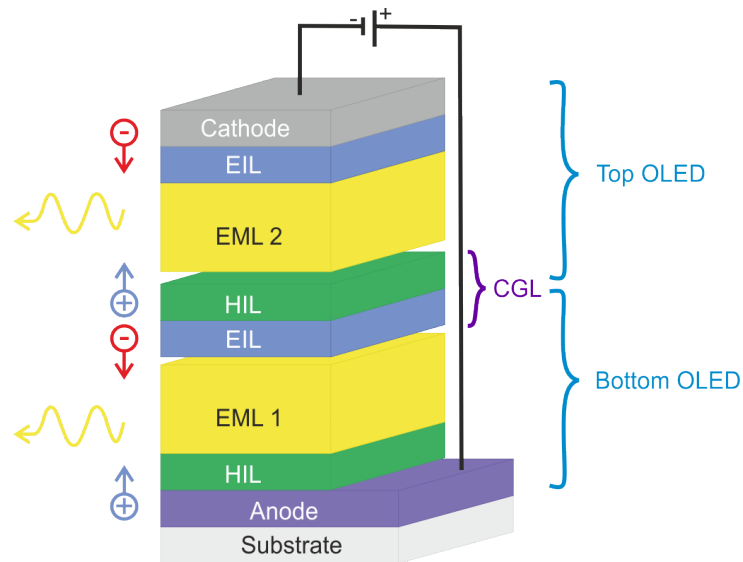
Figure 3.10: Illustration of a tandem OLED architecture, where the bottom and top devices are connected via a charge generation layer (CGL). Pairs of electrons and holes are induced in the CGL and then separated by the external electrical filed. The generated electrons recombine with the injected holes from the anode in the bottom OLED, while the generated holes form excitons with the injected electrons in the top device. Consequently two photons are simultaneously generated in the tandem device with one injected electron-hole pair.

electron from the cathode, a second photon is generated. In the ideal case, one externally injected electron-hole pair can produce two photons. At the same current density, tandem device can achieve twice the luminance of the single OLED. To obtain a certain brightness, only half of the current density of the single OLED is required in the tandem device. Consequently for the same luminance, the lower current density in the tandem OLEDs can extend the lifetime of the devices.

In addition, the tandem OLEDs provide the advantage of independent design of the two sub-OLEDs. If one emitter emits with blue color and one in orange, white light is emitted from the device. The low current density in tandem architectures can also reduce the efficiency roll-off, which is particularly important for the phosphorescent devices.[98]

A CGL comprises an electron donating (electron injection) layer and an electron accepting (hole injection) layer, mostly one p-doped and one n-doped semiconductor. When two doped materials are in contact (Figure 3.11), the Fermi levels are aligned and the vacuum level is shifted. When an external voltage is applied to the OLED stack, the CGL works under reverse bias. Then the electrons can tunnel from the HOMO of the p-doped material to the LUMO of the n-doped material, leaving holes behind. With assistance of an electric field, the electrons and holes are further driven away from each other.[99]

The electron accepting layer (or hole injection layer) can comprise n-doped transition metal oxides, such as V_2O_5, WO_3 or MoO_3, which exhibit high work functions and high transmittance in the visible range.[6, 51, 96, 100, 101] Figure 3.12 presents an example
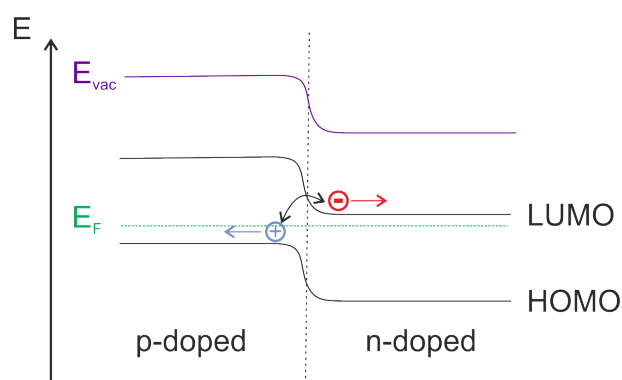
Figure 3.11: Energy diagram of a typical charge generation layer comprising one p-doped and one n-doped layer. When two materials are brought into contact, the Fermi levels are aligned and the vacuum level is shifted. An electron propagates from the HOMO of the p-doped layer to the LUMO level of the n-doped layer, leaving one hole behind. In the electric field, the holes and electrons are driven further apart.
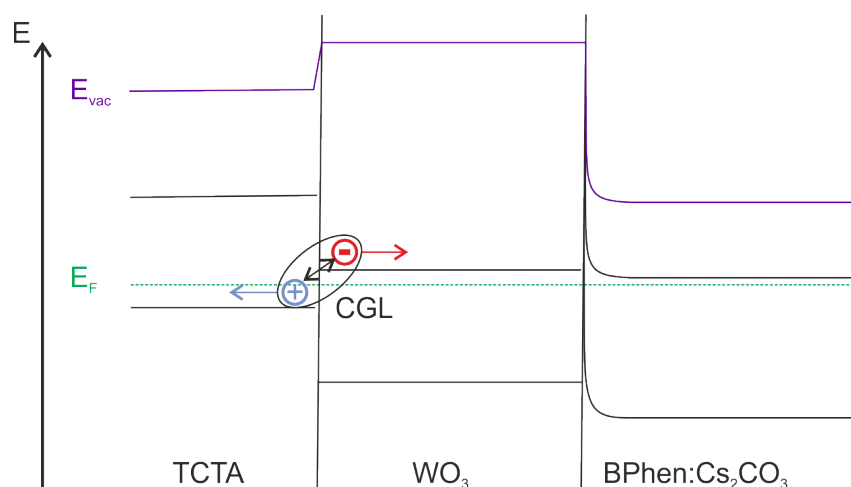
Figure 3.12: Energy alignment diagram of a charge generation layer consisting of TCTA, WO_3 and Cs_2CO_3 doped BPhen. Charge generation takes place at the interface between TCTA and the n-doped WO_3. Then the electron is further transported to electron injection layer BPhen:Cs_2CO_3, while hole is transported to the other emission layer. [102]

with WO_3 in the CGL as the electron accepting material. In this case, the common hole transport organic material tris(4-carbazoyl-9-ylphenyl)amine (TCTA) is incorporated adjacent to the n-doped WO_3, and there is a small energy difference (0.8 eV) between the conduction band of WO_3 and the HOMO of TCTA. Consequently the charge generation occurs at the interface between TCTA and WO_3. A large dipole is built at the interface between the hole transport layer and WO_3.[102] Then the generated electrons and holes can be driven apart by applied voltage. Holes will be transported to the emission layer of the first OLED, while electrons are driven to the n-type EIL (Cs_2CO_3 doped bathophenanthroline (BPhen)) of the second OLED.

2,3,5,6-tetrafluoro-7,7,8,8-tetracyanoquinodimethane (F_4TCNQ) and Lewis acids, such as iron(III) chloride ($FeCl_3$), have strong electron-accepting properties, and they can form

charge-transfer (CT) complexes with electron-donating arylamine compounds to be used in CGLs.[5, 96, 103] However, these Lewis acids are not stable and increase the driving voltage during long-term operation.[98]

The transparent ITO electrode can be sputtered as an interconnecting layer to connect sub-OLEDs in series. Yet, sputtering ITO often damages the existing organic layer beneath. Ultra-thin metals such as aluminum, silver or gold have also been presented as interconnecting layers in tandem OLEDs at the cost of transparency.[104–106] The electrons are then injected from the interconnecting electrode into the bottom light emitting unit, while holes are supplied from thin electrode into the top OLED. If the conductivity of ITO or the metal electrode is too high, crosstalk can occur between emitting pixels in display applications. In addition, inserting a metal-based layer may decrease the transmittance in the visible spectral regime.[105, 106]

3.9 Photophysical Properties

In order to compare different kinds of OLEDs, it is imperative to have some standard indicators to characterize OLEDs. The most common features of one light source include efficiency, brightness and color.

3.9.1 Internal Quantum Efficiency

The internal quantum efficiency (IQE) of a device describes the conversion efficiency of the injected charge carriers into photons:

$$\text{IQE} = \gamma \chi \eta_{\text{rad}} \tag{3.15}$$

where γ is the ratio of the electrons to holes (or vice versa) injected from each electrode. χ represents the fraction of the emissive excitons and it is usually determined intrinsically by the emitter material. As described in Chapter 3.6, in fluorescent emitters, maximum 25% of the excitons can contribute to the radiative emission, while in the phosphorescent and TADF OLEDs, theoretically 100% IQE can be achieved. η_{rad} is the effective radiative efficiency of the emitter, which can be influenced by various bimolecular annihilation processes that result in exciton quenching, such as triplet–triplet annihilation (TTA), triplet–polaron annihilation (TPA), singlet–polaron annihilation (SPA), singlet–singlet annihilation (SSA), singlet–triplet annihilation (STA), as well as exciton dissociation under the influence of heat or an electric field.[107]

Owing to the long lifetime of triplet excitons, quenching processes involving triplet excitons are more likely to occur than quenching processes involving the singlet excitons.

TTA is the most widely studied mechanism in OLEDs. In TTA, the annihilation of two triplet excitons result in an intermediate state X which can then be transferred, according to spin statistics, into one singlet, three triplet, or five quintet states.[108] The quintet states are usually neglected due to its higher energy than the two triplet states. This process can be described as

$$T_1 + T_1 \xrightarrow{k_{TT}} X \begin{cases} \xrightarrow{75\%} T_n + S_0 \rightarrow T_1 + S_0 \\ \xrightarrow{25\%} S_n + S_0 \rightarrow S_1 + S_0 \end{cases} \tag{3.16}$$
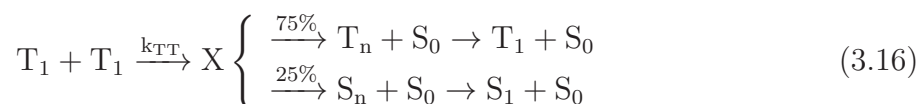
where k_{TT} is the rate constant describing the kinetics of the TTA process. The total ratio of the triplet excitons that can be converted into the singlet excitons is 15%.[109] This is an improvement for the fluorescent emitter, but in the phosphorescent emitter, the singlet excitons will be transferred back to triplet state via intersystem crossing, causing at least one exciton loss during this process.

The annihilation of excitons with free or trapped charge carriers is possible via triplet-polaron or singlet-polaron annihilation. TPA can be described as a process wherein triplets T and doublets D (the spin state of the polaron) form triplet–doublet pairs, which then transform into the singlet ground states S_0 and excited doublets D*. They can either relax into ground state doublets or ionize into free charge carriers and ground state neutral traps.[107] Nevertheless, SPA hardly influences the OLED efficiencies at moderate currents.[110]

Generally, singlet-singlet annihilation is more pronounced in crystalline than in amorphous materials because of higher diffusion constants in ordered materials.[111] Singlet-triple annihilation is negligible in phosphorescent OLEDs, as singlets undergo fast ISC to triplet states. In fluorescent materials, the singlet excited state of the donor transfers its energy to the first excited triplet state of an acceptor. After relaxation back to the T_1 level, only one triplet exciton is left.[107]

3.9.2 External Quantum Efficiency

Not all emission can escape from the device. Therefore another important criteria to characterize devices is the external quantum efficiency (EQE). It can be related to IQE via

$$EQE = \eta_{out}IQE \tag{3.17}$$

where η_{out} represents the outcoupling efficiency. Provided that the emission in the organic layer is isotropic and that the top electrode is perfectly reflective, the outcoupling fraction is

$$\eta_{out} = \frac{1}{\xi \cdot n^2} \tag{3.18}$$
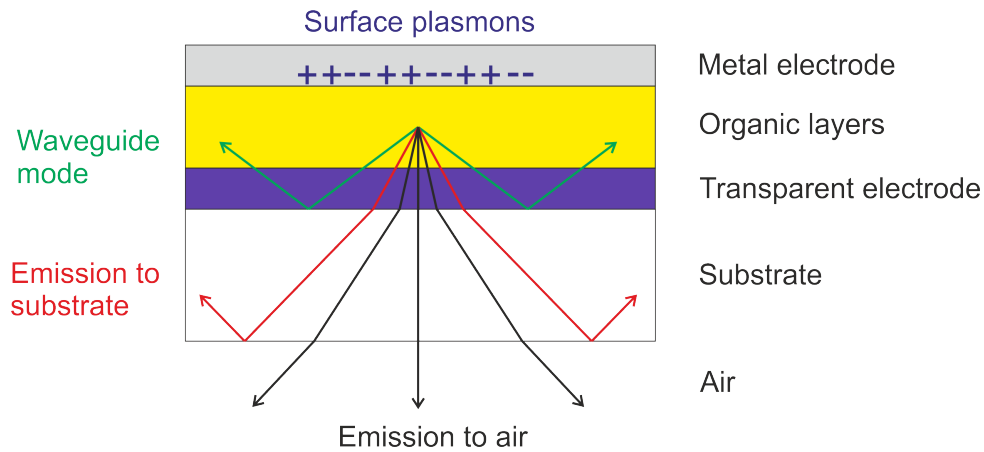
Figure 3.13: Schematic demonstration of optical loss mechanisms in an OLED device. Without any outcoupling enhancement, only a small fraction of light can pass through the substrate and be emitted to air. Most of the energy is lost to waveguide modes, surface plasmons, or substrate.[112]

where ξ is a constant depending on the dipole alignment and the geometry of the OLED device, and n is the refractive index of the OLED material.[112] For most organic materials the refractive index is around 1.7, and assuming 2 for ξ, the outcoupling efficiency is only about 20%.[113] As illustrated in Figure 3.13, other than emission into air, the light could be guided into the substrate or into waveguide modes or couple to surface plasmons.[112] Surface plasmons (SP) are induced by the interaction between free charges at the surface of the metal electrode and electromagnetic radiation. The interaction leads to surface plasmons with greater momentum, or equivalently, greater inplane wavevector than "free" photons in the emission layer. This increased momentum (inplane wavevector) imply that they cannot be coupled to a free space mode. Thus SP modes on flat surfaces are nonradiative, and they are bound to the interface between the metal and the organic material.[114]

Waveguide mode is very low for very thin ETLs (the layer between emitter and metal electrode), but with increasing thickness it is strongly enhanced, since there is a minimum layer thickness for an asymmetric waveguide to own a waveguide mode. Above this limit, an increasing amount of modes can exist for larger thicknesses. On the contrary, SP modes are strong with thin layers and get reduced with increasing layer thicknesses. As a result, SP and waveguide modes cause in total around 50% loss, which is almost independent of ETL thickness.[112]

Another part of the energy is emitted to the substrate, and this process takes place at the interface between substrate and air. According to Snell's law, when light propagates from one medium with refractive index of n_1 to another medium with different refractive

index of n_2, light is partially reflected and partly refracted. The relationship between the incident angle (θ_1) and the refractive angle (θ_2) is described by

$$n_1\sin\theta_1 = n_2\sin\theta_2 \tag{3.19}$$

If $n_1 > n_2$, a critical angle θ_c exists,

$$\theta_c = \arcsin(\frac{n_2}{n_1}) \tag{3.20}$$

if the incident angle equals the critical angle, the angle of refraction is 90°. Any incident light which has a larger angle of incidence than the critical angle will not be refracted anymore. Thus total internal reflection takes place. The critical angle for glass substrate and air can therefore be calculated $\theta_c = \arcsin(1/1.5) = 41.8°$. Any emission at larger incident angles is coupled into substrate modes and accounts for around 30% loss of the total energy.

3.9.3 Photometry and Radiometry

To characterize the emission from an OLED, both electrical and optical characteristics should be taken into consideration. Besides quantum yield, another critical feature to characterize an OLED emission is the brightness to human eyes. Human eyes have different sensitivities to different wavelengths, and the sensitivity changes between day and night. As depicted in Figure 3.14, the red curve shows the human eye sensitivity to different wavelengths of daylight. The peak is 683 lm/W at 555 nm, that means human eyes are more sensitive to green light than to red or blue under daylight. When background luminance becomes low, the eyes will adapt to scotopic vision. Consequently, human eyes become most sensitive to green-blue colors around 500 nm.

Light sources can be characterized either in radiometric units or photometric units. In photometric units, the spectral sensitivity of the human visual perception of brightness is taken into consideration. Table 3.1 compares the common radiometric and their corresponding photometric units. The photometric data can be calculated from the recorded radiometric data.

The luminous flux (Φ_v) is the quantity of energy emitted by a light source per unit time in all directions, and it can be calculated via

$$\Phi_v = K_m \int_{\lambda_{min}}^{\lambda_{max}} \Phi_{e\lambda}(\lambda)V(\lambda)d\lambda \tag{3.21}$$

where $\Phi_{e\lambda}$ describes the power distribution versus wavelength. $K_m = 683$ lm/W is the highest human eye sensitivity to light during photopic vision. $\lambda_{min} = 380$ nm and $\lambda_{max} =$
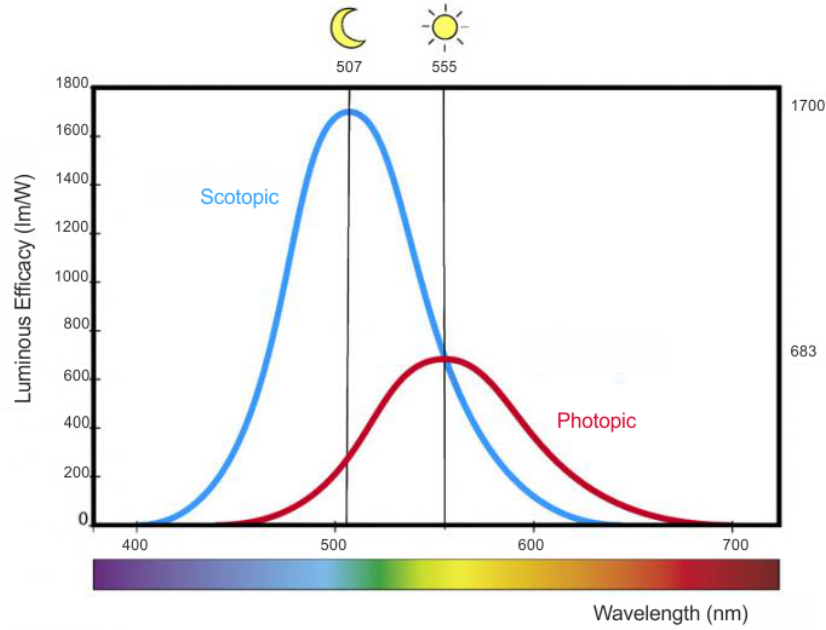
Figure 3.14: The red curve corresponds to human eye sensitivity to various wavelengths during day time (photopic vision). Human eyes are more sensitive to green color than red and blue. At low light conditions (scotopic vision), the highest sensitivity peak is blue-shifted to around 500 nm.[115]

Radiometry	Unit	Photometry	Unit
Radiant flux (Φ_e)	W	Luminous flux (Φ_v)	lm
Radiance (L_e)	W/m^{2}sr	Luminance (L_v)	cd/m^2
Radiant intensity (I_e)	W/sr	Luminous intensity (I_v)	cd
Irridiance (E_e)	W/m^2	Illuminance (E_v)	lx = lm/m^2

Table 3.1: Comparison of the radiometric and the corresponding photometric units of a light source. The photometric data takes human eye sensitivity into consideration.

780 nm define the wavelength range that human eyes can detect. $V(\lambda)$ describes the spectral sensitivity of the human eye during photopic vision, and it becomes 0 if the wavelength is smaller than 380 nm or larger than 780 nm. In reality, the absolute luminous flux is measured in an integrating sphere.

Luminous intensity (I_v), of which the unit is candela, describes the luminous flux from a light source into a given direction within the unit of the spatial angle. Therefore it can be calculated by

$$I_v = \frac{d\Phi_v}{d\lambda} \tag{3.22}$$

The luminance L_v represents the luminous intensity per unit area of light traveling in a given direction. It can be related to the luminous flux Φ_v by

$$L = \frac{dI_v}{dA \cdot \cos\epsilon} = \frac{d^2\Phi_v}{d\omega \cdot dA \cdot \cos\epsilon} \tag{3.23}$$

where A represents the area of the emitting surface, and $d\omega$ is the solid angle (sr). ϵ describes the angle between the axis perpendicular to the emitting surface and the axis of the viewer. Likewise, it is also possible to deduce the luminous flux from a known luminance distribution. For a Lambertian emitter, the luminous flux is not dependent on the viewing angle and the total flux of an area A into the half space is then given by

$$\Phi_v = \pi \cdot A \cdot L_v. \tag{3.24}$$

In reality, an ideal Lambertian emitter does not exist, but it is a good approximation. Other than the absolute luminous flux and luminance, it is important to characterize the yield of devices based on the sensitivity of human eyes. The power efficiency (η_p) of the light source can be calculated from the ratio of the luminous flux and the applied electrical power:

$$\eta_p = \frac{\Phi_v}{I \cdot V} \tag{3.25}$$

where I and V represent the corresponding current and voltage applied on the device to achieve the flux Φ_v. The current efficiency (η_c) is defined as the fraction of luminance to current density (J),

$$\eta_c = \frac{L_v}{J}. \tag{3.26}$$

The current efficiency describes the conversion fraction of injected charge carriers into light as perceived by human eyes. It is independent of the operating voltage and allows to judge, for example, injection losses of OLEDs.

3.9.4 Color

Besides the brightness to human eyes, the device color is also important to describe OLEDs. Human eyes possess three kinds of cones and they have sensitivity peaks at short, middle, and long wavelengths respectively. Since it is difficult to determine the spectral sensitivities of different cones directly, in 1931, three primary light (700 nm, 546.1 nm, 435.8 nm) was mixed together in order to match the test color, which comprises only one single wavelength. The amounts of each primary color used to match the test color were then recorded and known as CIE RGB color matching functions. Yet negative values appeared in this case. To simplify further calculations, positive standard observer matching functions are mathematically simulated. The primaries, in this case, do not exist anymore.

If the spectral power distribution $\phi(\lambda)$ of an emission is given, the standard tristimulus values X (a linear combination of cone response curves chosen to be nonnegative), Y (luminance) and Z (quasi-equal to blue stimulation) can be calculated as follows:
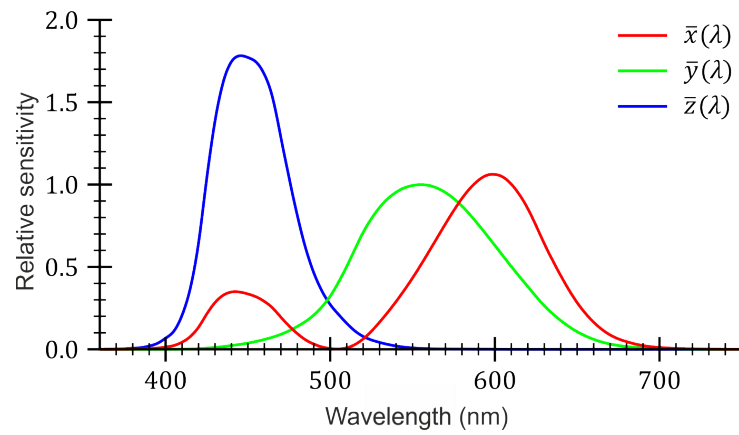
Figure 3.15: The CIE standard observer color matching functions.[116]
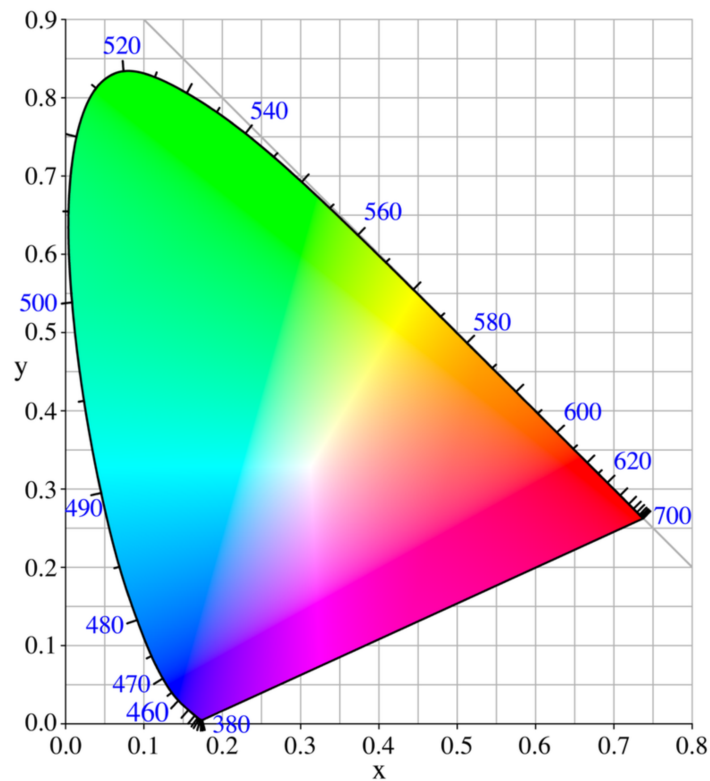
Figure 3.16: The CIE 1931 color space chromaticity diagram. The curved edge of the gamut corresponds to monochromatic light, and the wavelengths are indicated in nanometers. The white color is at the center, where x = y = 1/3 (achromatic).[117]

$$X = k \cdot \int \phi(\lambda) \cdot \bar{x}(\lambda) \cdot d\lambda$$

$$Y = k \cdot \int \phi(\lambda) \cdot \bar{y}(\lambda) \cdot d\lambda \qquad (3.27)$$

$$Z = k \cdot \int \phi(\lambda) \cdot \bar{z}(\lambda) \cdot d\lambda$$

where $\bar{x}(\lambda)$, $\bar{y}(\lambda)$ and $\bar{z}(\lambda)$ are the numerical descriptions of the chromatic response of the standard observer (Figure 3.15). $\bar{y}(\lambda)$ is exactly the same as the spectral sensitivity of the human eye.[118, 119]

As shown in Figure 3.16, the CIE XYZ color space contains colors visible colors to a person with average eyesight. The color of a light source can be illustrated as a dot in the CIE color space. The chromaticity of a color can be specified by the two parameters x and y that are functions of tristimulus values X, Y and Z:

$$x = \frac{X}{X+Y+Z}$$
$$y = \frac{Y}{X+Y+Z} \qquad (3.28)$$

The edge curve is called spectral locus and indicates the monochromatic color with only one single wavelength. In the center of the color space (x = y = 1/3) is the white color.

4 OLED Fabrication and Chracterization

4.1 Layer Deposition

Since the thicknesses of all the functional layers in OLEDs are in the nanometer range, dust particles would most likely lead to failure of the devices. Hence, all the experiments are conducted in the cleanroom at Light Technology Institute (LTI) and Material Research Center for Energy Systems (MZE). Both cleanrooms consist of rooms of different classes, which are defined by the maximum allowed amount of particles per volume atmosphere. The substrates are cut and etched in the room with class 100,000, noting that less than 100,000 particles of size 0.5 µm or larger are permitted per cubic foot of air. Prior to further layer depositions, all the precut samples are cleaned in acetone and isopropanol in ultrasonic bath for 10 minutes each. Oxygen plasma is applied after cleaning in order to remove any potential organic residuals. In addition, if the following layer is deposited from polar solvents, oxygen plasma can polarize the ITO surface for better adhesion. However, most organic functional materials are sensitive to oxygen and water in air. Therefore the device fabrications and characterizations are accomplished in the gloveboxes filled with nitrogen if not specified. Some thin-film characterizations, including microscope and stylus profilers, are performed in a room of class 1,000.

Spincoating

The simplest approach to realize homogeneous thin-films from solution is the utilization of a spincoater. The samples are placed on a chuck and fixed by vacuum during rotation. Then a certain amount of solution is taken by a pipette and dropped onto the substrate. The solution is then spread over the entire substrate by centripetal forces during spinning. The solvent used to dissolve the organic semiconductors is usually volatile. Therefore it evaporates during the spinning process, leaving a dry film behind. Depending on the solvent used, sometimes, an annealing step may be necessary to dry the film completely. The layer thickness (d) of the dried film is related to many parameters, including physical
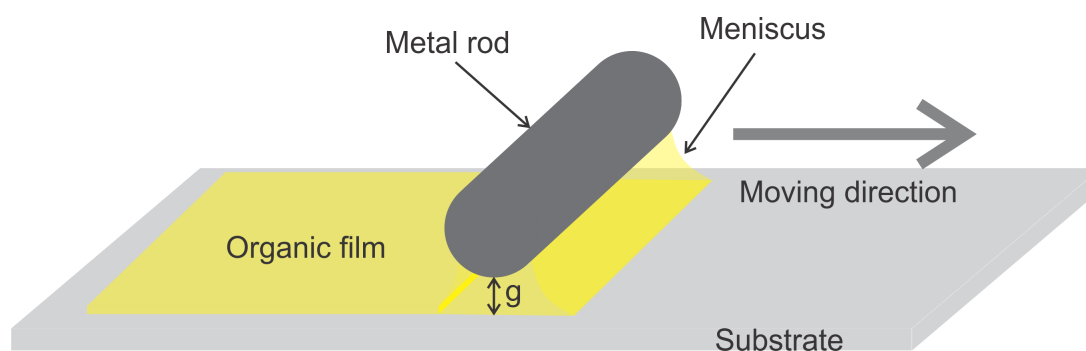
Figure 4.1: Schematic illustration of H-dipping. The organic film is left behind the moving metal rod.

properties of solute, solvent, substrate, as well as, according to the following equation, the angular velocity (ω)

$$d = k\omega^{\alpha} \tag{4.1}$$

where k and α are empirical constants. A typical value for the exponent α is -0.5.[120]

Horizontal-Dipping

Although spincoater is widely used in the lab to form homogeneous thin layers, horizontal dipping (H-dipping) owns unique advantages when it comes to large area device fabrication. Unlike spincoating, the loss of coating solution in H-dipping can be minimized to 5%. Hence, for large-area substrates, the required minimum amount of solution in H-dipping deposition is much lower than in spincoating. Furthermore, the H-dipping parameters can be rather easily transferred to roll-to-roll process. As demonstrated in Figure 4.1, a horizontal metal rod (coating barrier) is placed at a fixed distance (g) above the substrate. The coating solution, dropped in front of the rod, is distributed across the substrate upon moving the coating barrier, leaving a wet film behind.[121] Back in 1942, Landau and Levich have already proven that the thickness of the layers formed by dragging a plate with liquid is dependent on the coating solution, drawing speed as well as the meniscus.[122] Hence, wedge shaped organic films can be obtained by modifying the moving speed of H-dipping metal rod. In order to study the layer thickness influence on devices, wedge-shaped layers are deposited by utilizing a H-dipping machine (Zehntner ZAA2300).[123]

Vacuum Evaporation

Thermal evaporation (Model: Spectros, Kurt J. Lesker) is used to deposit metal electrodes and sometimes organic charge carrier transport layers under high vacuum (10^{-6} mbar).
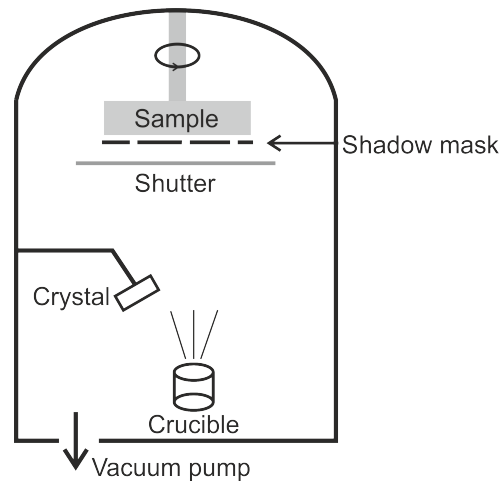
Figure 4.2: Simplified illustration of the evaporation chamber. High vacuum is achieved via vacuum pumps. The materials evaporate when the source is heated up, and the layer thickness is monitored by the crystal. The substrate shutter is open during film deposition and closed when the thickness is reached. The metal mask beneath the sample is to assure film deposition onto specific areas on the substrates. The samples together with the mask are rotated during evaporation to assure homogeneous film deposition.

The systems comprises a 3-step pumping system of a rotary vane pump, a turbopump and a cryopump. A simplified schematic graph of the evaporation chamber is depicted in Figure 4.2. The metal and dielectric sources are heated by high currents of up to 400 A, while organic materials are heated in temperature-controlled effusion cells. The samples are placed above the evaporation source with a shadow mask fixed beneath. The substrates along with the mask rotate during evaporation to assure uniform film deposition. The shutter opens when the desired evaporation rate is reached and closes when the desired thickness is achieved. Deposition rate and thickness are monitored by a quartz crystal microbalance, on which the film mass variation is reflected by the frequency change in the quartz resonator.

4.2 OLED Layout Design

All the samples in this work are fabricated either on glass or PET substrates. ITO sputtered on glass substrates (d = 1 mm) is purchased from Luminescense Technology Corp., and it has a sheet resistance of $R_\square = 12\,\Omega$. The substrates are patterned via photolithography. A positive photoresist (ma-P 1215) from Microresist Technology is spincoated on the entire substrate, followed by a soft baking procedure at 100 °C for 90 s. Afterwards, the sample covered with a mask is radiated under ultraviolet (UV) light. Then the sample is dipped into a developer solution (maD 331) for 35 s. Hard baking at 100 °C is necessary before the sample is rinsed in hydrochloric acid (37%) for 7 minutes to remove all the ITO areas which are not illuminated by UV light, while protecting the
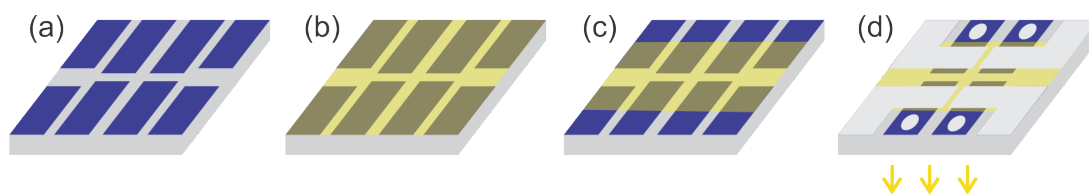
Figure 4.3: Illustration of the standard design with a substrate with size of 25 mm × 25 mm. (a) The bottom electrode (ITO) is patterned on the glass substrate. (b) Following functional layers are deposition on the entire substrate. (c) To access the bottom electrode, parts of the deposited layers are removed. (d) The top electrode is evaporated through a metal shadow mask.
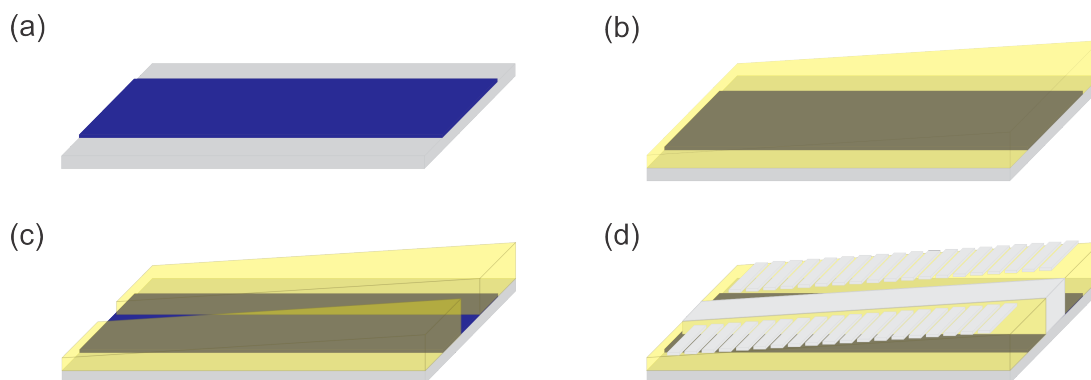
Figure 4.4: The schematic fabrication steps of OLED arrays on glass substrates of 25 mm × 75 mm. (a) The bottom ITO electrode is patterned to 15 mm × 75 mm. (b) The wedge-shaped functional layer is applied with increasing film thickness from left to right. (c) In order to access the bottom electrode, the very middle of the functional film is removed. (d) The final metal electrodes for 38 OLED pixels are evaporated through a shadow mask.

desired ITO patches by the photoresist.

Standard OLEDs

In the standard layout, all glass samples are cut into 25 mm × 25 mm pieces with a glass cutter. Figure 4.3a demonstrates the pattern of ITO after photolithography. All the following functional layers are deposited on the entire substrate by spincoating or H-dipping (Figure 4.3b). In order to contact the bottom electrode in the characterization setup, the functional layers at the edges need to be removed before the top electrode deposition (Figure 4.3c). At the end, the top electrode is evaporated through a metal mask (Figure 4.3d), eventually forming four OLED pixels with size of 5 mm × 5 mm on each substrate, where the top and bottom electrodes overlap. With a transparent bottom electrode and an opaque top electrode, the generated photons will be coupled out through the glass side.

OLED Arrays with Wedge-shaped Emission Layer

The OLED arrays with wedge-shaped emission layer are designed have in total 2×19 pixels, each with a size of $2\,\text{mm} \times 4.5\,\text{mm}$ on one single substrate. The glass substrate has a size of $25\,\text{mm} \times 75\,\text{mm}$, and the ITO electrode is patterned to cover an area of $15\,\text{mm} \times 75\,\text{mm}$ (Figure 4.4a). After cleaning the bottom electrode, the functional layers with increasing thicknesses along the substrate are deposited (Figure 4.4b). In order to electrically connect the bottom electrode with the measurement setup, the middle part of the functional layer is scratched away as illustrated in Figure 4.4c. Finally, the top metal electrodes are deposited via thermal evaporation, defining 38 OLED pixels on each substrate (Figure 4.4d).

Transparent OLEDs

Both the standard OLEDs and the wedge shaped OLEDs incorporate metal electrodes which are deposited on top of the devices through metal shadow masks. A different OLED design is used for the transparent devices where both bottom and top electrodes are transparent. Like the other functional layers, the transparent top electrode is also deposited from solution. As depicted in Figure 4.5b, all layers including the top electrode are deposited on the entire ITO substrate without any patterning. In order to achieve defined active areas, three dicing tapes are sticked to the top electrode and removed afterwards, so that the covered parts of top electrode are removed together with dicing tapes. In order to access the bottom electrode, the functional layers at the edges are removed. Silver ink is applied on the sample to ensure better contact with the measurement setup. Each substrate carries in total four pixels with an active area of $5\,\text{mm} \times 5\,\text{mm}$, and light can be emitted through both the top electrode and the glass substrate.

Flexible OLEDs

In addition to the ITO coated glass substrate, an OLED layout on the mechanical flexible PET substrate ($d = 50\,\text{µm}$) is designed in order to realize all-solution processed transparent OLEDs, in which both bottom and top electrodes are spincoated from solutions. The substrate is cut into $25\,\text{mm} \times 25\,\text{mm}$. As shown in Figure 4.6a, part of the area is covered with the pre-patterned silver mesh, which is connected to two silver pads at the edges to ensure better contact. Because silver is sensitive to oxygen, in this case no O_2 plasma is applied. Since the PET substrate is very thin and flexible, for easier spincoating, it is attached to a polydimethylsiloxane (PDMS) stamp which is fixed on
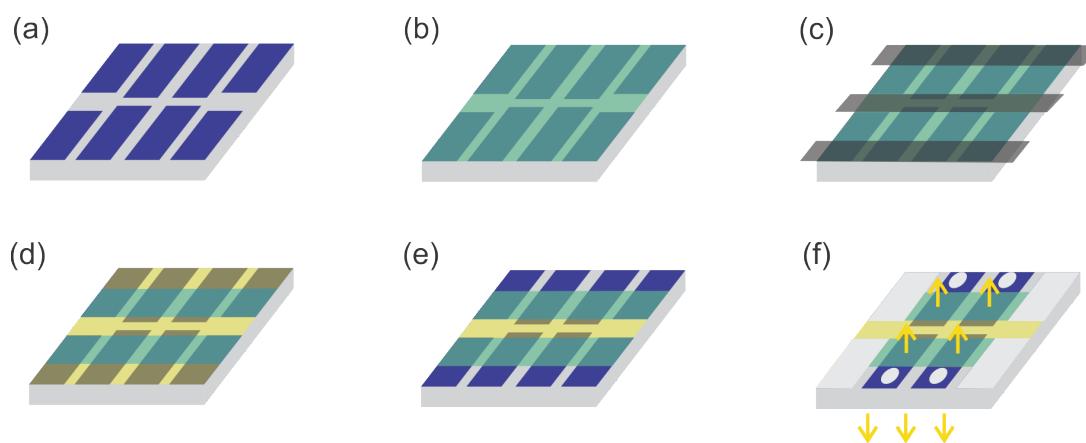
Figure 4.5: Fabrication steps of the transparent OLEDs on the substrate of $25\,\text{mm} \times 25\,\text{mm}$. (a) The bottom ITO electrode is patterned. (b) All layers (including the top electrode) are coated on the entire substrate. (c) Three dicing tapes are applied on the deposited top electrode. (d) By removing the dicing tapes, the top electrodes are also patterned. (e) The other layers are then scratched to access the bottom electrode. (f) Silver ink is applied to improve the contact with the electrodes.

a glass substrate. The bottom electrode is spincoated on the substrate (Figure 4.6b), followed by dicing tape patterning (Figure 4.6c). Likewise, all the other functional layers are deposited on the entire substrate including the top electrode (Figure 4.6d and e). The top electrode is also patterned using dicing tape to define active areas of $5\,\text{mm} \times 5\,\text{mm}$ each (Figure 4.6d). To access the bottom electrode, the functional layers are removed by swiping with solvents (Figure 4.6g). Similarly, the silver ink is applied (Figure 4.6h). Each substrate carries two transparent pixels. Before characterization, the substrate is detached from the PDMS stamp.

4.3 Layer Characterization

Optical Microscope

In order to monitor the film surface, a reflected light microscope (Axioplan 2) from Carl Zeiss AG was utilized. Light from the lamp passes through an aperture and is focused onto the specimen. Then the light beam is reflected from the surface of the sample and re-enters the objective. Finally, the reflected light is directed either to the eyepieces or a camera.

Stylus Profiler

The organic layer thicknesses are essential to the performance of the devices. A stylus profiler (DektakXT, Bruker Corporation) is used to determine the film thicknesses with
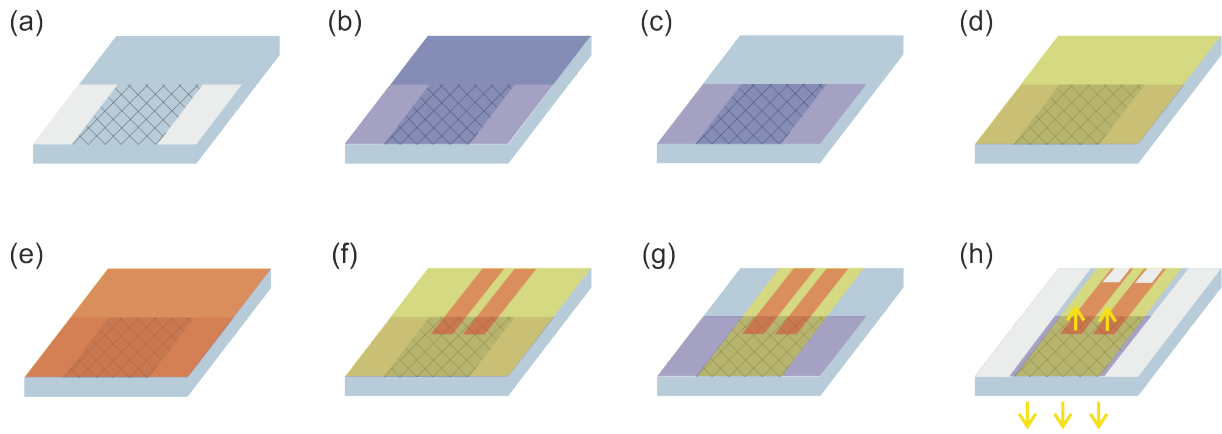
Figure 4.6: Fabrication of the transparent OLEDs on a PET substrate of 25 mm × 25 mm. (a) The silver mesh was pre-patterned on the substrate which is represented by the grid. The white areas at the edges are silver pads. (b) The bottom electrode is spincoated on the entire substrate. (c) To pattern the bottom electrode, it is partly removed by using dicing tape. (d) All layers are sequentially deposited on the entire substrate. (e) The top electrode is obtained from spincoating. (f) Top electrodes are patterned by dicing tapes. (g) The functional layers at the edge are carefully removed by wiping with solvent, leaving the bottom electrode uncovered. (h) Silver ink is applied to improve the electrical contact with the characterization setup.

a precision of a few nanometers. It uses a diamond stylus to move laterally at the surface with specific force, producing one-dimensional height profiles. Usually it is necessary to make a scratch on the sample before measurement, so that when the stylus scans from the film to the bottom of the scratch, it detects the height difference, which is the layer thickness. The stylus force can be chosen between 1 mg and 15 mg, and the value is critical to the result. Strong forces might promote penetration of the stylus into the film, producing false thickness values.

Atomic Force Microscope (AFM)

The profilometer scans the height information only in one dimension, while the atomic force microscope (AFM) scans the height variation of the entire surface (2 dimensional). The AFM (Dimension ICON, Bruker Corporation) enables the layer topography characterization in the nanometer range. A tip is mounted on the cantilever which can scan the surface in lateral and vertical directions by adjusting the voltage applied on the piezo actuator. A laser beam from a laser diode is reflected on the backside of the cantilever and is detected by a four-quadrant photodiode. In proximity of the surface, the cantilever interacts with the surface and gets deflected from its original position. This deflection causes variations on the photodiode. Contact mode is the primary approach to get high resolution images, yet the constant tip-sample contact might compromise the soft organic films. Therefore, tapping mode is applied to collect the topographic information. As depicted in Figure 4.7, the cantilever oscillates at its
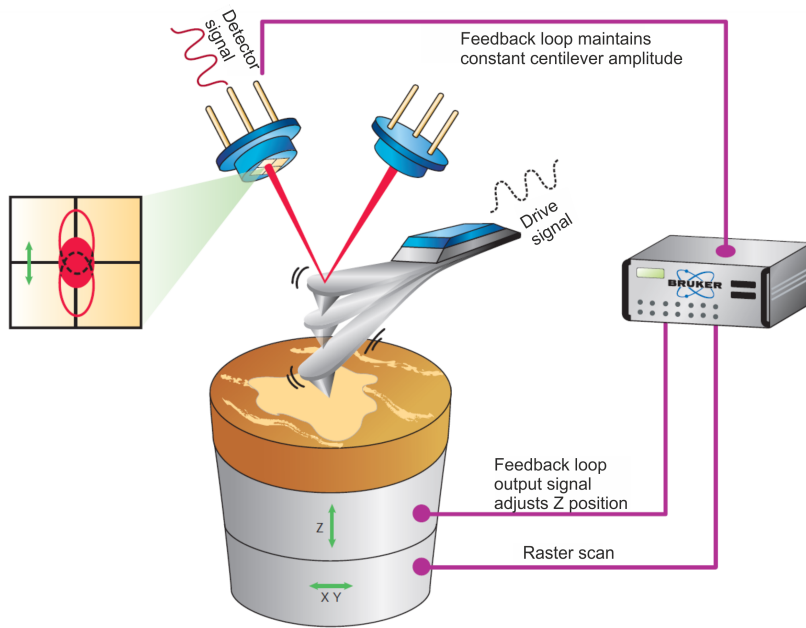
Figure 4.7: Schematic of the AFM in tapping mode. The laser beam from a laser diode is reflected by the backside of cantilever. The cantilever oscillates at its resonance frequency. When interacting with the sample surface, the resonance frequency is changed. The phase or amplitude change can be detected by a photodetector and is used as feedback loop to adjust the scan height.[124]

resonance frequency. When it approaches the surface, the tip-sample interaction changes the amplitude and frequency of this oscillation. The feedback loop can then use the amplitude or phase lag variations to adjust the scan height of the piezo actuator and track the sample surface.
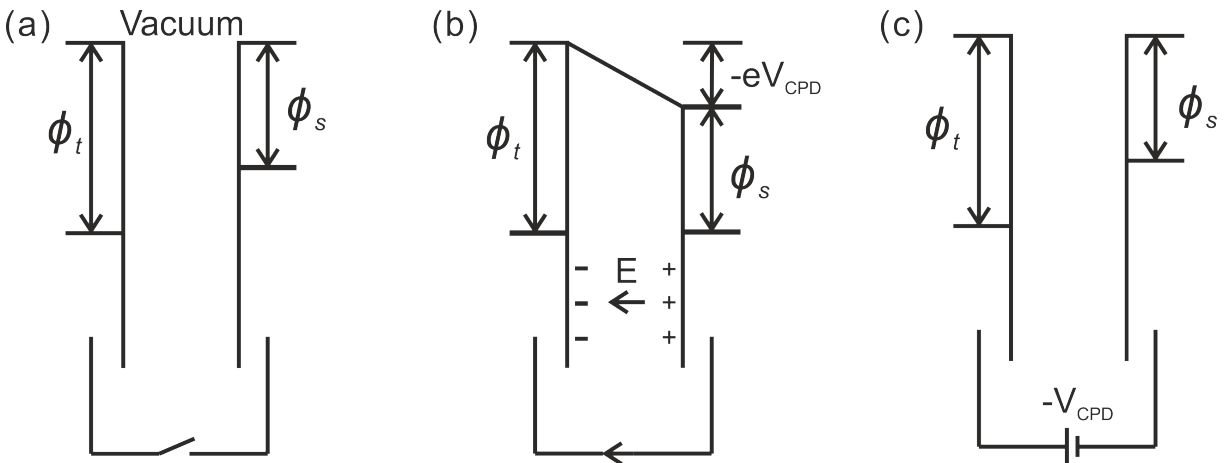
Figure 4.8: Energy diagram to illustrate KPFM measurements. (a) The tip and the sample have different work functions ϕ_t and ϕ_s. (b) When the tip approaches the sample surface, electrons flow from the tip to the sample to align the Fermi levels. (c) KPFM measurement setup adjusts the applied bias voltage so that the electric field between the tip and the sample is compensated.[125]

Other than the layer topography, the electrical properties, such as contact potential difference (CPD) can be determined via AFM. Kelvin probe force microscopy (KPFM) uses AFM to measure the local CPD between the AFM tip and the sample surface. The principle is illustrated in Figure 4.8. The tip and the sample have different work functions, ϕ_t and ϕ_s. When they are electrically connected to each other, the electrons flow from the material with the lower work function to the other one so that the Fermi levels of both are brought into the same level. Therefore, the opposite charges accumulated at on the surface, and an electric field and a CPD is built up at the interface (Figure 4.8b). Then an external direct current bias (-V_{CPD}) is applied to eliminate the electric field between the tip and sample.[125] Consequently, if the CPD between the tip and a reference sample with known work function is given, the absolute work function of other unknown materials can be deduced. Very often, a highly oriented pyrolytic graphite (HOPG) with a work function of $\Phi = 4.4\,eV$ is used as the reference to deduce the work function of the sample.[126]

UV-Vis-NIR Spectrometer

Absorption spectra can be used to determine the optical bandgap of organic semiconductors, as the absorption starts when the incident photon energy is larger than the bandgap. UV-Vis-NIR spectrometer (Cary 5000, Agilent Technologies AG) measures the transmittance with a double beam system, where one light beam firstly goes through a monochromator before it is split into two beams. The two beams go through a reference and a measurement sample separately. Then they are detected and compared. In this setup, it is also possible to measure the transmittance by using an integrating sphere. The sample is placed in front of the integrating sphere. After the beam goes through the sample, all light that passes through the sample is collected and again compared with the reference beam. In this setup, light that is emitted at an angle is also taken into account. The wavelengths range from the near infrared at of 3330 nm to the UV region of 175 nm. By comparing the intensity difference of the beams behind reference and measurement samples, the transmittance T can be determined. It is well known that the transmittance, absorbance A and reflectance R add up to 1. Therefore for weak reflecting samples, where reflectance can be neglected, the absorbance A can be calculated via following equation

$$A = 1 - T \tag{4.2}$$
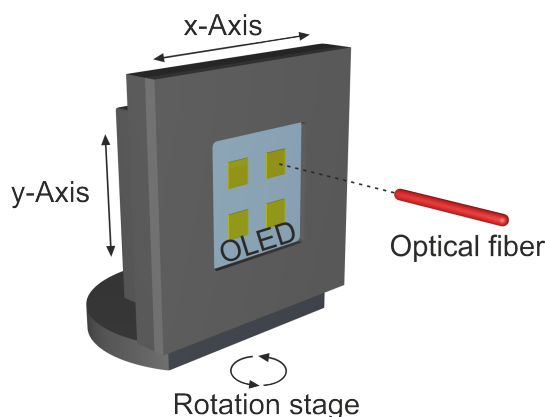
Figure 4.9: Schematic of the homebuilt optoelectronic characterization setup (OCS). One substrate with four OLED pixels is fixed in the sample holder that is mounted on a rotation stage. In front of the holder, an optical fiber couples the emission from each pixel into a calibrated spectrometer. The stage can move in x- and y-axis in order to subsequently point the fiber at a series of pixels.[62]

Photoelectron Spectroscopy in Air (PESA)

During the photoelectron spectroscopy in air (PESA) measurement, UV light with increasing photon energy is applied onto the sample. Beyond a certain threshold, electrons are ejected from the sample surface and are accelerated by a suppressor grid and then a quenching grid. During the acceleration process, the electrons ionize oxygen (O_2) and form O_2^- ions. The ions are further accelerated to the anode because of the electric field between the quenching grid and the anode. As long as the O_2^- ion reaches near the anode, the electron will be detached from the ion. It is accelerated again towards the anode. Due to the high potential of the anode, the accelerated electron results in an electron avalanche, inducing many electrons that are collected on the anode. Afterwards, the electrons are detected and counted as an electric pulse with one photoelectron entering the counter. The ionization potential and the Fermi level of metals are identical, therefore the measured value also represents the work function. In the case of an un-doped organic semiconductor, PESA determines its HOMO level.[127]

4.4 Device Characterization

4.4.1 Optoelectronic Characterization Setup (OCS)

Most of the OLEDs are characterized on a homemade optoelectronic characterization setup (OCS) in a glovebox filled with nitrogen, so that the samples are protected from air during the measurements.[128] In this setup, substrates of up to $25.5 \, \text{mm} \times 25.5 \, \text{mm}$ can fit into the sample holder. As illustrated in Figure 4.9, the holder is mounted on a
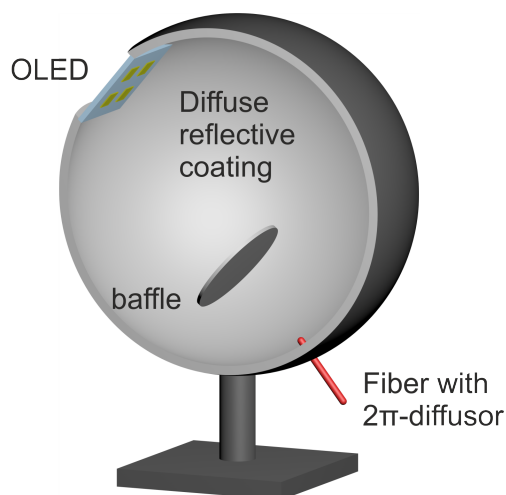
Figure 4.10: In the integrating sphere setup, the OLED substrate is fixed on a holder and put on the sphere, which is coated with diffusive reflective material on the inside. A fiber with a 2π diffuser couples the emission out. The baffle between the sample and the fiber is to prevent the direct OLED emission from reaching the fiber port.[62]

rotation stage so that angle-dependent measurements are possible.[62] The OLEDs are electrically driven and characterized by a source measurement unit (SMU, Keithley 238, Keithley Instruments LLC). A fiber centered in front of the pixel couples the OLED emission into a calibrated spectrometer (StellerNet Inc, EPP2000). The stage can move in x and y directions, so that all four pixels on one substrate can be sequentially measured automated. During the measurement, the respective pixel is driven by a voltage and the corresponding optoelectronic properties are recorded. Afterwards, the stage moves to the next OLED pixel, and the same measurement is conducted until the last pixel. To calculate the luminance and efficiencies, all OLEDs are considered to have Lambertian emission pattern.

4.4.2 Integrating Sphere

The OCS only measures the front emission, while the integrating sphere can be used to measure the total flux. The integrating sphere is also located in a glovebox. Likewise, the pixels are electrically operated and measured by an SMU (Keithley 2400, Keithley Instruments LLC). All pixels can be switched on and off separately by a multiplexer.

A schematic of the integrating sphere is depicted in Figure 4.10, where the sample is placed on the sphere.[62] The sphere is coated with white reflective material, in this case Teflon, so that the visible light experiences more than 99% diffusive reflectance when hitting at the surface. An optical fiber with a 2π-diffuser is mounted at the sphere, and it connects with a calibrated spectrometer (CAS 140CT, Instrument Systems GmbH) on the other side. In the sphere, it is critical that all light is diffused before leaving through
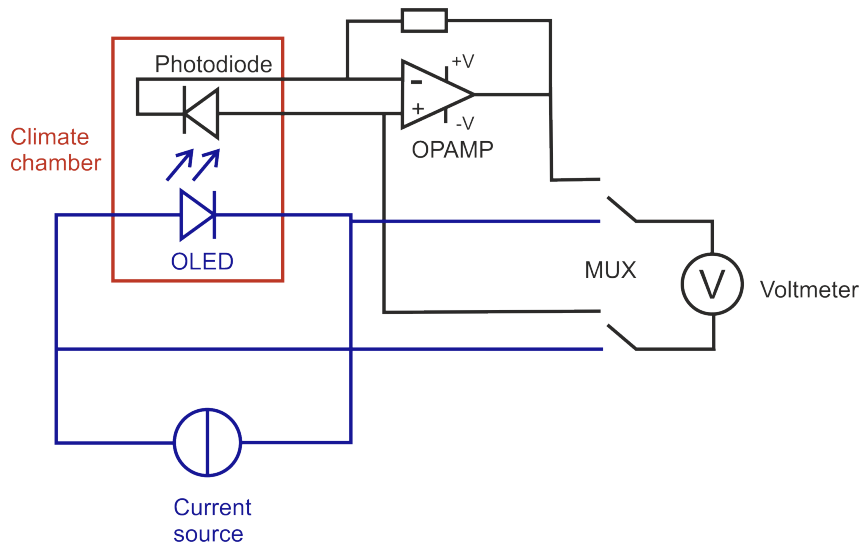
Figure 4.11: Design of the home-built OLED lifetime measurement setup. The OLED together with a photodiode are kept in a climate chamber during characterization. The OLED is driven by a current source and its voltage can be measured by a voltmeter. The current generated in the photodiode is converted into a voltage and is amplified by an operational amplifier. This voltage signal can also be recorded by the same voltmeter. The multiplexer (MUX) connecting voltmeter can switch between OLED voltage and the amplified photodiode signal.

the output port, so that the emission direction has no influence on the detected intensity anymore. Hence, a baffle is mounted between the sample and the fiber, preventing direct OLED emission to reach the fiber. In this configuration, the fiber collects all the photons emitted into all directions and hence measures the total power of one pixel.

4.4.3 Lifetime Measurement Setup

In order to characterize the stability of the OLEDs, lifetime measurements are conducted. The samples are put into a climate chamber (RS-Simulatoren Group, Klimaprüfschrank KS 320/75) which provides an environment with constant temperature and humidity. To prevent potential damage from oxygen and water, the samples are encapsulated in the glovebox. The encapsulation glass is in total 1 mm thick with a 0.5 mm thick cavity in the middle. The encapsulation glass has a size of 25 mm × 18 mm, and it covers the four pixels of the standard OLED layout. UV curable glue (KOTIOBOND LP686, DELO GmbH & Co. KGaA) is applied at the edge of encapsulation glass which is then put on top of the substrate. Then the substrate together with encapsulation glass is illuminated with UV light for 15 min. The glue must not contact the active areas, so that the pixels will not be influenced by the glue.
As depicted in Figure 4.11, the OLEDs are operated with a current source (National Instruments NI 9265, 0 mA-20 mA). During the measurements, a constant current is applied onto each pixel. Its corresponding voltage can be recorded by a digital multimeter

(Keysight 34465A, Keithley Instruments LLC). To determine the emission intensity change over time, a photodiode (BPW 34B, Osram Licht AG) is brought on top of the pixel. If the spectrum does not change over time, the respond current of the photodiode is linearly related to the emission intensity. Yet, the generated current is usually low. Therefore it is necessary that the low-level current goes through a transimpedance amplifier by using an operational amplifier (OPAMP), so that the current is converted into a voltage, and at the same time is amplified. Thus, the voltage magnitude indicates the OLED emission intensity. This voltage can be recorded by the same multimeter through a multiplexer (Keysight 34922A, Keithley Instruments LLC), so that the voltmeter can switch between the voltage of the OLED and the amplifier.

5 Thermally Activated Delayed Fluorescent (TADF) OLEDs

In this chapter, two types of thermally activated delayed fluorescent (TADF) emitters are investigated, with one being a sky blue emitting pure organic TADF emitter (Tetrazole-xy). Different host materials, mCP and 26DCzppy are incorporated to host the Tetrazole-xy emitter in a regular OLED architecture. The OLEDs with a mixed host system consisting of mCP and 26DCzppy with weight ratio of 95:5 (wt/wt) achieve the best performance with a low onset voltage of $V_{on} = 3.5\,\mathrm{V}$ and 10% external quantum efficiency. The other emitter is a green-emitting copper(I) complex, which is formed from CuI and a MePyrPHOS ligand. Its optimum emitter layer thickness (~20 nm) is determined by fabricating OLED arrays with wedge-shaped emission layer. Using the optimal emission layer thickness, it is incorporated into inverted OLEDs with five solution processed functional layers, including a novel electron injection layer comprising ZrO₂:Y and PEI. The devices finally achieve a low onset voltage of $V_{on} = 3\,\mathrm{V}$ and a high current efficiency of $\eta_c = 29\,\mathrm{cd/A}$ at $100\,\mathrm{cd/m^2}$.

In phosphorescent molecules, the high quantum efficiency is achieved via the employment of rare heavy metals such as iridium or platinum. Yet, the heavy metals contribute to the increased cost and potential environmental contaminations.[86] TADF emitter can harvest both singlet and triplet excitons without using any rare metal. Additionally, despite of highly efficient red and green emitting phosphorescent materials, today the phosphorescent blue emitting OLEDs are below the requirements for stability, color purity and brightness.[97] TADF is widely considered to be the solution to overcome these issues by allowing the transfer from the triplet states to the singlet states and by possessing enhanced stability of the fluorescent emitter without incorporating any expensive heavy metal.

In the very early reports, the TADF mechanism was described inefficient due to the rather large energy difference between the singlet and triplet state (ΔE_{ST}).[81, 129–131] Endo et al. first realized the concept of TADF in OLEDs by incorporating a Sn(IV)–porphyrin complex emitter.[132] Later, they reported on the first OLEDs based on a purely organic TADF emitter.[133] Minimizing the overlap between the molecule's HOMO and LUMO is the key to achieve small ΔE_{ST}. Therefore efficient TADF emitters can be designed
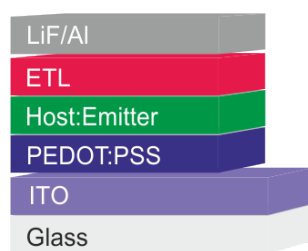
Figure 5.1: Regular OLED architecture used to investigate purely organic TADF emitters, where PEDOT:PSS and the emission layer are deposited from solution, while the electron transport layer and the top electrode LiF/Al are thermally evaporated.

by spatial separation of the HOMOs and the LUMOs of a molecule on the donor and acceptor part respectively.[87]

5.1 TADF OLEDs with Tetrazole-xy

Uoyama et al. reported an efficient green emitting TADF molecule 2,4,5,6-tetra(carbazol-9-yl)-1,3-dicyanobenzene (4CzIPN), where the carbazole (donor) and the acceptor (dicyanobenzene) moieties are spatially separated. Its molecular structure is demonstrated in Table 5.1.[85] First the nitrile group (-CN) of 4CzIPN is transformed into a tetrazole, which is then substituted with an allyl group, yielding an allyl-substituted tetrazole. The allyl group itself can react in further transformations to bind the TADF emitter, for example, to biomolecules or surfaces etc. Other than the allyl group, many functional groups can be introduced, allowing for the follow-up chemistry. To investigate the influence of these transformations on the photophysical properties, as an example, the new molecule 3-(1-allyl-1H-tetrazole-5-yl)-2,4,5,6-tetra(carbazole-9-yl)benzonitrile, henceforth referred to as Tetrazole-xy (Table 5.1) is investigated.

The purely organic TADF emitter (Tetrazole-xy) exhibits a rather high photoluminescence quantum yield (PLQY) of 94%, making it a promising material to be employed as an OLED emitter. In order to choose the appropriate device architecture, its optoelectronic properties are characterized. It possesses a HOMO energy of $E_{HOMO} = -5.9\,\text{eV}$, and the optical bandgap is $E_g = 2.7\,\text{eV}$. Considering the small singlet-triplet energy difference of $\Delta E_{ST} = 0.116\,\text{eV}$ (obtained from density functional theory calculation), the triplet energy level of this emitter is approximately $E_T = 2.6\,\text{eV}$.

Envisioning printing for future device production, the OLEDs are fabricated from solution according to the architecture shown in Figure 5.1. In order to enhance the charge carrier confinement on the emitter molecules and to reduce exciton quenching through triplet-triplet annihilation on neighboring emitter molecules, a host-guest emission layer system must be chosen where the triplet energy E_T of the host is higher than the E_T of the emitter (guest) molecule. If the host exhibits a higher hole mobility
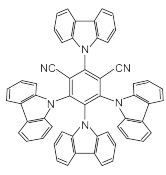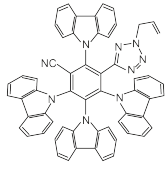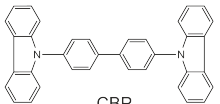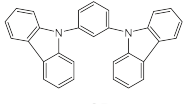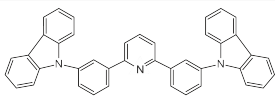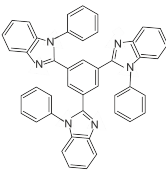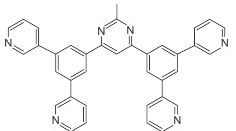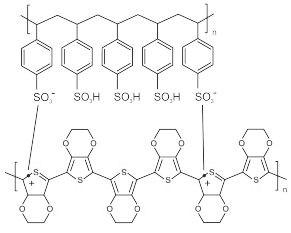
	Molecule	HOMO	LUMO	E_T
Emitter	4CzIPN	-5.9 eV	-3.5 eV	2.4 eV
	Tetrazole-xy	-5.9 eV	-3.2 eV	2.6 eV
Host	CBP	-5.9 eV	-2.5 eV	2.6 eV
	mCP	-6.0 eV	-2.6 eV	3.0 eV
	26DCzppy	-6.1 eV	-2.4 eV	2.7 eV
ETL	TPBi	-6.2 eV	-2.7 eV	2.7 eV
	B3PYMPM	-6.8 eV	-3.2 eV	2.8 eV
HIL	PEDOT:PSS	-5.1 eV	-2.3 eV	—

Table 5.1: Molecular structures, acronyms and energy levels of all organic semiconductors used to investigate Tetrazole-xy OLEDs.

than electron mobility, the emission zone is likely to be close to the cathode. Therefore, a hole blocking layer below the cathode is necessary. Uoyama et al. reported efficient OLEDs with 4,4-bis(carbazol-9-yl)biphenyl (CBP) as a host for 4CzIPN and 2,2,2''-(1,3,5-benzinetriyl)-tris(1-phenyl-1-H-benzimidazole) (TPBi) as the electron transport layer.[85, 134, 135] However, if Tetrazole-xy is incorporated into the same architecture (ITO/PEDOT:PSS/CBP:Tetrazole-xy/TPBi/LiF/Al), the devices show very poor performance with $\eta_c = 5\,\text{cd/A}$ at $100\,\text{cd/m}^2$. This can be attributed to the low triplet energy of CBP ($E_T = 2.6\,\text{eV}$) and the shallow HOMO of TPBi ($E_{HOMO} = -6.2\,\text{eV}$), which lead to severe triplet exciton quenching and inefficient hole blocking.[134] All the energy levels and molecular structures are summarized in Table 5.1.

Consequently, a host with higher triplet energy than the emitter is required. N,N-dicarbazoyl-3,5-benzene (mCP) is a commonly used host which has previously been applied in other blue emitting OLEDs, and it is a well-suited host for Tetrazole-xy due to its higher triplet energy ($E_T = 3.0\,\text{eV}$) than Tetrazole-xy ($E_T = 2.6\,\text{eV}$).[136] Besides a proper host, an alternative ETL with better hole blocking ability is imperative for good device performance. To improve the charge carrier confinement in the emission layer by effectively blocking holes, the electron transport material bis-4,6-(3,5-di-3-pyridylphenyl)-2-methylpyrimidine (B3PYMPM) with a deep HOMO ($E_{HOMO} = -6.8\,\text{eV}$) and a high triplet energy ($E_T = 2.8\,\text{eV}$) is investigated.[137]

The emission layer comprises the mCP host and the Tetrazole-xy emitter with a weight ratio of 100:15 (wt/wt). The corresponding OLED characteristics are illustrated in Figure 5.2. The luminance-voltage curve in Figure 5.2b reveals an onset voltage of $V_{on} = 3\,\text{V}$ (at $1\,\text{cd/m}^2$) for the OLEDs with mCP host. At $100\,\text{cd/m}^2$, the OLEDs achieve a current efficiency of $\eta_c = 14\,\text{cd/A}$ (Figure 5.2c) which corresponds to an external quantum efficiency EQE = 6.7% (Figure 5.2d).

Due to the superior hole transport in mCP, the triplet excitons are likely to accumulate at the interface of the mCP:Tetrazole-xy emission layer and the B3PYMPM. This results in a narrow recombination zone and, at high current densities, leads to triplet-triplet annihilation and strong efficiency roll-off.[138] Hence, to improve the efficiency of the OLED, the alternative ambipolar host 2,6-bis(3-(carbazol-9-yl)phenyl)pyridine (26DCzppy) is incorporated to yield a more balanced charge carrier transport and broaden the recombination zone.[107, 139] The weight ratio of the host and the emitter is kept at 100:15 (wt/wt). For direct comparison, the characteristics of the OLEDs incorporating this 26Dczppy host are plotted in Figure 5.2 together with the curves of the devices with the neat mCP host. At $100\,\text{cd/m}^2$, the devices produce a current efficiency of $\eta_c = 17\,\text{cd/A}$ and an EQE = 7.3% which is a significant improvement compared to the OLEDs with mCP host. Notably, in OLEDs with neat 26DCzppy hosts, towards higher luminance, a reduced efficiency roll-off is found which can be attributed to the more
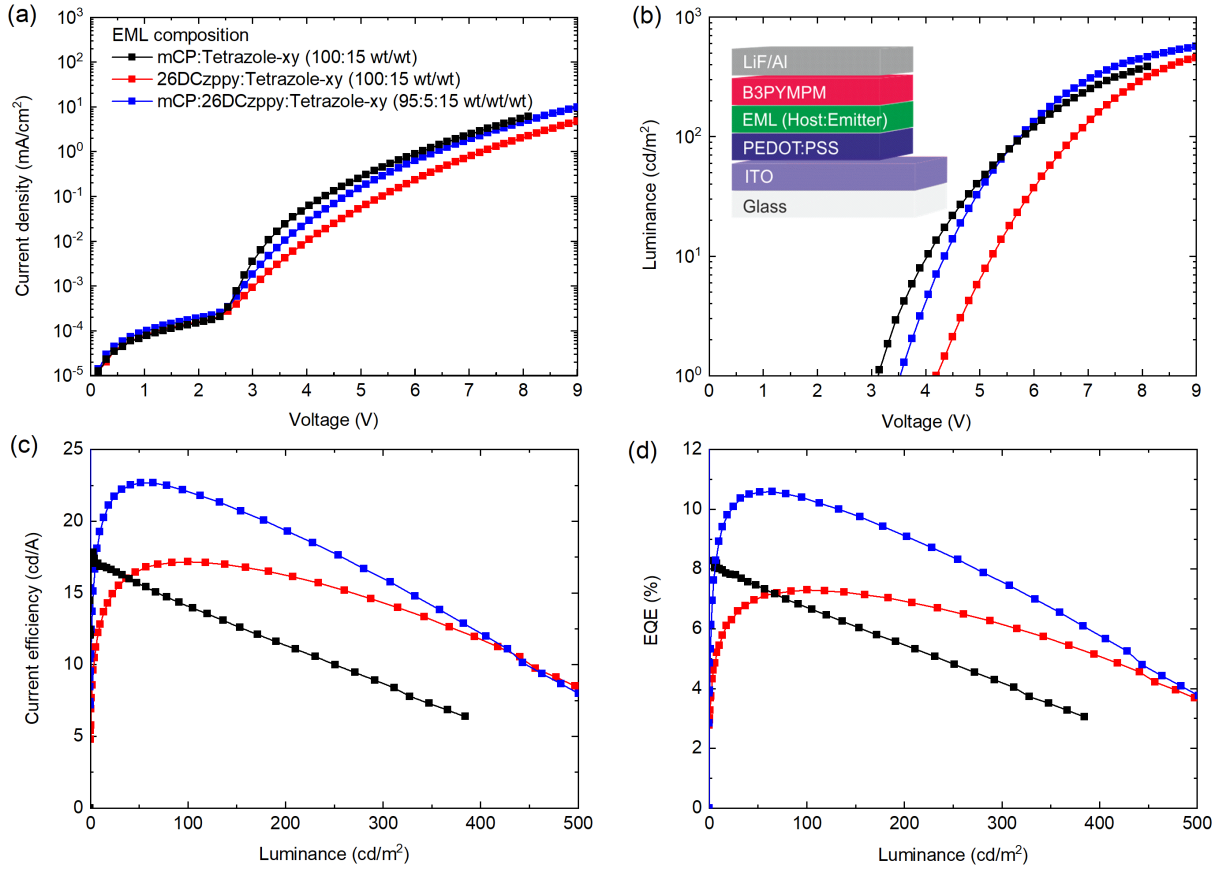
Figure 5.2: (a) J-V characteristics of the OLEDs with emission layers comprising different host:Tetrazole-xy combinations. (b) Luminance-voltage (L-V) curves. Inset: The OLED architecture. (c) Current efficiency versus luminance. (d) External quantum efficiency versus luminance.

balanced charge carrier transport in 26DCzppy and hence a recombination zone away from any layer interfaces.[140] However, the triplet energy of 26DCzppy ($E_T = 2.7\,\mathrm{eV}$) is similar to that of Tetrazole-xy ($E_T = 2.6\,\mathrm{eV}$) which may lead to a reduced exciton confinement on the Tetrazole-xy emitter.[141]

Therefore, in a third approach, a blend of mCP and 26DCzppy is employed to host Tetrazole-xy in the same OLED architecture. In all OLEDs, the weight ratio between the host and the emitter is kept constant (100:15 wt/wt), while the fraction between two hosts is varied. In Figure 5.3, the external quantum efficiencies of the OLEDs with different compositions of mCP and 26DCzppy are plotted. The same EQE trend is observed at both luminances of $100\,\mathrm{cd/m^2}$ and $300\,\mathrm{cd/m^2}$. The EQE continuously increases with rising mCP quantity until the maximum efficiency is reached, that is, a mCP:26DCzppy:Tetrazole-xy weight ratio of 95:5:15 (wt/wt/wt). For better comparison, properties using an optimized mixed host are also depicted in Figure 5.2. Notably, by combining the properties of both host materials, the OLEDs show superior current efficiencies and EQEs to the devices comprising a neat host. At $100\,\mathrm{cd/m^2}$, current efficiencies of up to $\eta_c = 22\,\mathrm{cd/A}$ and corresponding EQE = 10.4% are accomplished.
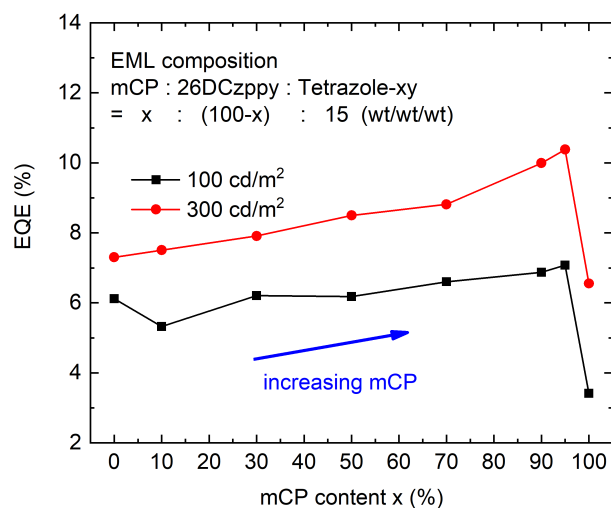
Figure 5.3: External quantum efficiency of the OLEDs incorporating mCP:26DCzppy blend as host for Tetrazole-xy. The weight ratio between the host and the emitter is fixed to be 100:15 (wt/wt). By varying the ratio between mCP and 26DCzppy, the EQE changes. The optimum ratio of mCP and 26DCzppy is found at 95:5 (wt/wt).

The normalized emission spectra of the OLEDs at 8.1 V incorporating pure mCP, pure 26DCzppy and the blend of mCP and 26DCzppy as host for Tetrazole-xy are depicted in Figure 5.4a. Only emission from the emitter Tetrazole-xy is detected, evidencing the effective hole blocking and exciton confinement effect of B3PYMPM. The almost identical spectra imply that the choice of host has no influence on the emission spectrum. The CIE1931 color coordinates of (x,y) = (0.19, 0.33) (at V = 8.1 V) are calculated from the electroluminescence spectrum, which confirms that Tetrazole-xy is a sky blue emitter as depicted in Figure 5.4b.

Experimental: The HOMO of 4CzIPN and Tetrazole-xy are measured by PESA. The absorbance onset characterized by UV-Vis-NIR spectrometry is considered to represent the optical bandgap. All OLEDs are fabricated on ITO coated glass substrates using the standard layout. PEDOT:PSS (Clevios P VPAI 4083, Heraeus Deutschland GmbH & Co. KG) and the emission layer are spincoated sequentially according to the recipe summarized in Table 5.2. The hosts and emitters are separately dissolved in tetrahydrofuran (THF) before they are mixed with a specific weight ratio to achieve a final concentration of 2 mg/mL. Then an electron transport layer (60 nm) as well as an LiF (1 nm)/Al (200 nm) cathode are deposited via thermal evaporation. The optoelectronic measurements are conducted in the integrating sphere setup.
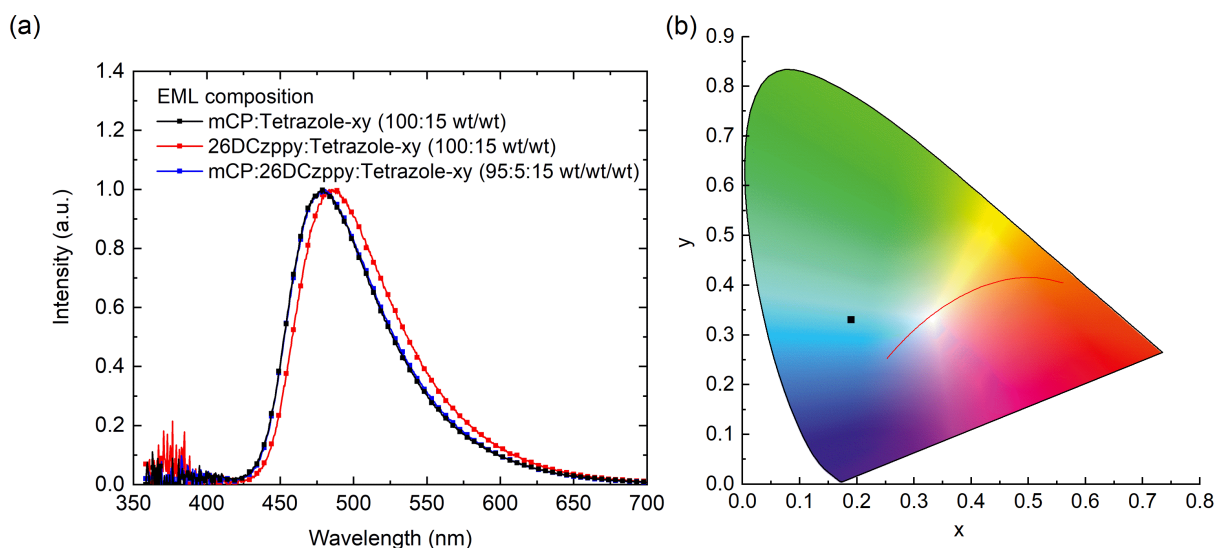
Figure 5.4: (a) The normalized electroluminescence spectra of the OLEDs at 8.1 V employing neat mCP, neat 26DCzppy or a blend of mCP and 26DCzppy as hosts for Tetrazole-xy emitter. The emission peak is around 490 nm. (b) The corresponding CIE1931 coordinate is (x,y) = (0.19, 0.33), and the location of the black point indicates the color of the OLEDs at 8.1 V. The red curve indicates Planckian locus.

Layer	Concentration	Solvent	Spincoating	Annealing	Thickness
PEDOT:PSS	1:3 (v/v)	ethanol	4000 rpm, 30 s	100 °C, 10 min	25 nm
EML	2 mg/mL	THF	1000 rpm, 30 s	60 °C, 10 min	30 nm

Table 5.2: Spincoating parameters for the HIL (PEDOT:PSS) and the TADF organic emission layer (EML).

5.2 TADF OLEDs with Copper(I) Complex

Delayed fluorescence has been observed in various organic copper(I) complexes. Since Deaton et al. first incorporated an organic copper(I) complex based emission layer into OLEDs which exhibited an impressive efficiency of EQE = 16.1%, extensive investigations have been carried out.[142–144] In such copper(I) complexes, the central copper(I) atom introduces a moderate spin-orbit coupling. Consequently, ΔE_{ST} is small and fast intersystem crossing to the triplet state and back is observed. At room temperature, the repopulation of the singlet excited states gives rise to thermally activated delayed fluorescence.[131].

Conventionally, Cu(I) emitters are synthesized, isolated and processed. Here a simplified process of co-depositing a Cu(I) precursor and a ligand is used. The feasibility of this co-deposition approach was demonstrated with an extended X-ray absorption spectroscopy study.[146] The ratio of the copper salt and the organic ligand was previously optimized to 2:3 (v/v). The homoleptic Cu(I) complex showing delayed fluorescence is incorporated into solution processed OLEDs. This Cu(I) complex is
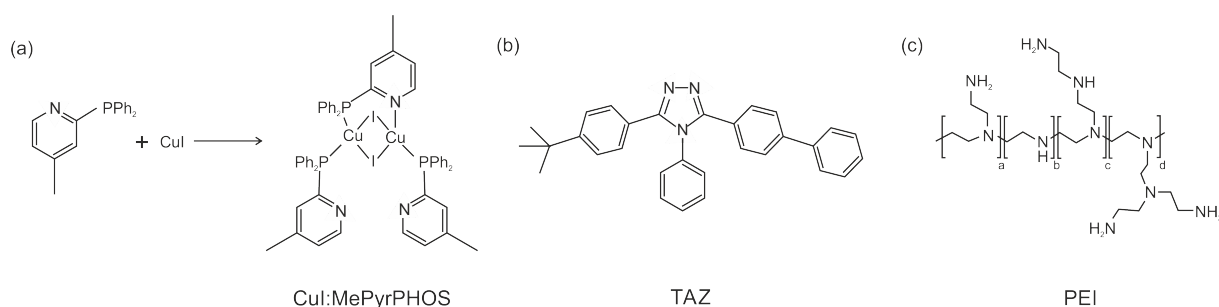
Figure 5.5: (a) The copper(I) complex emitter is formed by mixing two molecules of CuI and three molecules of MePyrPHOS. The molecular structure of (b) TAZ and (c) PEI.[145]
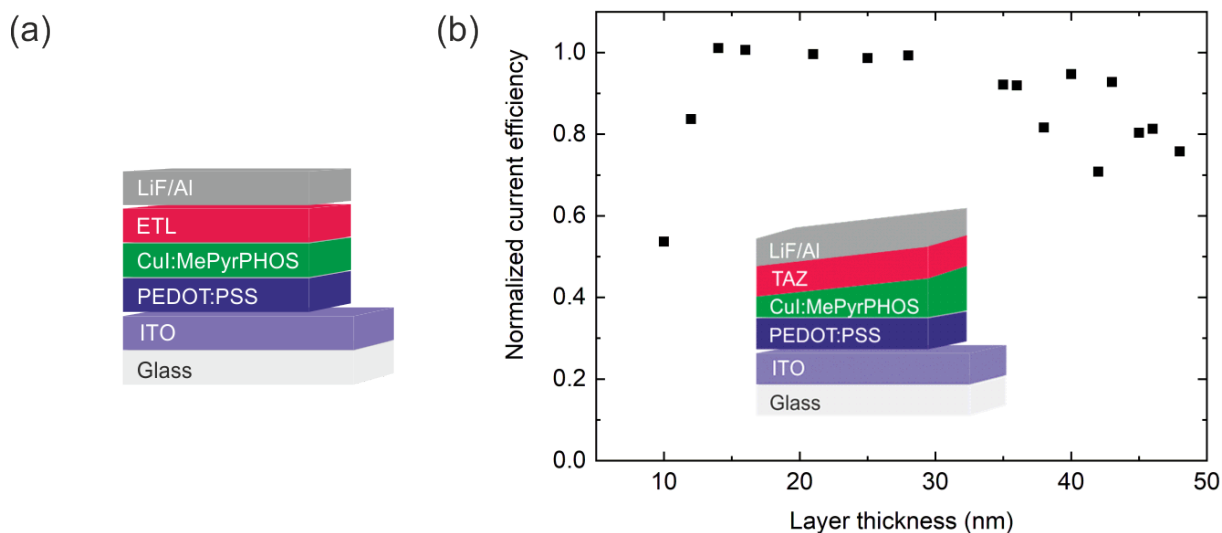
Figure 5.6: (a) Regular OLED architecture incorporating the TADF emitter complex CuI:MePyrPHOS. (b) Normalized current efficiency of OLEDs with architecture indicated in the inset. The OLED arrays are fabricated with various emission layer thicknesses changing from 10 nm to 50 nm, while the thicknesses of the other layers are kept constant. The highest current efficacy is achieved with an emission layer thickness of around 20 nm.

formed from two molecules of copper iodide (CuI) and three molecules of organic ligands, 4-methyl-2-(diphenylphosphino)-pyridine (MePyrPHOS, cynora GmbH).[147, 148] As depicted in Figure 5.5a, the molecule is based on a butterfly shaped Cu_2I_2 core bridged by a N,P-ligand, with two ligands on the periphery coordinated to the Cu(I)-ions. The HOMO of the compound is mainly localized on the Cu_2I_2 core, while the LUMO is largely located on the bridging N,P-ligand.[147] Excellent solubility of the CuI salt and the MePyrPHOS ligand in acetonitrile facilitates solution deposition.

Initially, the emitter is investigated in the regular OLED architecture that is depicted in Figure 5.6a. The optimized emission layer thickness is determined by fabricating wedge-shaped OLEDs (Chapter 4.2) with emission layer thickness varying from 10 nm to 50 nm along the substrate. To facilitate electron transport, an electron transport layer is thermally evaporated. Since triplet excitons are involved in the electroluminescence mechanism of the copper(I) complex, the electron transport layer should have a

higher triplet energy level than the emitter to confine triplet excitons in the emitter. The common electron transport material, 3-phenyl-4-(1'-naphthyl)-5-phenyl-1,2,4-triazole (TAZ) ($E_{HOMO} = -6.6$ eV, $E_{LUMO} = -2.6$ eV, $E_T = 2.8$ eV) fulfills this requirement.[149, 150] In addition, owing to its deeper HOMO than the emitter, the holes are expected be blocked effectively. All OLEDs are characterized by using the integrating sphere setup. The normalized current efficiencies of all OLED pixels with different emission layer thicknesses are plotted in Figure 5.6b. The maximum current efficiency is obtained with an emission layer thickness of 15-27 nm.

After the determination of the optimal emission layer thickness, the corresponding spincoating parameters for the standard OLED layout are determined for further device improvement, and the resulting emission layer thickness is 22 nm. The characteristics are illustrated in Figure 5.7. Due to the enhanced exciton confinement in the emission layers, the current efficiency of the OLEDs achieve $\eta_c = 20$ cd/A at 100 cd/m^2. However, the onset voltage of $V_{on} = 5.2$ V is rather high. It is attributed to the low electron mobility of TAZ (1.57×10^{-6} cm^2/Vs), which leads to a low current density and hence a high onset voltage.[151] Consequently, the electron transport material TPBi with higher electron mobility (6.52×10^{-5} cm^2/Vs) is used for further investigations.

As discussed in Chapter 5.1, TPBi is a common electron transport material with a deep HOMO ($E_{HOMO} = -6.2$ eV) and a high triplet energy ($E_T = 2.7$ eV).[135] Due to all these beneficial properties, TPBi is used as ETL in the OLEDs. As visible in Figure 5.7, the OLEDs exhibit a lower onset voltage of $V_{on} = 4.5$ V compared to the devices with TAZ because of the higher electron mobility of TPBi. At 100 cd/m^2, the current efficiency is only about $\eta_c = 11$ cd/A due to its lower exciton and hole confinement ability than TAZ. Yet, the power efficiency difference between devices with TPBi and TAZ is small. At a luminance higher than 400 cd/m^2, the OLEDs with TPBi are even better than the performance of OLEDs comprising TAZ.

In order to eventually realize all-solution processed OLEDs, all functional layers including the EIL and the ETL need to be soluble in suitable solvents. Furthermore, the solutions for the subsequent layers must not dissolve the underlying layer, which in turn requires a set of orthogonal solvents. ZnO is a common solution processed EIL in organic devices. In this chapter, an alternative EIL, yttrium doped zirconium oxide (ZrO$_2$:Y), is studied due to its resistance against acidic environment, thus enabling both inverted and regular tandem architectures. The details of tandem architecture will be discussed later in Chapter 6. The electron injection ability of ZrO$_2$:Y nanoparticles (2.5 wt.% in isopropanol, Avantama AG) is analyzed by KPFM. A work function of $\Phi = 4.1$ eV is found. Therefore ZrO$_2$:Y itself as an EIL might cause a large electron injection barrier for most emission layers. It was reported that by applying polyethylenimine (PEI) (molecular structure in Figure 5.5c) on top of ZnO, the work function of the EIL can be further lowered.[22, 55] Likewise,
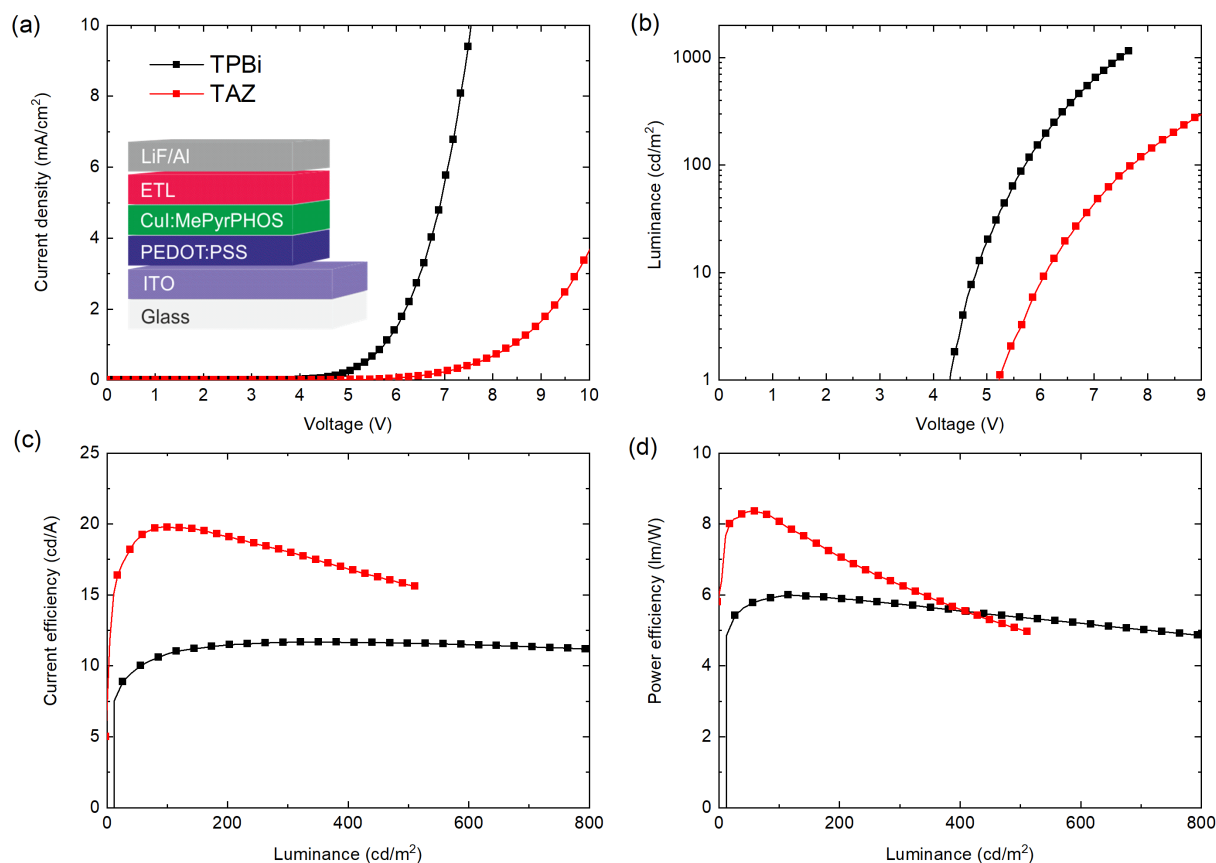
Figure 5.7: Optoelectronic characteristics of regular OLEDs comprising CuI:MePyrPHOS complex as emitter, where either TPBi or TAZ is evaporated as ETL on top of emitter: (a) J-V curves, (b) L-V curves, (c) current efficiency and (d) power efficiency.

the work function of ZrO_2:Y/PEI ($\Phi = 3.5\,eV$) is analyzed with KPFM, which is similar to ZnO/PEI. As for the ETL, TPBi instead of TAZ is chosen, since TPBi has a higher electron mobility and it can be dissolved in ethanol, which opens up new possibilities of incorporating other organic emitters.

After carefully choosing the proper EIL and ETL, regular TADF OLEDs according to the architecture in Figure 5.8a (inset) are fabricated. In this OLED architecture, all layers are deposited from solution, except the electrodes. Although PEDOT:PSS can be coated from solution, its relatively low work function ($\Phi = 5.1\,eV$) is likely to be one reason for the high onset voltage of the Cu(I) OLEDs (Figure 5.7b). To further reduce the hole injection barrier, a transition metal oxide WO_3 with a high work function of $\Phi = 5.9\,eV$ is employed instead of PEDOT:PSS. The layer is obtained from WO_3 nanoparticle dispersions (0.55 wt.% in water, P-10, Avantama AG). Subsequently, TPBi is spincoated on the emitter. As shown in Figure 5.8b, the devices exhibit a rather low onset voltage of $V_{on} = 3\,V$, indicating efficient charge carrier injection. Consequently, the current efficiency can reach above $\eta_c = 25\,cd/A$. Thus efficient TADF OLEDs with a copper(I) complex emission layer are realized, where five functional layers are
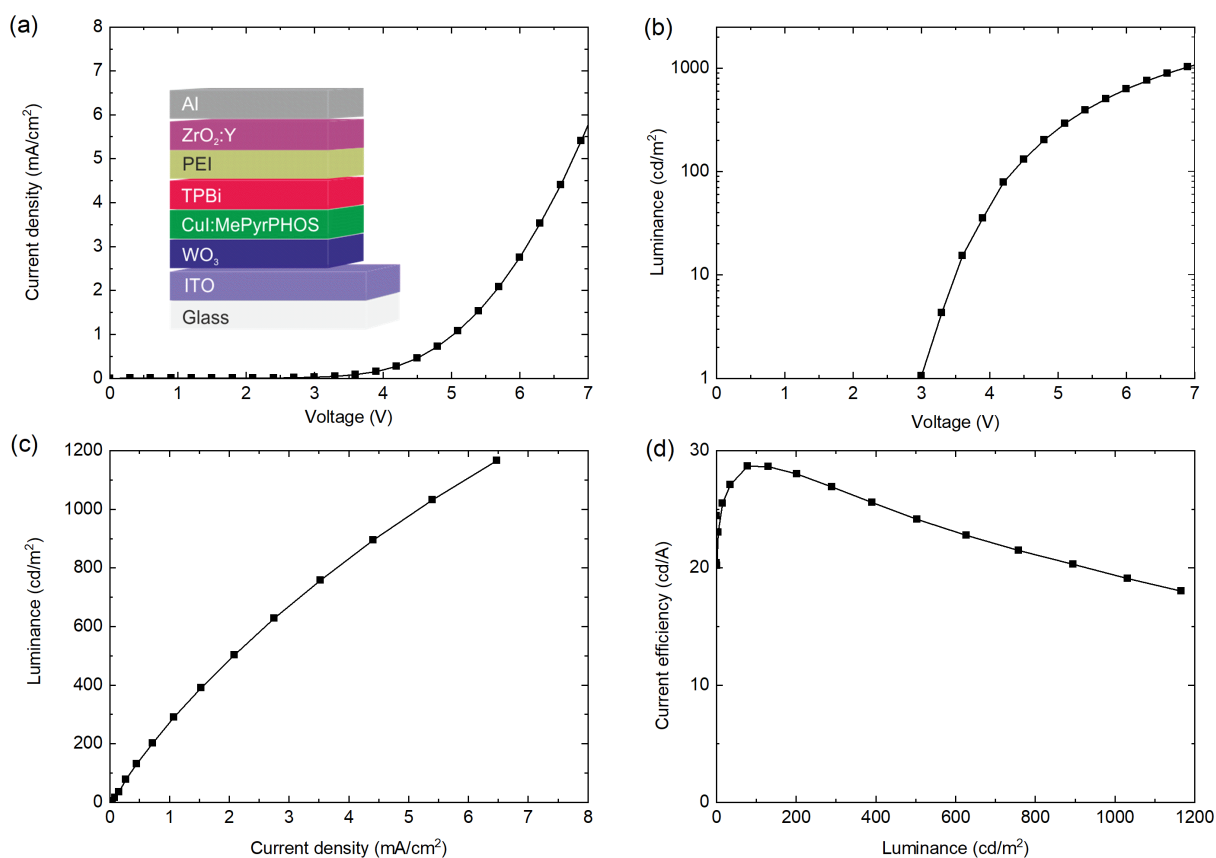
Figure 5.8: Optoelectronic characteristics of OLEDs with all functional layers deposited from solutions except the two electrodes. The emitter is a TADF copper(I) complex formed from CuI and MePyrPHOS: (a) J-V curves, (b) L-V curves, (c) L-J curves, (d) current efficiency versus luminance.

deposited from solutions. The outstanding performance implies the integrity of all layers during sequential deposition of the layers from solution. This novel ZrO_2:Y/PEI electron injection layer hence allows for more advanced OLED architectures, such as tandem OLEDs.

Experimental: For the fabrication of OLED arrays, PEDOT:PSS is deposited on ITO by H-dipping, where the rod is moved 400 μm above the substrate. The parameters are given in Table 5.3. The rod moves with an initial speed of 13 mm/s and it accelerates during deposition until the final speed of 15 mm/s. To obtain a wedge-shaped emission layer, CuI and MePyrPHOS are separately dissolved in acetonitrile with concentrations of 9.5 mg/mL and 13.9 mg/mL before they are mixed with volume ratio of 2:3 (v/v). The H-dipping follows the recipe in Table 5.3. The resulting emission layer thickness varies from 10 nm to 50 nm. 50 nm TAZ and the cathode made up of LiF (1 nm)/Al (200 nm) are sequentially evaporated. The OLED arrays are afterwards characterized in the integrating sphere setup.

Layer	Concentration	Solvent	Start Speed	Final Speed	Thickness
PEDOT:PSS	1:3 (v/v)	ethanol	13 mm/s	15 mm/s	25 nm
CuI:MePyrPHOS	12.1 mg/mL	acetonitrile	99 mm/s	2 mm/s	10-50 nm

Table 5.3: H-dipping parameters for the HIL (PEDOT:PSS) and the wedge-shaped CuI:MePyrPHOS emitter.

Layer	Concentration	Solvent	Spincoating	Annealing
WO_3	0.55 wt.%	isopropanol	4000 rpm, 45 s	50 °C, 10 min
CuI:MePyrPHOS	4.9 mg/mL	acetonitrile	1000 rpm, 50 s	70 °C, 5 min
TPBi	3.0 mg/mL	ethanol	1000 rpm, 20 s	-
ZrO_2:Y	0.55 wt.%	water	4000 rpm, 45 s	50 °C, 10 min
PEI	3.7 mg/mL	water	4000 rpm, 20 s	100 °C, 10 min

Table 5.4: All the spincoating parameters for the solution processed CuI:MePyrPHOS TADF OLEDs.

In the standard OLED architecture, PEDOT:PSS (Clevios P VPAI 4083) is spincoated with the same parameter as in Table 5.2. CuI and MePyrPHOS are separately dissolved in acetonitrile with concentrations of 3.8 mg/mL and 5.6 mg/mL before they are mixed with volume ratio of 2:3 (v/v) to reach a total concentration of 4.9 mg/mL. The spincoating recipe can be found in Table 5.4. After evaporating 50 nm of TAZ or TPBi, LiF (1 nm)/Al (200 nm) is sequentially evaporated. The optoelectronic measurements are conducted in the OCS setup.

All solution processed layers are spincoated following the recipe provided in Table 5.4. The work function measurements are conducted by using KPFM. In the inverted architecture, 10 nm MoO_3 and 100 nm silver are evaporated for hole injection. In the regular OLEDs, 200 nm aluminum is evaporated as cathode. All OLEDs use standard layout and are measured with the OCS setup.

6 Universal Charge Generation Layers for Tandem OLEDs

In this chapter, a universal charge carrier generation (CGL) layer for highly efficient solution processed tandem OLEDs is reported. This CGL can be employed for fluorescent polymers, phosphorescent molecules and TADF emitters. Because the CGL is robust against the most common solvents, it can be employed in both regular and inverted device architectures. By introducing charge carrier blocking layers, altogether eleven functional layers are sequentially processed from solutions. The tandem OLEDs with the phosphorescent emitter SM-green-A show a high current efficiency of up to $\eta_c = 184\,\mathrm{cd/A}$ and a remarkable lifetime with $LT_{80} = 1700\,\mathrm{h}$, outperforming the single reference OLEDs.

Thermal evaporation in vacuum is commonly used for the industrial fabrication of state-of-the-art OLEDs. Vacuum processing enables the stacking of an arbitrary number of functional layers, thus it can produce devices with high performance. Various architectures of tandem OLEDs fabricated by vacuum processing have been reported.[5, 152] Yet, maintaining the layer integrity of previously applied layers during deposition of subsequent layers from solutions still remains challenging, especially when the device architecture incorporates so many functional layers as in tandem OLEDs. The integration of cross-linkable materials is one concept to address solvent limitations, but they often require harsh processing conditions e.g. high annealing temperature and UV irradiation, which may also affect the integrity of the layer stack.[153–157] This is why orthogonal solvents are utilized in the solution processed tandem OLEDs and other advanced architectures, which in return limits the material choices. [139, 158]

CGL is critical for the overall performance of the tandem device, hence it requires a careful design. Upon applying a forward bias to the tandem OLEDs, pairs of electrons and holes are generated in CGL and injected into the sub-OLEDs. A very common CGL comprises one electron and one hole injection layer. In spite of various options for efficient hole injection layers, such as PEDOT:PSS, WO_3, MoO_3 or V_2O_5, the material choice for electron injection layers has rather been limited to ZnO.[38, 39, 159, 160]

A four-layer CGL comprising WO_3/PEDOT:PSS/ZnO/PEI was reported by Höfle et al. The WO_3 layer facilitates hole injection into the bottom OLED, while the ZnO/PEI

Layer	Concentration	Solvent	Spincoating	Annealing
		Inverted architecture		
ZrO$_2$:Y	0.55 wt.%	isopropanol	4000 rpm, 45 s	50 °C, 10 min, vacuum
PEI	3.7 mg/mL	isopropanol	4000 rpm, 20 s	100 °C, 10 min, N$_2$
SM-Green A	22 mg/mL	toluene	1000 rpm, 45 s	70 °C, 5 min, N$_2$
Super Yellow	4 mg/mL	toluene	1000 rpm, 60 s	70 °C, 5 min, N$_2$
CuI:MePyrPHOS	4.9 mg/mL	acetonitrile	1000 rpm, 50 s	70 °C, 5 min, N$_2$
mCP	3.0 mg/mL	ethanol	1000 rpm, 20 s	-
WO$_3$	0.55 wt.%	water	4000 rpm, 45 s	50 °C, 10 min, vacuum
PEDOT:PSS	1:3 (v/v)	water	4000 rpm, 60 s	-
		Regular architecture		
WO$_3$	0.55 wt.%	isopropanol	4000 rpm, 45 s	50 °C, 10 min, vacuum
TPBi	3.0 mg/mL	ethanol	1000 rpm, 20 s	-
PEI	3.7 mg/mL	water	4000 rpm, 20 s	100 °C, 10 min, N$_2$
ZrO$_2$:Y	0.55 wt.%	water	4000 rpm, 45 s	50 °C, 10 min, vacuum

Table 6.1: Summary of all process parameters used for layer deposition in this chapter.

bilayer injects electrons into the top OLED.[158] To hinder the solvent diffusion, a solvent impenetrable PEDOT:PSS layer is incorporated into the CGLs.[161] Yet the combination of ZnO and PEDOT:PSS is crucial for the device lifetime, and it hinders the fabrication of tandem OLEDs with regular architecture since the acidic PEDOT:PSS would dissolve the underlying ZnO layer. Therefore although this combination is incorporated in the previous solution processed tandem OLEDs, it is limited to inverted device architectures, where ZnO is deposited atop a PEDOT:PSS layer.[139, 158]

In the few reports about tandem OLEDs with regular architecture, the emitters are less soluble polymers because of the absent of PEDOT:PSS solvent barrier.[162, 163] In addition, due to the solvent limitations, so far all solution processed tandem OLEDs lack blocking layers. Yet as discussed in Chapter 3.4, blocking layers are essential for high-performing devices as they enhance proper charge carrier and exciton confinement inside the emission layers.

In the previous chapter, an alternative to ZnO is introduced for TADF OLEDs. The ZrO$_2$:Y does not dissolve in weak acidic media, enabling both inverted and regular tandem architectures. It also has a wide bandgap, thus parasitic re-absorption of light is prevented.

6.1 Inverted Phosphorescent Tandem OLEDs

Inverted OLEDs have recently drawn attention as they are easy to integrate with common n-type transistors, which are based on low-cost and highly-uniform transparent amorphous oxide semiconductors and amorphous silicon.[164] To examine the function of ZrO$_2$:Y in
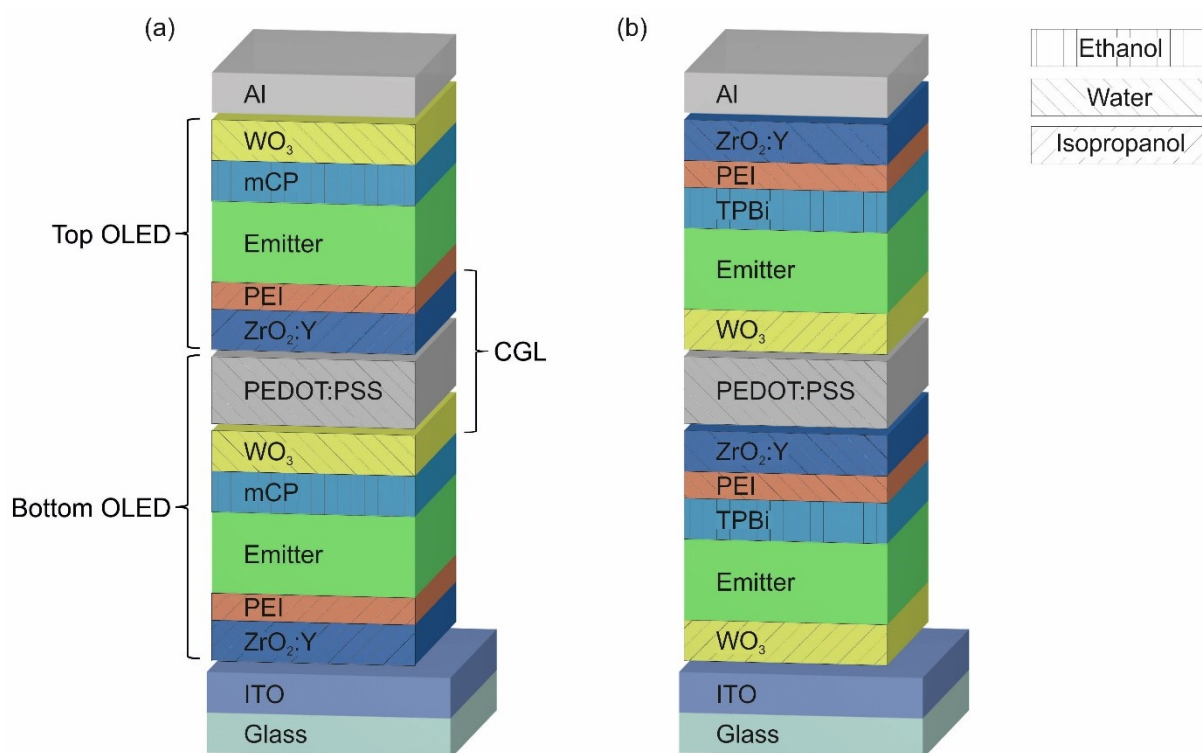
Figure 6.1: Device architectures of tandem OLEDs with (a) inverted and (b) regular device architecture. The charge generation layer (CGL) comprises WO_3/PEDOT:PSS/ZrO_2:Y/PEI, and it can be employed universally in inverted and regular device architectures. In addition, it provides a robust solvent barrier for most common solvents. Phosphorescent SM-Green-A, commercially available fluorescent Super Yellow or CuI:MePyrPHOS TADF is used to build the emission layers. The hatchures indicate solvents used for CGL layer.

the CGL, it is comprised in CGL WO_3/PEDOT:PSS/ZrO_2:Y/PEI for the tandem OLED architecture as depicted in Figure 6.1a. A phosphorescent small molecule SM-green-A is incorporated as emission layer. All processing parameters are summarized in Table 6.1.

In order to confine the charges inside the emission layer, an additional electron blocking and exciton confinement layer formed from mCP is introduced atop the emission layer. In Chapter 5, mCP is chosen as a host, and due to its shallow LUMO ($E_{LUMO} = -2.6\,eV$) and high triplet energy $E_T = 3\,eV$, mCP can also efficiently hinder the triplet excitons from reaching the anode, therefore impeding non-radiative recombination.[76] In order to achieve solvent impenetrable CGL, PEDOT:PSS (Clevios HTL Solar, Heraeus) mixed with sodium polystyrene sulfonate (SPS, 16:1 v/v) is integrated into CGL. Additionally it is admixed with the surfactant Zonyl (1 vol%) to improve its wetting properties. In total, eleven layers are sequentially spincoated in the tandem architecture.

For reference, the corresponding top and bottom OLEDs are fabricated as single devices with ITO and Al electrodes. The PEDOT:PSS interlayer is incorporated into the bottom reference OLED. Notably, all functional layers other than the emission layers are deposited from non-hazardous solvents, including ethanol, water and isopropanol.
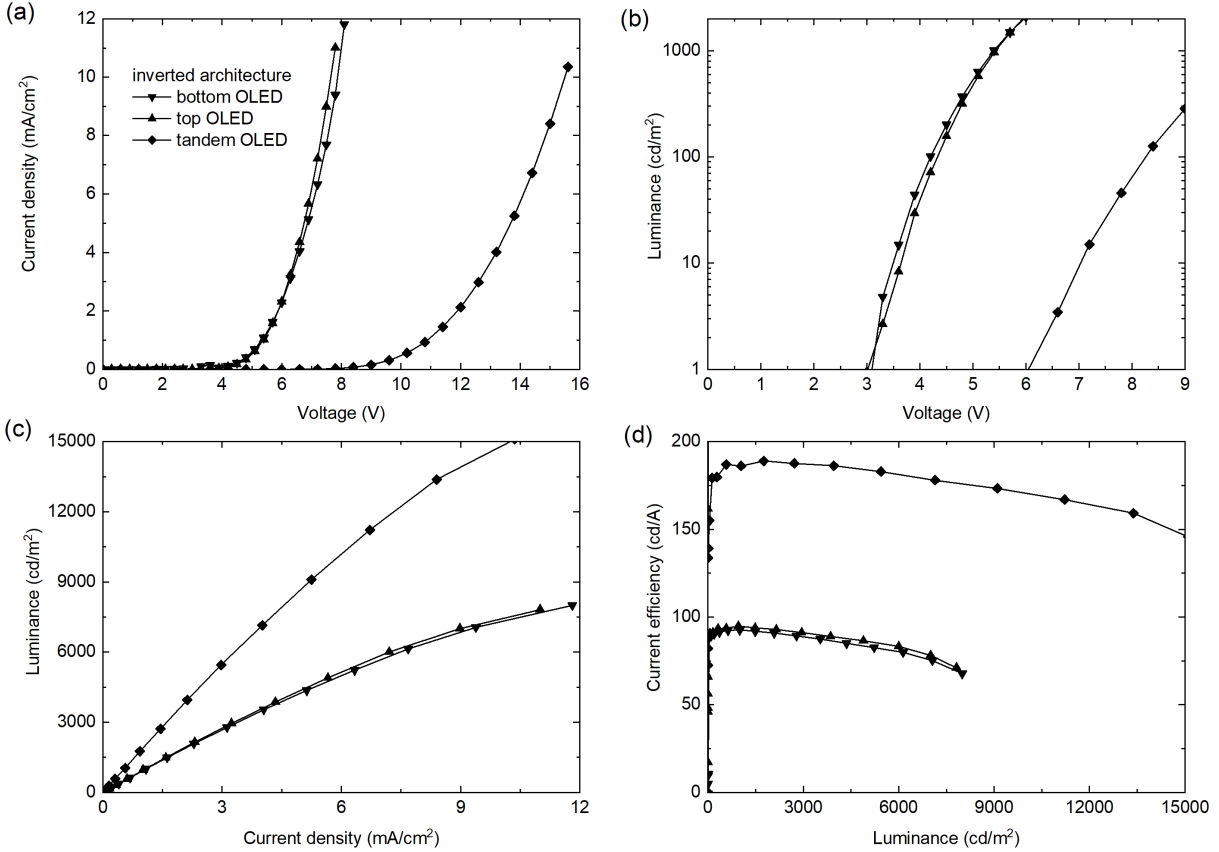
Figure 6.2: Optoelectronic properties of the tandem OLEDs (diamond) with the inverted architecture, which comprises the green emitting phosphorescent material SM-green-A in comparison to its corresponding bottom (down triangle) and top (up triangle) reference OLEDs: (a) J-V curves, (b) L-V curves, (c) L-J curves, (d) current efficiency versus luminance.

The emission layers are deposited from comparably unproblematic solvents, such as toluene or acetonitrile, which reveals its industrial fabrication potential. In Figure 6.2, the optoelectronic properties of the tandem OLEDs together with the single OLEDs comprising SM-green-A emission layers are summarized. The two sub-OLEDs show almost identical optoelectronic characteristics. In a properly working tandem OLED, its sub-OLED voltages adds up at the operating current. Figure 6.2a shows an almost perfect sum of driving voltages. For instance, at a certain current density of $J = 0.1 \, \mathrm{mA/cm^2}$, the driving voltage of the tandem OLED $V_{tandem} = 8.7 \, \mathrm{V}$ is approximately the addition of both reference device voltages $V_{bottom} = 4.4 \, \mathrm{V}$ and $V_{top} = 4.2 \, \mathrm{V}$. As Figure 6.2b demonstrates, this holds also true for the onset voltage at a luminance of $1 \, \mathrm{cd/m^2}$. The onset voltage of the tandem device is $V_{on,tandem} = 6.2 \, \mathrm{V}$, which is the onset voltage sum of the bottom OLED ($V_{on,bottom} = 3.1 \, \mathrm{V}$) and the top OLED ($V_{on,top} = 3.1 \, \mathrm{V}$). In particular, Figure 6.2c confirms that at a given current density, an addition of sub-OLED luminances in the tandem OLED is recorded. For instance, at the same current density of $J = 2.5 \, \mathrm{mA/cm^2}$, the luminance of single OLEDs is around $2177 \, \mathrm{cd/m^2}$, while the
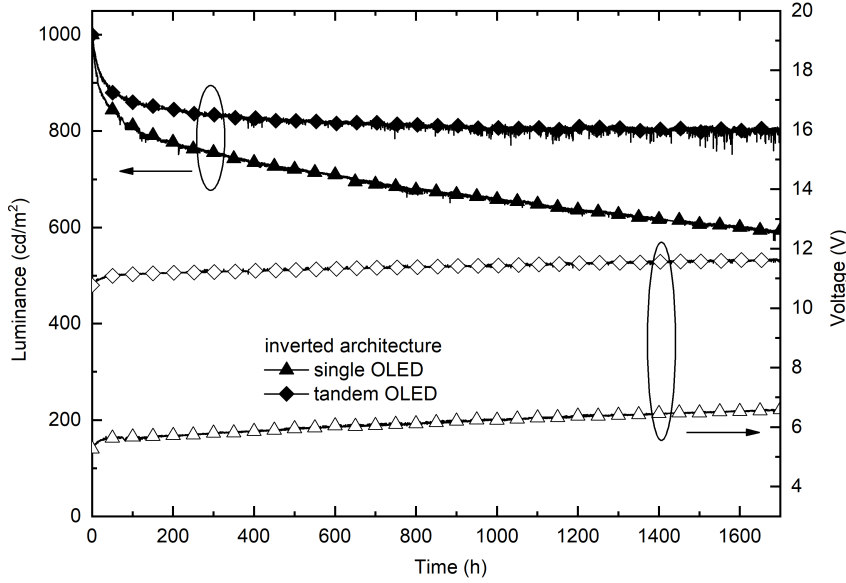
Figure 6.3: The device lifetime of OLEDs comprising SM-green-A as emission layer. The luminance (left axis) and the driving voltage (right axis) are plotted versus time. The measurements are conducted on inverted tandem (diamond) and the corresponding single (top, up-triangle) OLEDs. The constant current is set to achieve an initial luminance of $1000\,cd/m^2$. After 1700 hours (71 days) of continuous measurements, the tandem OLEDs still achieve 80% of the initial luminance, while the luminance of the single reference is decayed to 58%.

tandem device approximately doubles the luminance by achieving $4670\,cd/m^2$. Likewise, current efficiency curves in Figure 6.2d follow the same trend. At a luminance of around $500\,cd/m^2$, both single OLEDs show an excellent current efficiency of around $\eta_{c,bottom} = \eta_{c,top} = 92\,cd/A$. At $1000\,cd/m^2$, the tandem OLED achieves its maximum current efficiency $\eta_{c,tandem} = 184\,cd/A$. Notably, a reduced efficiency roll-off in the tandem OLED is observed, which can be attributed to the reduced current density at a given luminance. In the tandem device, the exciton densities are lower, hence exciton annihilation probabilities (triplet-triplet annihilation and triplet-polaron quenching) are reduced.[107, 165]

In addition, the device lifetime in the tandem device is enhanced by the lower current density and reduced non-radiative recombination. To compare the device lifetime of the tandem and single OLEDs, the devices are set to an identical initial luminance of $L_0 = 1000\,cd/m^2$. The operating current density of the tandem OLED is $J_{tandem} = 0.54\,mA/cm^2$ and the corresponding voltage is $V_{tandem} = 10.6\,V$. To yield the same initial luminance, the current density of the single top OLED is twice as high ($J_{top} = 1.1\,mA/cm^2$) and the operating voltage is $V_{top} = 5.6\,V$. During the lifetime measurements, the OLEDs are driven by a constant current and the emission intensities are monitored every 1 min.

Figure 6.3 depicts the device luminances (left axis) and driving voltages (right axis) at constant current densities versus time. After 1700 hours (i.e. 71 days) measurements, 80% of the initial luminance (LT_{80}) are still detected in tandem OLEDs, and the operating

voltage slowly increases to 11.6 V. Meanwhile, only 58% of their initial luminance are observed in single devices, and the voltage increases to 6.6 V. These curves clearly show the superior performance of the all-solution processed tandem OLED over their single OLED references.

6.2 Regular Phosphorescent Tandem OLEDs

As discussed above, the benefit of ZrO_2:Y over ZnO is its robustness towards acidic solvents. Thus it enables the fabrication of regular tandem OLED architectures with non-polymeric emitters. Accordingly all-solution processed tandem OLEDs with regular architecture are fabricated with a CGL comprising WO_3/PEDOT:PSS/ZrO_2:Y/PEI. As illustrated in Figure 6.1, the functional layers are similar but in different order. The solvents used for the same material can be different due to its position change in regular and inverted architectures. All process parameters are also summarized in Table 6.1. The single OLEDs share the same architecture reported in Chapter 5.2. On top of the emitter is TPBi ($E_{HOMO} = -6.2$ eV, $E_{LUMO} = -2.7$ eV, $E_T = 2.7$ eV). A 25 nm-thick layer is obtained by spincoating. To avoid the dissolution of the previously deposited organic layers, PEI and ZrO_2:Y nanoparticles are deposited from aqueous dispersions. The fabrication processes for the top and bottom OLEDs are identical.

The optoelectronic characteristics of the regular tandem OLEDs are plotted in Figure 6.4. Similar to the devices with inverted architecture, regular sub-OLEDs show outstanding performance with low onset voltages of $V_{on,bottom} = V_{on,top} = 3.2$ V and high current efficiencies up to $\eta_{c,bottom} = \eta_{c,top} = 90$ cd/A. The luminances of the tandem OLEDs are, again, perfect addition of the luminances of the single devices. The J-V curves in Figure 6.4a show that, at an operating current of $J = 0.1$ mA/cm^2, the corresponding voltage for both single OLEDs are $V_{bottom} = V_{top} = 4.3$ V. The corresponding tandem device voltage is $V_{tandem} = 8.7$ V. The same behavior is observed for the onset voltage (at 1 cd/m^2). Notably, the onset voltage of the tandem OLED is the addition of the two single OLEDs, $V_{on,tandem} = V_{on,bottom} + V_{on,top} = 6.4$ V. The luminance as well as the current efficiency of the tandem OLED doubles the values of the single devices. The highest current efficiency of the tandem $\eta_{c,tandem} = 184$ cd/A is accomplished at around 3000 cd/m^2. Accordingly, the perfect addition of voltages, onset voltages, luminance and current efficiencies are observed. The performance of all regular OLEDs also match the performance of the inverted devices, which is a good indicator for excellent energy level alignment throughout the device regardless the orientation of the layer stack.
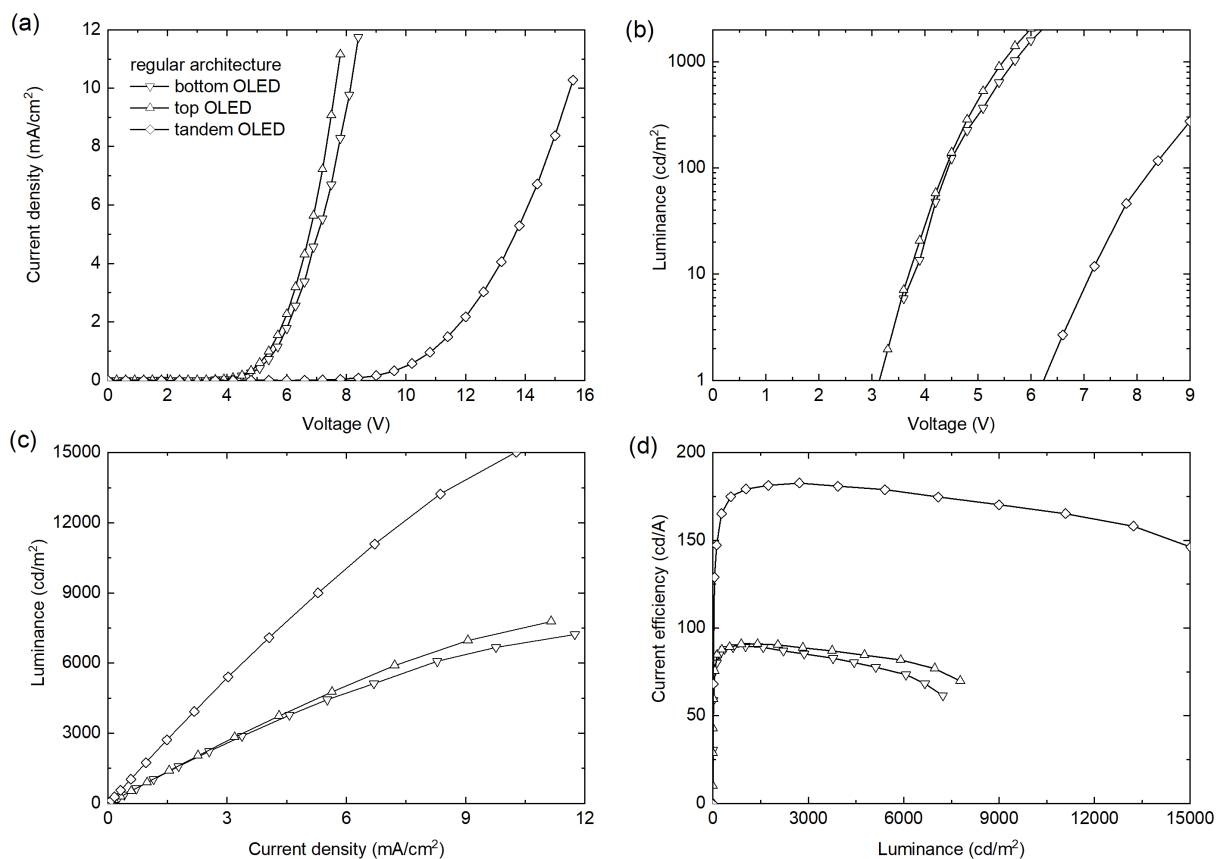
Figure 6.4: Optoelectronic properties of regular tandem OLEDs (diamond) comprising the green emitter SM-green-A in comparison to its corresponding bottom (down triangle) and top (up triangle) reference OLEDs: (a) J-V curves, (b) L-V curves, (c) L-J curves, (d) current efficiency versus luminance.

6.3 Fluorescent Tandem OLEDs

The realization of phosphorescent tandem OLEDs with regular and inverted architecture demonstrates the novelty of this CGL. All materials used in this CGL are robust against solvents used for the top light emitting unit. PEDOT:PSS does not dissolve in aromatic solvents, the nanoparticle layers (ZrO_2:Y und WO_3) can hardly be washed away, while PEI adheres firmly to the surfaces. Therefore, any emission layer that can be processed from common aromatic solvents such as toluene can be incorporated into this architecture. To demonstrate its universality, besides the phosphorescent small molecule SM-green-A, a fluorescent light-emitting polymer Super Yellow is integrated into the all-solution processed tandem OLED architecture.

Super Yellow is a commercially available light-emitting polymer, therefore, it can demonstrate the universality of this CGL. The device characteristics in Figure 6.5 show similar properties to the phosphorescent devices. The tandem device performs as an addition of two sub-OLEDs. Likewise, the curves of the regular and inverted architectures are similar. To drive the device with a current density of
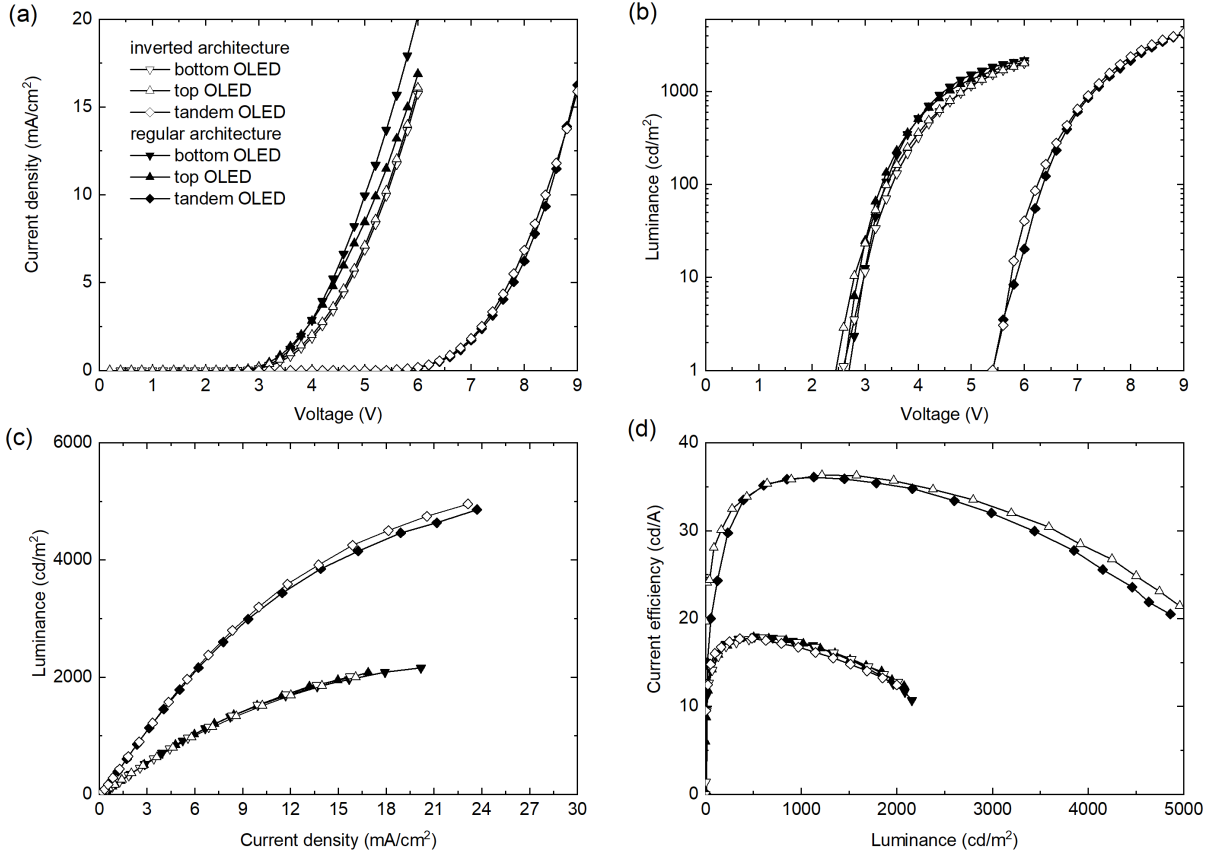
Figure 6.5: Optoelectronic characteristics of tandem OLEDs (diamond) comprising the fluorescent emitter polymer Super Yellow in comparison to the corresponding bottom (down triangle) and top (up triangle) references: (a) J-V curves, (b) L-V curves, (c) L-J curves, (d) current efficiency.

$J = 0.1\,\mathrm{mA/cm^2}$, the required operation voltages for inverted and regular bottom sub-OLEDs are $V_{\mathrm{inv,bottom}} = V_{\mathrm{reg,bottom}} = 3\,\mathrm{V}$, whereas both top sub-OLEDs require $V_{\mathrm{inv,top}} = V_{\mathrm{reg,top}} = 2.9\,\mathrm{V}$. The corresponding tandem OLEDs operate at the sum of the corresponding single OLEDs $V_{\mathrm{inv,tandem}} = 5.8\,\mathrm{V}$ and $V_{\mathrm{reg,tandem}} = 5.9\,\mathrm{V}$. The onset voltages of the inverted bottom and top OLEDs are $V_{\mathrm{on,inv,bottom}} = 2.6\,\mathrm{V}$ and $V_{\mathrm{on,inv,top}} = 2.5\,\mathrm{V}$, respectively. The onset voltages of both OLEDs are close to the bandgap of Super Yellow (2.4 eV), indicating efficient charge carrier injection. The sum of the voltages of the sub-OLEDs is approximately the same as the onset voltage for inverted tandem OLEDs ($V_{\mathrm{on,inv,tandem}} = 5.4\,\mathrm{V}$). For the regular devices, low onset voltages of the single devices are also observed, with $V_{\mathrm{on,reg,bottom}} = 2.7\,\mathrm{V}$ and $V_{\mathrm{on,reg,top}} = 2.6\,\mathrm{V}$, while the voltage of the tandem device is roughly the addition of both single references ($V_{\mathrm{on,inv,tandem}} = 5.4\,\mathrm{V}$) as depicted in Figure 6.5b. To maintain the same luminance, the current of the tandem OLED is only half of the current in the single devices (Figure 6.5c). For example, to generate a luminance of $1000\,\mathrm{cd/m^2}$, all single devices require about $J_{\mathrm{single}} = 6\,\mathrm{mA/cm^2}$, whereas the operating current density of the tandem OLEDs is only $J_{\mathrm{tandem}} = 2.6\,\mathrm{mA/cm^2}$. Thus the current efficiency of the tandem
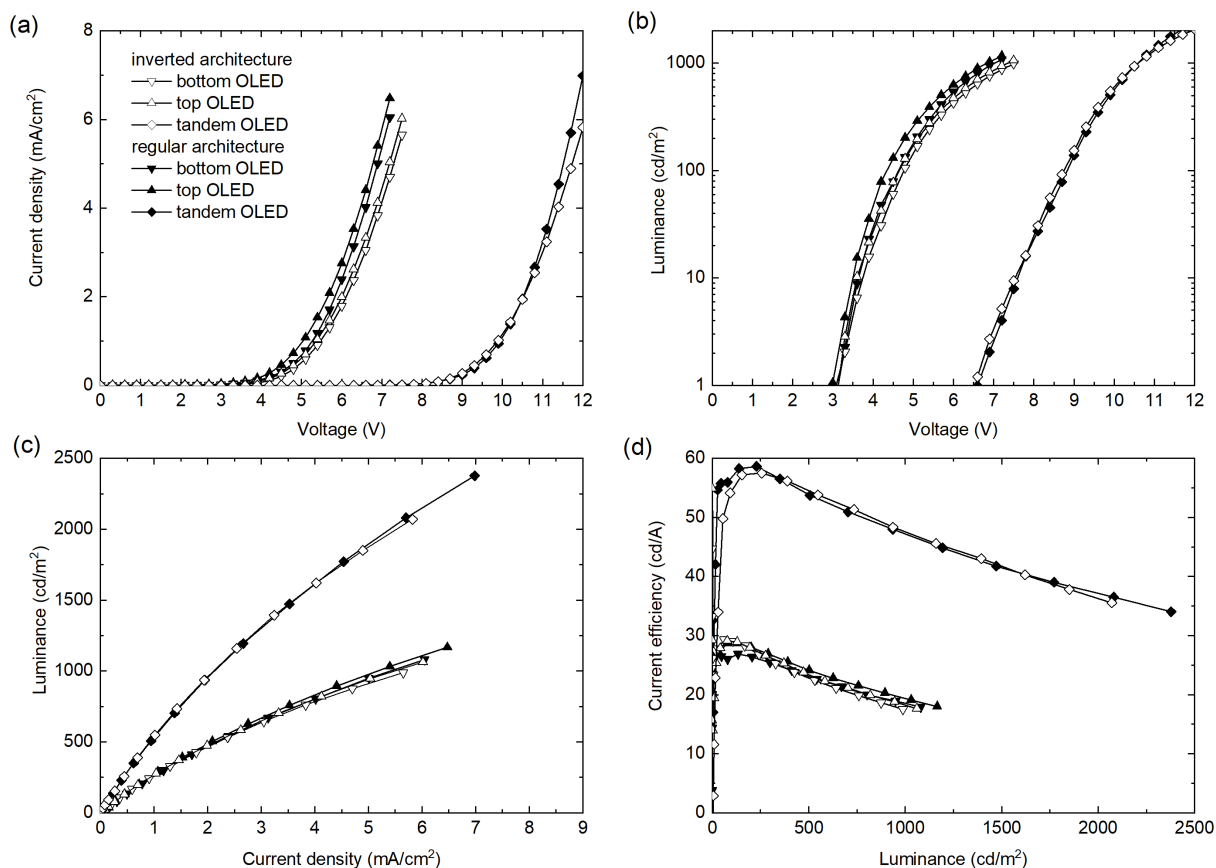
Figure 6.6: Optoelectronic characteristics of tandem OLEDs (diamond) comprising the light-emitting CuI:MePyrPHOS complex in comparison to the corresponding bottom (down triangle) and top (up triangle) references: (a) J-V curves, (b) L-V curves, (c) L-J curves, (d) current efficiency.

OLED is twice the efficiency of the single OLED. All single references, no matter whether inverted or regular, can reach $\eta_{c,single} = 18\,cd/A$, which are among the best reported current efficiencies for Super Yellow. The tandem OLEDs achieve a maximum current efficiency of $\eta_{c,tandem} = 36.3\,cd/A$. Owing to its fluorescent nature, Super Yellow yields only moderate performance. Yet, an overall identical behavior to SM-green-A OLEDs, in that all voltages, luminances and current efficiencies add up from the reference single OLEDs to the tandem OLED, is observed.

6.4 TADF Tandem OLEDs

The regular single TADF OLEDs have been presented in Chapter 5.2. Further investigations of the universality of this WO_3/PEDOT:PSS/ZrO_2:Y/PEI CGL is conducted with the green emitting CuI:MePyrPHOS complex.[148, 166] The performance data is depicted in Figure 6.6. Regardless of regular or inverted architecture, all voltages, luminances and current efficiencies add up from the reference single OLEDs to the

tandem OLED efficiencies. The TADF reference devices achieve decent performance with a low onset voltage of around $V_{on,single} = 2.5\,V$ and a current efficiency of around $\eta_{c,single} = 26\,cd/A$ at a luminance of $300\,cd/m^2$. The tandem devices clearly outperform the single references with a current efficiency of $\eta_{c,tandem} = 57\,cd/A$ which is twice the efficiency of the (reference) single OLEDs. The operating voltage ($V_{inv,tandem} = 8.4\,V$ and $V_{reg,tandem} = 8.4\,V$) for a given current density ($J = 0.1\,mA/cm^2$) and the onset voltage ($V_{on,inv,tandem} = 7.6\,V$ and $V_{on,reg,tandem} = 6.7\,V$) at a defined luminance of $L = 1\,cd/m^2$ add up, validating the tandem OLED functionality.

In conclusion, this universal solution processable CGL can be used in both regular and inverted tandem OLEDs. It is compatible with various light-emitting materials, regardless of fluorescence or phosphorescence. An yttrium doped zirconium oxide electron injection layer that is robust against the acidic PEDOT:PSS is the enabler of this tandem architecture. The incorporation of charge carrier blocking layers yields high device efficiencies and enhanced device lifetime.

Experimental: All OLEDs are fabricated on ITO coated glass substrates using the standard layout and are characterized in the OCS setup. All layer depositions follow the recipe in Table 6.1. The phosphorescent emitter SM-green-A was provided by Merck KGaA. Finally, a 200 nm-thick aluminum (Al) electrode is evaporated. In order to conduct lifetime measurements, all OLEDs are encapsulated. During the measurement, the OLEDs are kept in a climate chamber (30 °C, 30% rel. humidity).

7 Electron Injection Layers Comprising Cesium Fluoride

This chapter investigates a composite electron injection layer comprising metal oxide and cesium fluoride, that can be deposited from solution. Its low work function enables excellent performances with low onset voltage ($V_{on} = 2.6\,\mathrm{V}$) and high efficiency ($\eta_c = 17\,\mathrm{cd/A}$) in inverted Super Yellow OLEDs. Besides the common fluorescent polymer emitter Super Yellow, the phosphorescent small molecule IrMDQ₂(acac) is also incorporated as emitter. The devices exhibit a high current efficiency of $\eta_c = 12.5\,\mathrm{cd/A}$. The universality of producing low work function EILs by blending cesium fluoride with metal oxides is further proven by employing ZrO₂ and yttrium doped ZrO₂. Both electron injection layers produce Super Yellow OLEDs with current efficiencies higher than $18\,\mathrm{cd/A}$.

In the previous chapter, a low work function electron injection bilayers are investigated by applying an ultra-thin PEI layer ($\sim 4\,\mathrm{nm}$) on top of ZrO₂:Y. However, the deposition of two layers from solution including an ultra-thin layer can be problematic for large area devices. One possible approach to replace the bilayer is to doping alkali metal compounds into metal oxide to produce an electron injection layer for OLEDs. [167–169] Considering that evaporated CsF is used in many OLED architectures and it is solution processable, CsF can be considered a promising alternative solution processed EIL for OLEDs.[48, 170, 171]

7.1 Fluorescent OLEDs with Cesium Fluoride

As reported in the literature, thermally evaporated CsF is usually covered with conductive metal electrodes to produce low work function cathodes.[172, 173] Here, the effect of applying CsF directly on top of the ITO electrode is investigated. The OLED architecture is depicted in Figure 7.1a. Cesium fluoride (Sigma-Aldrich Corporation) is dissolved in isopropanol at various concentrations of $2\,\mathrm{mg/mL}$, $5\,\mathrm{mg/mL}$, $10\,\mathrm{mg/mL}$ and $15\,\mathrm{mg/mL}$. With respect to the energy levels of Super Yellow ($E_{\mathrm{HOMO}} = -5.4\,\mathrm{eV}$, $E_{\mathrm{LUMO}} = -3\,\mathrm{eV}$),

(a)

Ag

MoO$_3$

Super Yellow

CsF

ITO

Glass

(b)

E

ITO/CsF

-3.6 eV

-4.9 eV

ITO

-3.0 eV

-5.4 eV

Super Yellow

-4.3 eV

-5.9 eV

MoO$_3$

Ag
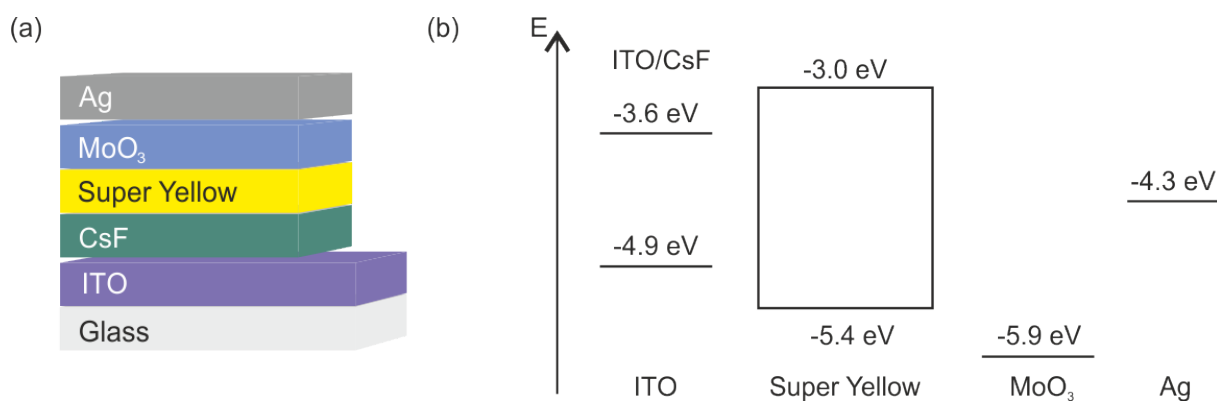
Figure 7.1: (a)Inverted OLED architecture comprising an ITO cathode and a Ag anode, where CsF is employed as EIL while MoO$_3$ is evaporated as HIL. The polymer Super Yellow is incorporated as emission layer. (b) Energy diagram of the inverted OLED architecture. Upon depositing CsF atop ITO, its work function is reduced from 4.9 eV to 3.6 eV. Due to the high work function of MoO$_3$ (5.9 eV), no hole injection barrier to HOMO of Super Yellow is formed.

MoO$_3$ with a high work function of $\Phi = 5.9$ eV is evaporated as HIL to facilitate the hole injections. The energy diagram is illustrated in Figure 7.1b.

The optoelectronic characteristics of OLEDs comprising neat CsF are plotted in Figure 7.2. It illustrates that the onset voltages of OLEDs with CsF layers applied from 2 mg/mL and 15 mg/mL solutions are around $V_{on} = 3.8$ V, while the devices with CsF layers from 5 mg/mL and 10 mg/mL show much lower onset voltages of $V_{on} = 3$ V. Notably, the current efficiency of the OLEDs employing CsF layers from 5 mg/mL solution stands out (Figure 7.2c). The same trend is observed in the power efficiencies in Figure 7.2d.

To explore the origin of the superior behavior of CsF layer from 5 mg/mL solution, topography images of CsF layers with different concentrations (2 mg/mL, 5 mg/mL, 10 mg/mL and 15 mg/mL) atop ITO are shown in Figure 7.3. Notably, in Figure 7.3a, instead of forming a closed layer on ITO, CsF from 2 mg/mL solution randomly distributes at the surface and the ITO flakes beneath CsF still remain visible. Thus, although the work function of CsF (2 mg/mL) atop ITO is $\Phi = 3.6$ eV (measured by KPFM), the excitons are still likely to quench at the vicinity of ITO electrode.[22] Consequently, the current efficiency and power efficiency of these OLEDs can only reach up to $\eta_c = 4$ cd/A and $\eta_p = 1$ lm/W.

When CsF solution has a concentration of 5 mg/mL, the ITO flakes cannot be observed and a thin layer of CsF is detected atop ITO (Figure 7.3b). Its work function is determined to $\Phi = 3.6$ eV (KPFM measurements), thus leading to lower onset voltage ($V_{on} = 3$ V), higher current efficiency of $\eta_c = 8$ cd/A and power efficiency of $\eta_p = 4$ lm/W. As demonstrated in Figure 7.3c and d, larger CsF crystals are detected towards increasing concentrations (10 mg/mL and 15 mg/mL). The root mean square roughness (R_q) of the topography, an indicator of the layer homogeneity, increases dramatically from $R_q =$
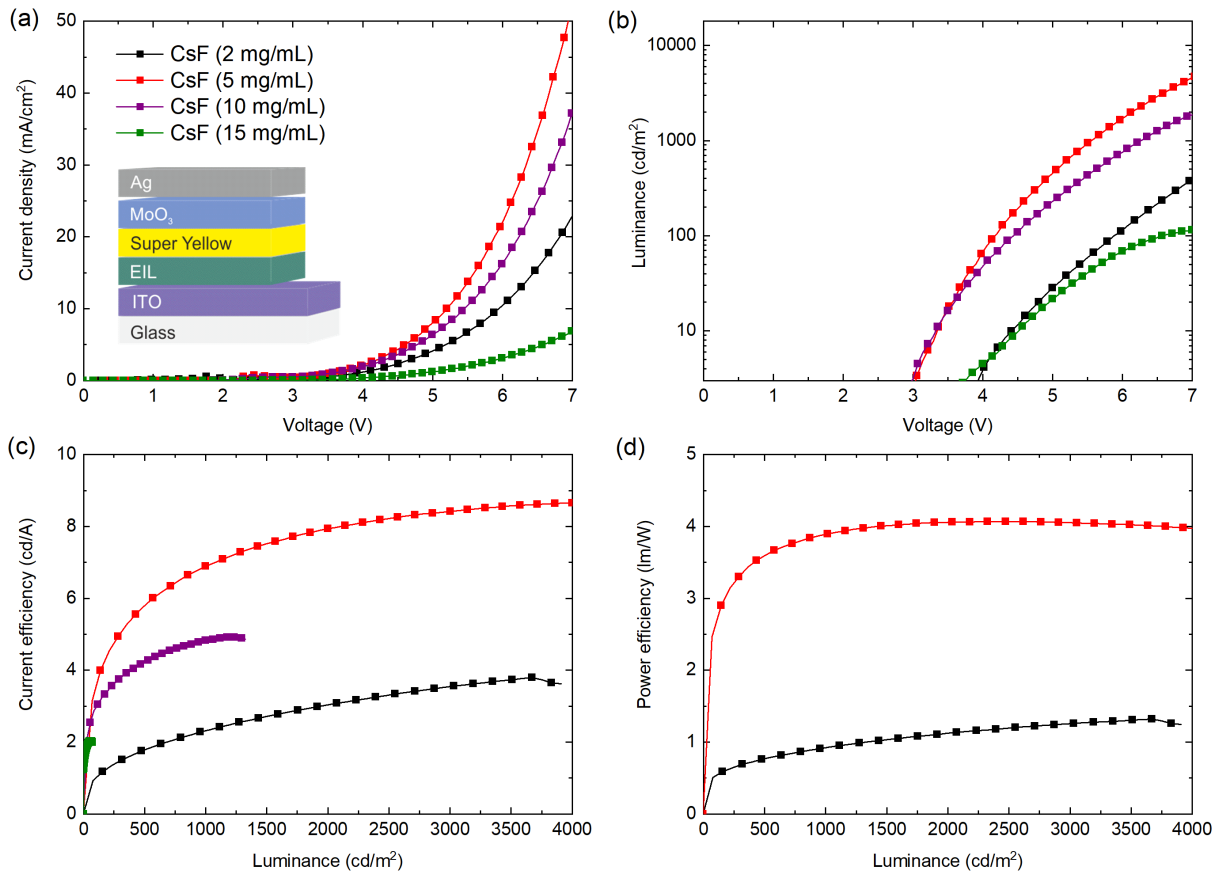
Figure 7.2: Optoelectronic characteristics of IOLEDs incorporating neat CsF, where CsF is deposited from isopropanol solutions with concentrations of $2\,mg/mL$, $5\,mg/mL$, $10\,mg/mL$ and $15\,mg/mL$. (a) Current density versus voltage curves. (b) Luminance versus voltage curves show an onset voltage. (c) Current efficiencies at different luminances. (d) Power efficiency versus luminance.

$7.8\,nm$ at a concentration of $5\,mg/mL$ to $R_q = 36.3\,nm$ at $15\,mg/mL$. The highest spikes exceed $100\,nm$ if the CsF concentration in solution exceeds $10\,mg/mL$. Considering that the emission layer (Super Yellow) thickness is only $70\,nm$, such high peaks on the CsF surface impede efficient OLEDs. Thus the current and power efficiencies of both OLEDs are low.

Compared to the OLEDs without any EIL, where no electroluminescence is observed, devices with CsF electron injection layer show enhanced performance. According to Huang et al., the improved device performance of introducing CsF as EIL is attributed to the thin dipole layer formed at the ITO/CsF interface, leading to a reduced work function of the ITO surface.[171, 174] Yet, even the optimum CsF layer surface appears to be rather rough with peaks more than $60\,nm$ due to crystallization. Consequently the optimized devices are not among the best reported OLEDs with Super Yellow as emissive material. As demonstrated in Figure 7.1b, the work function of ITO/CsF is $\Phi = 3.6\,eV$ and the LUMO energy of Super Yellow is around $E_{LUMO} = -3\,eV$, thus an electron injection

(a)

44.0 nm

0.0   5.0 μm

(b)

60.0 nm

0.0   5.0 μm

(c)

124.0 nm

0.0   5.0 μm

(d)

161.0 nm

0.0   5.0 μm
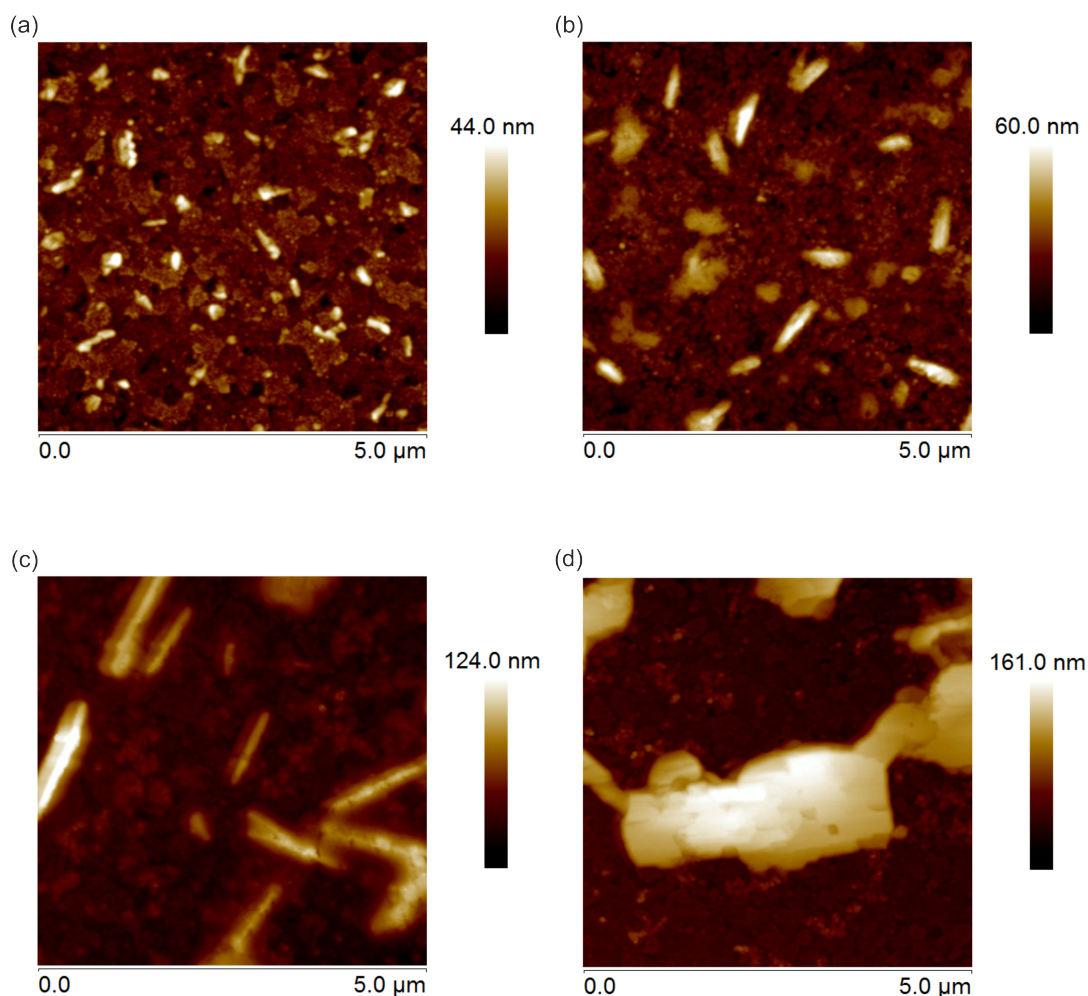
Figure 7.3: AFM images of CsF atop of the ITO electrode. The CsF layers are processed from isopropanol solutions with concentrations of (a) $2\,mg/mL$, (b) $5\,mg/mL$, (c) $10\,mg/mL$ and (d) $15\,mg/mL$. The corresponding root mean square roughnesses are $R_q = 5.4\,nm$, $R_q = 7.8\,nm$, $R_q = 18.1\,nm$ and $R_q = 36.3\,nm$, respectively. At a lower concentration of $2\,mg/mL$, the CsF solution does not form a closed layer after spincoating, while solutions with higher concentrations, e.g. $10\,mg/mL$ and $15\,mg/mL$, result in undesirable CsF crystallization.

barrier of $0.6\,eV$ still prevails. This Schottky contact between the cathode and emission layer illustrates the necessity of further lowering the work function difference between the cathode and Super Yellow. In other words, the surface roughness and the work function of the electron injection layer must be minimized in order to achieve outstanding device performances.

7.2 Fluorescent OLEDs with ZnO:CsF Composite

ZnO is a common electron transport material for organic solar cells, which can be easily deposited solution. As shown in Figure 7.4, OLEDs with pure ZnO layers obtained form nanoparticle dispersions show a relatively high onset voltage of $V_{on} = 3.2\,V$, a low current
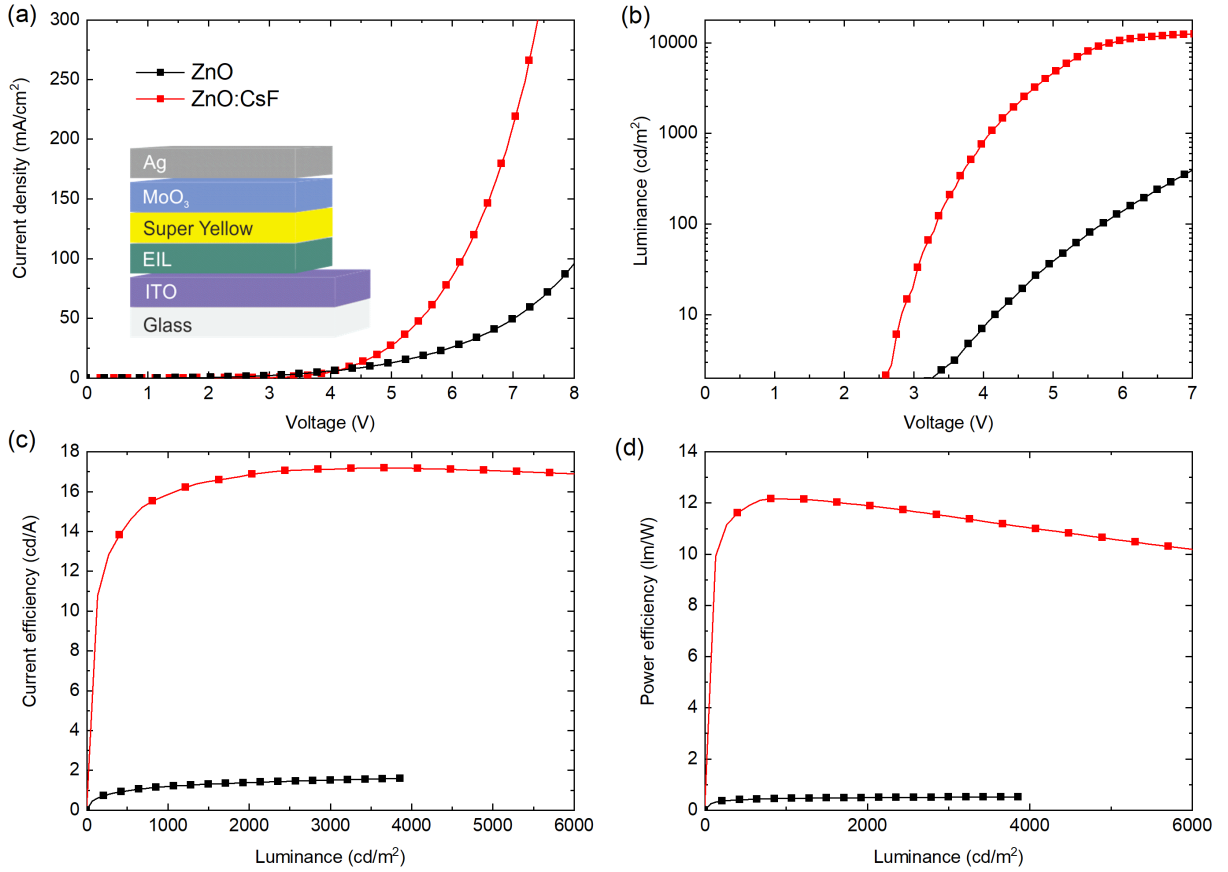
Figure 7.4: Optoelectronic characteristics of inverted polymer OLEDs with device architecture depicted in Figure 7.5, where pure ZnO or a ZnO:CsF mixture is employed as EIL. (a) J-V curves. (b) The luminance versus voltage curves show that the onset voltages of the OLEDs with ZnO:CsF are significantly lower than the onset voltages of devices with pure ZnO. (c) Current efficiency versus luminance. (d) Power efficiency versus luminance.

efficiency of $\eta_c = 1.5 \, \mathrm{cd/A}$ and a poor power efficiency of $\eta_p = 0.5 \, \mathrm{lm/W}$, rendering ZnO itself as unsuitable EIL for OLEDs. The reason can partly be attributed to its high work function ($\Phi = 3.9 \, \mathrm{eV}$), leading to a rather large electron carrier injection barrier exists between cathode and emission layer. Yet, the ZnO layer on ITO is quite homogeneous with $R_q = 6.1 \, \mathrm{nm}$.

Park et al. have reported that adding Cs_2CO_3 can greatly reduce the work function of TiO_2 and they attribute it to the doping of Cs.[168] Here the influence of blending CsF into ZnO is investigated. The ZnO:CsF composite layer is obtained by spincoating a mixture of the ZnO nanoparticle dispersions and the CsF solutions. The OLED architecture and the corresponding energy diagram are depicted in Figure 7.5. In comparison to $\Phi = 3.9 \, \mathrm{eV}$ of pure ZnO layer, the work function of the composite layer is only $\Phi = 3.1 \, \mathrm{eV}$, hinting at an ohmic contact at the cathode/Super Yellow interface. Different compositions of ZnO and CsF are tested. The optimum composite comprises ZnO and CsF at a weight ratio of 5:8 (wt/wt). The corresponding optoelectronic characteristics are plotted in Figure 7.4.

(a)

(b)
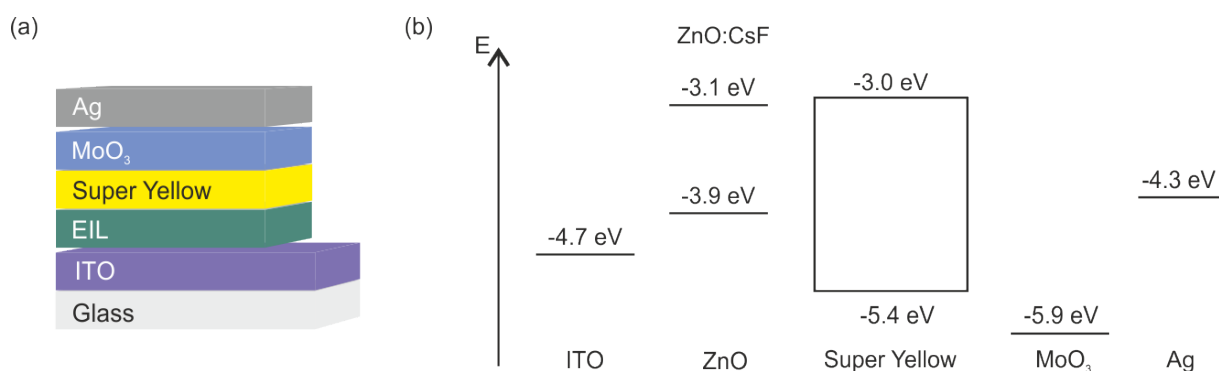
Figure 7.5: (a) Inverted OLED architecture incorporating either ZnO or a mixture of ZnO and CsF as EIL. (b) The corresponding energy diagram. By blending CsF into the ZnO layer, the work function of the EIL is reduced from $\Phi = 3.9\,\text{eV}$ of that neat ZnO layer to $\Phi = 3.1\,\text{eV}$.

a)

b)
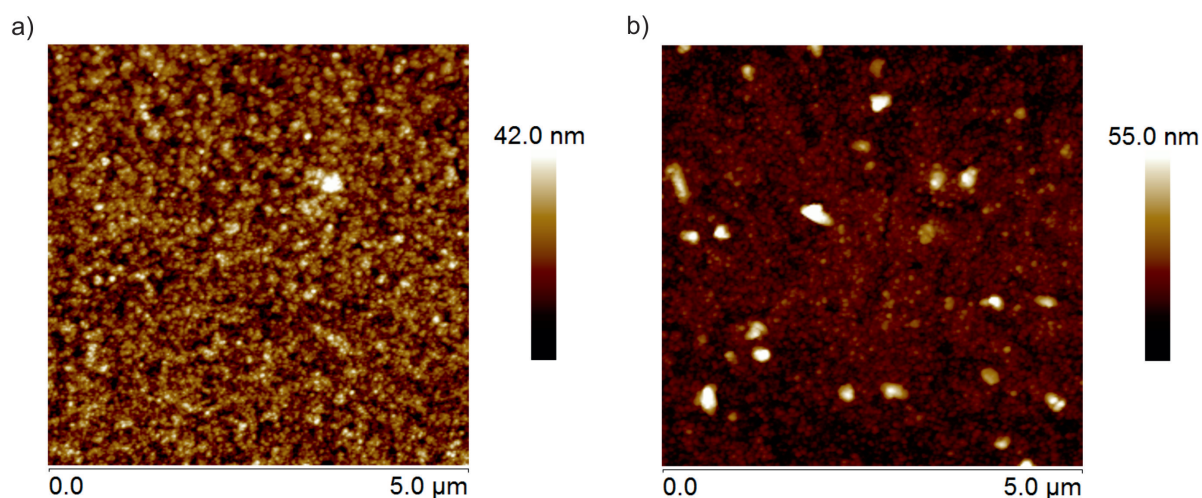
Figure 7.6: AFM images of layers deposited from (a) ZnO nanoparticles and (b) a blend of ZnO nanoparticles and CsF with a weight ratio of 5:8 (wt/wt) on top of ITO. The root mean square roughnesses are $R_q = 6.1\,\text{nm}$ and $R_q = 6.15\,\text{nm}$, respectively.

The onset voltage is reduced to $V_{on} = 2.6\,\text{V}$, due to efficient charge carrier injection. The inverted OLEDs can reach a current efficiency of up to $\eta_c = 17\,\text{cd/A}$ (at $3000\,\text{cd/m}^2$) and the power efficiency can achieve $\eta_p = 12\,\text{lm/W}$. These characteristics indicate that the performances of IOLEDs with ZnO:CsF are comparable to the reported devices comprising ZnO/PEI bilayers to facilitate electron injections.[22] Figure 7.6 shows AFM images of the EILs deposited from pure ZnO nanoparticle dispersions and the ZnO:CsF blend. The roughness of the ZnO layer is $R_q = 6.1\,\text{nm}$. The composite layer exhibits a similar $R_q = 6.15\,\text{nm}$, implying that the ZnO nanoparticles hinder the crystallizations of CsF. Owing to its low work function and its ability to form homogeneous layer, the ZnO:CsF mixture can be considered as an easy-to-apply EIL alternative to the previously reported metal oxide/PEI bilayer.

7.3 Phosphorescent OLEDs with ZnO:CsF Composite

As discussed in Chapter 3.6, the efficiencies of the fluorescent OLEDs are intrinsically limited since triplet excitons are not utilized for photon emissions. Therefore iridium based phosphorescent OLEDs are widely considered superior to the fluorescent devices. Yet, small molecule based phosphorescent materials are difficult to introduce into solution processed devices, since the layers can easily be washed out by the following solvents. In addition, phosphorescent OLEDs usually require exciton blocking layer so that the long-living triplet excitons can be confined in the emissive layer. Yet the exciton blocking layer consists mostly an organic material which can be dissolved in the common organic solvent. These issues make the solution processed phosphorescent OLED stacks very challenging. If the exciton blocking layer is omitted, the emission layer needs careful design to make sure the triplet excitons are confined in the emission layer.

In this work, a polymer matrix is necessary to affix the small molecules. Here, phosphorescent IOLEDs based on solution processed ZnO:CsF layer are presented. The corresponding device architecture and the energy diagram are depicted in Figure 7.7. To deposit the EIL, ZnO nanoparticle dispersion and CsF solution are mixed at a weight ratio of 10:11 (wt/wt). In the emission layer, poly(N-vinylcarbazole) (PVK) ($E_{HOMO} = -5.8\,eV$, $E_{LUMO} = -2.2\,eV$, $E_T = 2.5\,eV$) is used as host and the polymer matrix for the red phosphorescent emitter iridium-(III)bis (2-methyldibenzo-[f,h] quinoxaline) (acetylacetonate) (Ir(MDQ)$_2$(acac)) ($E_{HOMO} = -5.7\,eV$, $E_{LUMO} = -2.5\,eV$, $E_T = 2.1\,eV$).[69, 177, 178] To achieve balanced charge carrier transport in the emission layer, the electron and hole transporting materials 1,3-bis[2-(4-tert-butylphenyl)-1,3,4,-oxadiazo-5-yl] (OXD-7, $E_{HOMO} = -6.3\,eV$, $E_{LUMO} = -2.4\,eV$, $E_T = 2.7\,eV$) and tris(4-carbazoyl-9-ylphenyl)amine (TCTA, $E_{HOMO} = -5.7\,eV$, $E_{LUMO} = -2.4\,eV$, $E_T = 2.9\,eV$) are incorporated, too.[136, 175] PVK, OXD-7, TCTA, Ir(MDQ)$_2$(acac) are mixed at a weight ratio of 49:45:5:1 and then spincoated, producing an emission layer thickness of d = 60 nm. The chemical structures of all the organic materials can be found in Figure 7.8.

In the emission layer, all host compounds (PVK, OXD-7, TCTA) possess higher triplet energies than Ir(MDQ)$_2$(acac) (Figure 7.7b), which is a mandatory property in order to effectively confine triplet excitons effectively in the emitter. In this case, the electron injection barrier from ZnO:CsF and the hole injection barrier from PEDOT:PSS to emission layer are substantial. Thus the voltage versus luminance curve in Figure 7.9a (inset) shows a rather high onset voltage ($V_{on} = 8.3\,V$). Notably, due to the limitations of solution processes, no charge carrier blocking layers are introduced in this architecture which leads to a current leakage, thus a high onset voltage. Nevertheless, this value is still comparable to the voltage ($V_{on} = 7 - 8\,V$) required to obtain $2\,cd/m^2$ from solution
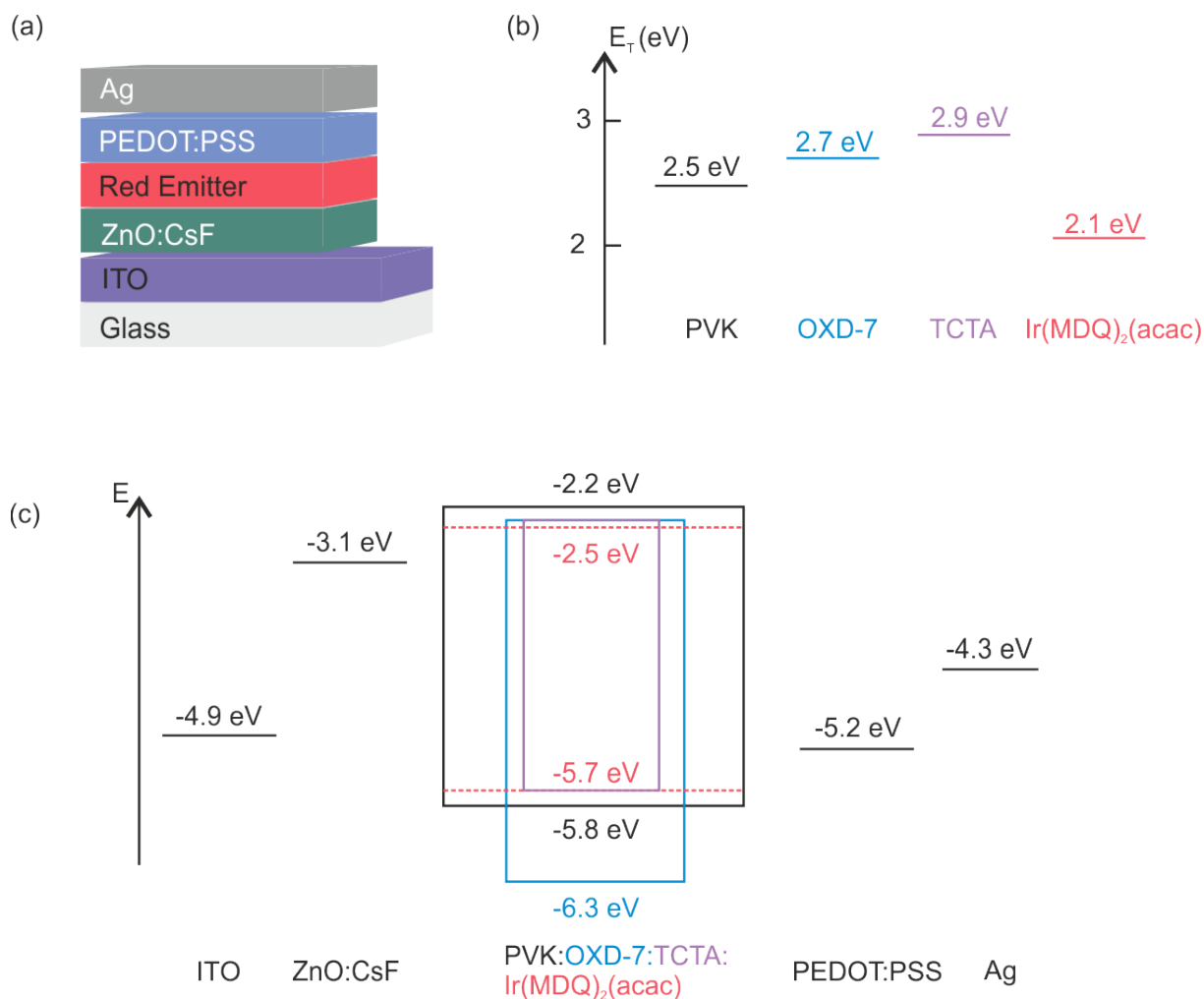
Figure 7.7: (a) Solution processed phosphorescent OLED architecture, where a blend of ZnO and CsF is used to facilitate the electron injection, and the solution processed polymer PEDOT:PSS is employed as hole injection layer. The red phosphorescent emission layer consists of the polymer PVK and the small molecules TCTA, OXD-7 and Ir(MDQ)$_2$(acac). (b) Triplet energies of all materials in the emission layer. (c) The corresponding energy diagram of the red emitting OLED. Although ZnO:CsF shows a rather low work function, electron and hole injection barriers still prevail.[175, 176]
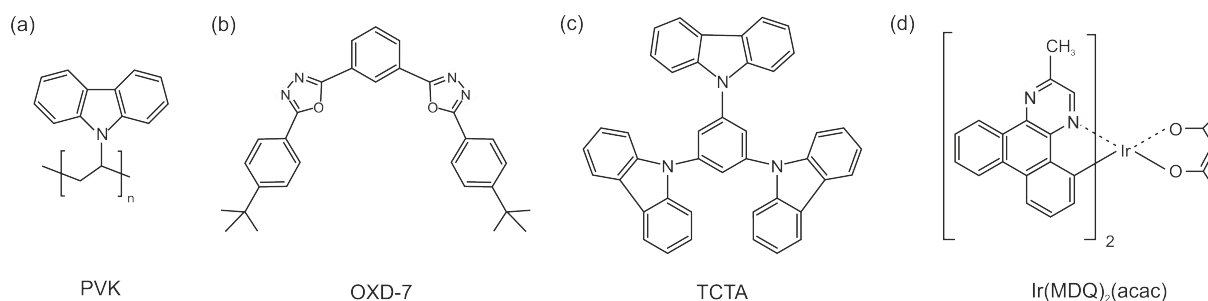
Figure 7.8: Molecular structures of (a) PVK, (b) OXD-7, (c) TCTA and (d) Ir(MDQ)$_2$(acac).[7, 179, 180]
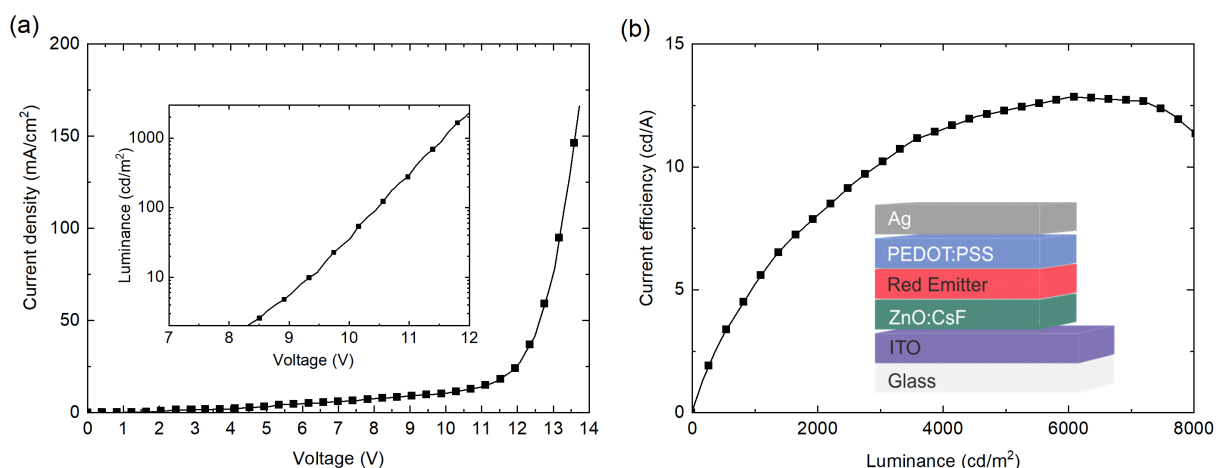
Figure 7.9: Optoelectronic characteristics of inverted phosphorescent OLEDs employing electron injection layer from a mixture of ZnO and CsF. (a) J-V curve. Inset: the onset voltage (at $2\,\mathrm{cd/m^2}$. (b) The current efficiency versus luminance.

processed phosphorescent OLEDs reported by Chiba et al., where they incorporated bilayer of metal oxide and surface modifier.[139] As shown in Figure 7.9b, despite of the high onset voltage, the completely solution processed red emitting devices can achieve a current efficiency of $\eta_c = 12.5\,\mathrm{cd/A}$ at a high luminance of $6000\,\mathrm{cd/m^2}$.

7.4 Fluorescent OLEDs with ZrO$_2$:CsF Composite

Like the well-known ZnO, the metal oxide zirconium oxide (ZrO$_2$) can also be used for electron injection.[43] However, ZrO$_2$ is less intrinsically doped than ZnO. With its deep valence band at $-8.7\,\mathrm{eV}$, ZrO$_2$ may exhibit superior hole blocking abilities compared to ZnO.[43] Here, the properties of solution processable ZrO$_2$ and its integration into IOLEDs are investigated.

Although ZrO$_2$ is supposed to have a high conduction band at $-3\,\mathrm{eV}$ and a valence band of $-8.7\,\mathrm{eV}$, KPFM measurement show its work function at $\Phi = 4\,\mathrm{eV}$, indicating its intrinsic n-doping property.[43] Because its work function is similar to the work function of ZnO ($\Phi = 3.9\,\mathrm{eV}$), a rather large electron injection barrier exists upon its incorporation into inverted OLEDs (Figure 7.10b, inset, black curves). The OLEDs' properties are depicted in Figure 7.10. The high onset voltage of $V_{on} = 2.8\,\mathrm{V}$ of the OLEDs confirms this electron injection barrier. Consequently, only a moderate current efficiency of $\eta_c = 2\,\mathrm{cd/A}$ is obtained. To further reduce the work function of the EIL, a blend of ZrO$_2$ nanoparticles and CsF with weight ratio of 1:2 is spin cast atop the ITO. For direct comparison, the characteristics of a representative OLED are plotted in Figure 7.10 (red curves).

According to KPFM measurements, the ZrO$_2$:CsF layer exhibits a work function of $\Phi = 3.2\,\mathrm{eV}$ which is comparable to that of ZnO:CsF ($\Phi = 3.1\,\mathrm{eV}$). Thus electrons can be
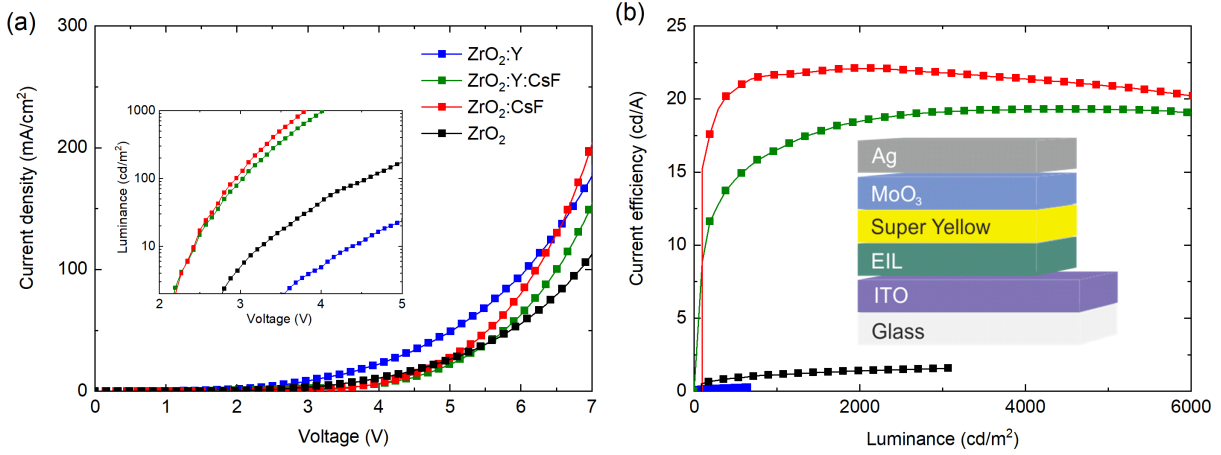
Figure 7.10: (a) Current density-voltage (J-V) curves of inverted OLEDs incorporating pure ZrO_2, the mixture of ZrO_2 and CsF (ZrO_2:CsF), yttrium doped ZrO_2 (ZrO_2:Y) or blend of ZrO_2:Y and CsF ((ZrO_2:Y):CsF) as EIL. Inset shows the corresponding voltage-luminance (V-L) curves. It also reveals the respective onset voltage of at $2\,cd/m^2$. (b) Current efficiency of these OLEDs at different luminances. Inset: The inverted OLED architecture.

efficiently injected into the emission layer, resulting in a lower onset voltage of $V_{on} = 2.2\,V$ compared to $V_{on} = 2.8\,V$ of the devices with the neat ZrO_2 layer. The current efficiency of the OLEDs incorporating EILs from the ZrO_2:CsF composite can reach up to $\eta_c = 22\,cd/A$. Compared to OLEDs comprising the ZnO:CsF composite ($V_{on} = 2.6\,V$, $\eta_c = 17\,cd/A$), the devices with ZrO_2:CsF achieve better performances. Since Super Yellow exhibits better hole mobility than electron mobility, the emission zone is expected in the vicinity of the EIL. Hence an EIL with improved hole blocking abilities such as ZrO_2:CsF can improve the device performance.[181]

In addition to neat ZrO_2, an yttrium doped zirconium oxide (ZrO_2:Y) nanoparticle dispersion is investigated using the same device architecture. ZrO_2:Y exhibits a similar work function ($\Phi = 4.1\,eV$) as ZrO_2, yet, the stability and electron mobility is enhanced via yttrium doping. This is confirmed by the J-V curves in Figure 7.10a that a higher current is observed in OLEDs with neat ZrO_2:Y than with neat ZrO_2. Upon blending CsF and ZrO_2:Y, the same work function as for ZrO_2:CsF is observed ($\Phi = 3.2\,eV$). Thus OLEDs with low onset voltages ($V_{on} = 2.2\,V$) and a high current efficiencies ($\eta_c = 18\,cd/A$) are obtained.

In this work, several efficient inverted OLED architectures with solution processable electron injection layers are presented. The EIL is fabricated from mixtures of CsF and metal oxide nanoparticles, namely ZnO, ZrO_2 and ZrO_2:Y. All OLEDs incorporating the blend of metal oxide and CsF show superior performance over these employing neat metal oxide. Thus adding solution processable CsF to the metal oxide nanoparticle dispersions is an universal approach to generate low work function electron injection layers. The low work function of EIL minimizes the electron injection barrier and

enhances the performance of the inverted OLEDs. Both the common fluorescent emitting polymer Super Yellow and the phosphorescent small molecules have shown impressive optoelectronic properties in OLEDs.

Experimental: All OLEDs are fabricated on ITO coated glass substrates using the standard OLED layout and are characterized in the OCS setup. The work function measurements are accomplished by KPFM, with HOPG as the reference. The ZnO nanoparticle dispersion (Avantama AG, N-10, 2.5 wt.%) is first diluted in isopropanol to produce a 0.55 wt.% dispersion and then spincoated. The ZrO_2 nanoparticle dispersion (2.5 wt.% in isopropanol, Avantama AG) is diluted to 0.55 wt.% before deposition. All electron injection layers are spincoated at 4000 rpm for 30 s, followed by an annealing procedure at 150 °C for 10 min. For the fabrication of the fluorescent OLEDs, Super Yellow is spin cast from toluene solution (4 mg/mL) at 1000 rpm for 45 s, then 4000 rpm for 3 s, producing a layer thickness of 70 nm. Then 10 nm molybdenum oxide is vacuum deposited as hole injection layer which is then covered by 100 nm silver anode.

For the fabrication of the phosphorescent OLEDs, PVK, OXD-7, TCTA, $Ir(MDQ)_2(acac)$ are separately dissolved in chlorobenzene and then mixed at a weight ratio of 49:45:5:1 (wt/wt/wt/wt) to reach a total concentration of 20 mg/mL. Then, the mixed solution is deposited onto the EIL by spincoating (1000 rpm, 45 s; 4000 rpm, 3 s) and annealing (130 °C, 10 min) in the glovebox, resulting in an emission layer with a thickness of 60 nm. PEDOT:PSS (Clevios HTL Solar) is diluted in isopropanol and water with a volume ratio of 5:4:1 (v/v/v) before it is spincast (4000 rpm, 60 s) atop the emission layer and annealed (100 °C, 10 min) to achieve a 30 nm-thick film. Finally, 100 nm Ag anode is vacuum deposited.

8 Electron Injection Layers Incorporating PEI

In this chapter, a universal approach to produce a low work function electron injection layer is proposed by mixing PEI with metal oxides. The EIL comprising ZnO:PEI is optimized in an inverted device architecture and then incorporated into all-solution deposited transparent OLEDs on plastic substrates. The high work function anode is obtained by blending highly conductive PEDOT:PSS and PFI. The flexible OLEDs exhibit excellent mechanical robustness as evidenced in bending 1000 cycles. Likewise, the electron injection through ZrO₂:PEI is investigated and optimized in both regular and inverted OLED architectures.

A novel and facile approach to produce low work function EILs is proposed in Chapter 7 by mixing CsF with metal oxides, such as ZnO, ZrO_2 or yttrium doped ZrO_2. Nevertheless, the disadvantage of CsF is its poor chemical stability. The surface modifier PEI, on the other hand, is a rather stable material. Previously, PEI was admixed with ZnO (ZnO:PEI) in a sol-gel process, and successfully used as electron electron extraction layer for organic solar cells. The structural order of ZnO in the ZnO:PEI composite film was enhanced to align perpendicularly to the ITO electrode, enhancing electron transport.[182] However, a high conversion temperature of 200 °C for the ZnO precursor was used, hindering its application on flexible substrates and hence sacrificing one of the most important benefits of OLEDs [182] In contrast, the annealing of nanoparticle dispersions does not necessarily require high temperature. In this work, the effect of blending PEI into ZnO and ZrO_2 nanoparticle dispersions is studied.

8.1 Inverted OLEDs with ZnO:PEI Composite

Initially, the properties of ZnO:PEI composites are investigated by measuring their work function. The ZnO nanoparticle dispersion (2.5 wt% in isopropanol) is diluted in 1-propanol with 1:1.5 (v/v) before it is further mixed with PEI solutions (1 mg/mL, 2 mg/mL, 3 mg/mL and 4 mg/mL in 1-propanol) at a volume ratio of 1:1 (v/v). The
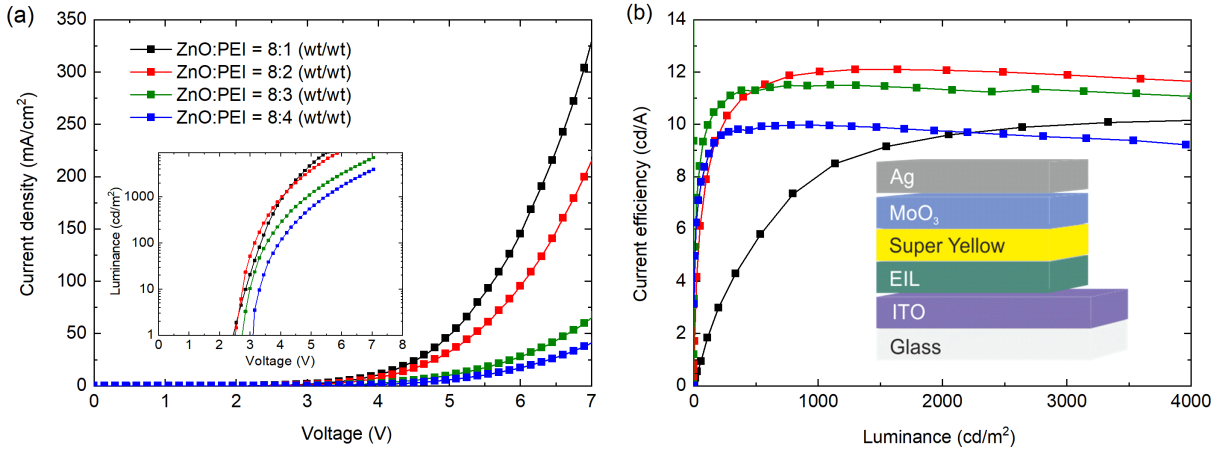
Figure 8.1: (a) Current density-voltage (J-V) curves of standard inverted OLEDs incorporating the composite of ZnO and PEI, where the weight ratio between ZnO and PEI variates from 8:1 (wt/wt) to 8:4 (wt/wt). The inset shows the voltage-luminance (V-L) curves, indicating the onset voltage of the devices at $1\,\mathrm{cd/cm^2}$. (b) Current efficiency at various luminances. Inset: Standard inverted OLED architecture.

corresponding weight ratios are calculated to be 8:1, 8:2, 8:3, 8:4 (wt/wt), respectively. The work functions of these four layers are determined by KPFM measurements and vary from $3.4\,\mathrm{eV}$ (ZnO:PEI = 8:1 (wt/wt)) to $3.6\,\mathrm{eV}$ (ZnO:PEI = 8:4 (wt/wt)). All measured work functions allow these layers to be applied as EILs in OLEDs. Accordingly, inverted Super Yellow OLEDs with the architecture in Figure 8.1b inset are fabricated and characterized using the integrating sphere setup. With increasing PEI concentration in the blend, the required voltage to achieve the same current density increases. This can be attributed to the insulator property of the PEI, that is, more PEI leads to lower conductivity. The same trend is observed for the device onset voltage. The onset voltages of devices with low amounts of PEI (ZnO:PEI = 8:1 (wt/wt) and 8:2 (wt/wt)) are similarly low (V_{on} = $2.5\,\mathrm{V}$ at $1\,\mathrm{cd/m^2}$). For the OLEDs with the highest PEI concentration (ZnO:PEI = 8:4 (wt/wt)), the onset voltage increases to V_{on} = $3.1\,\mathrm{V}$. This effect may partly be explained by the increasing work function. The best device performance is achieved with ZnO:PEI = 8:2 (wt/wt) (η_{c} = $12\,\mathrm{cd/A}$, η_{p} = $9.5\,\mathrm{lm/W}$ at $1000\,\mathrm{cd/m^2}$), matching the performance of state-of-art Super Yellow OLEDs, but mot importantly, avoiding any high annealing temperature. As such, this process is well compatible with OLED fabrication on plastic substrate.

Most OLEDs make use of opaque top electrodes, Yet, transparent OLEDs may open up new markets, such as windows integration or transparent displays. In order to reduce the fabrication costs for future mass production, the entire devices should be deposited from solutions. In this chapter, (i) all-solution processed (ii) transparent, (iii) flexible OLEDs are presented.
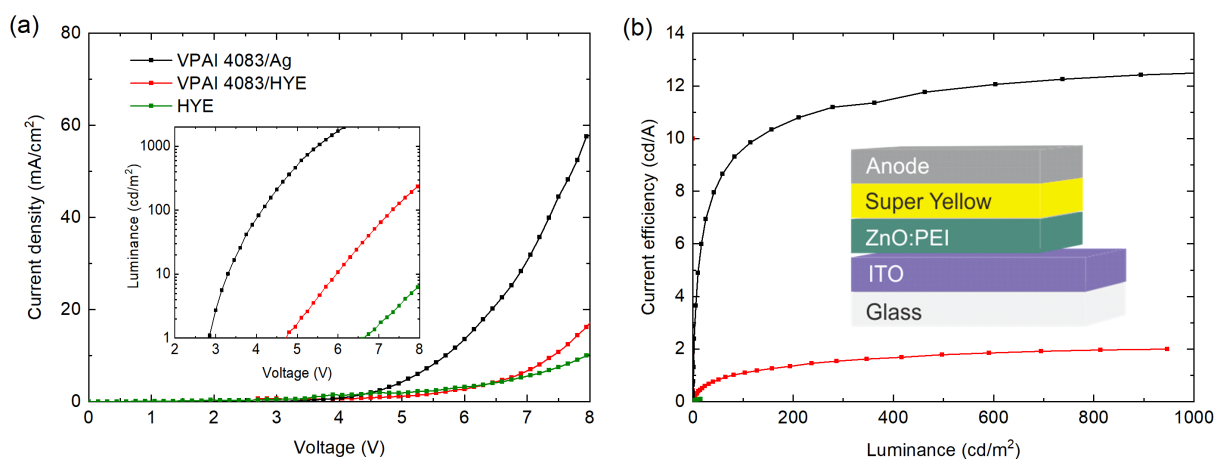
Figure 8.2: (a) J-V curves of the inverted OLEDs comprising different top electrodes. Inset: L-V curves indicate the onset voltages of the devices at $1\,cd/cm^2$. (b) Current efficiency versus luminance. Inset: OLED architecture. Three different anodes from VPAI 4083/Ag, VPAI 4083/HYE or neat HYE are deposited on top of Super Yellow.

8.1.1 Transparent OLEDs

In order to realize transparent OLEDs, the opaque metal top electrode (Ag) needs to be replaced by a transparent, conductive and solution processable material. Highly conductive PEDOT:PSS, an aqueous composite consisting of a π-conjugated polymer PEDOT and a counterion PSS, was employed as transparent electrodes in organic devices.[28, 29, 183, 184] To further increase the conductivity of PEDOT:PSS, silver nanowires (AgNWs) are incorporated into PEDOT:PSS (Clevios HY E, henceforth referred to as "HYE").[185] Here it is investigated as the top electrode (anode) for transparent OLEDs.

As discussed in Chapter 3.1, the work function of the anode is decisive. A HIL is only necessary if the work function of the anode is too low, so that the direct hole injection into the HOMO of the emission layer becomes inefficient. Upon incorporation of an anode with high work function, the HIL can be omitted. The work function of HYE is found at $\Phi = 4.7\,eV$ by PESA, resulting in a hole injection barrier of $0.7\,eV$ to the HOMO of Super Yellow ($E_{HOMO} = -5.4\,eV$). The patterning of the top electrode is described in Chapter 4.2. The area of each OLED pixel is afterwards measured under microscope. The respective OLED characteristics are plotted in Figure 8.2. Owing to the low work function of HYE, the OLEDs with pure HYE as anode show only moderate performance with high onset voltages of $V_{on} = 6.6\,V$ and negligible current efficiency. Therefore an additional HIL is essential between Super Yellow and HYE.

The most common solution processable hole injection material is a lower-conductive version of PEDOT:PSS (Clevios VPAI 4083, henceforth referred to as "VPAI 4083"), which is initially investigated as substitute for the evaporated MoO_3 in the inverted

architecture before.[186] In this chapter, to realize a homogeneous VPAI4083 layer atop Super Yellow, it is mixed with methanol and isopropanol at a ratio of 1:1:4 (v/v/v) before spincoating (4000 rpm, 40 s) and annealing (100 °C, 10 min). Then 100 nm silver is evaporated on top. VPAI 4083 exhibits a high work function of $\Phi = 5.1\,\text{eV}$, enabling efficient hole injection into Super Yellow. The corresponding OLED architecture and its performance are shown in Figure 8.2. With the black curves representing the IOLEDs with VPAI 4083 and silver anode, an onset voltage of $V_{on} = 2.9\,\text{V}$ (at $1\,\text{cd/m}^2$) and a current efficiency of $\eta_c = 12.5\,\text{cd/A}$ (at $1000\,\text{cd/m}^2$) are achieved, which are comparable to the OLEDs using MoO_3 ($V_{on} = 2.5\,\text{V}$, $\eta_c = 12\,\text{cd/A}$), demonstrating the decent hole injection function of VPAI 4083.

Consequently, VPAI 4083 is chosen as HIL between Super Yellow and the HYE anode. Notably, the devices show lower performance than the OLEDs with silver electrode (Figure 8.2). Although the onset voltage ($V_{on} = 4.7\,\text{V}$) is lower than the onset voltage of the OLEDs with pure HYE anode, it is still inferior to the references with Ag electrodes ($V_{on} = 2.9\,\text{V}$). As the OLEDs with neat HYE and VPAI 4083/HYE are transparent, the emission can be observed from both top and bottom directions. The luminances and the current efficiency in Figure 8.2 are calculated based on the bottom emission. The current efficiency of the devices with VPAI 4083/HYE is only $\eta_c = 2\,\text{cd/A}$, which is one sixth of the reference. The lower performance may be attributed to the water and organic solvent ($\sim 5\%$) content in HYE, which may redissolve the VPAI 4083 layer and Super Yellow underneath.

As discussed above, when using a high work function anode, the HIL becomes obsolete, which substantially simplifies the deposition procedures. Lee et al. discovered that by adding the polymer PFI (perfluorinated ionomer) into VPAI 4083, an enhanced HIL with higher work function is obtained.[33] Jeong et al. employed the highly conductive PEDOT:PSS and PFI composite to replace ITO in OLEDs.[187] Therefore, the blend of HYE and PFI is likely to act as a proper working anode. However, the mixed solutions of HYE and PFI (Nafion 117 solution, Sigma-Aldrich) do not produce a film on top of Super Yellow upon spincoating because of poor wetting properties. In order to obtain a layer from the HYE:PFI composite, isopropanol is added to the solution. PESA measurements are conducted on various films from different solutions, where the volume ratio of HYE and isopropanol is kept constant at 1:2 (v/v), while the volume ratio of HYE and PFI is varies (10:1, 10:2, 10:3, 10:4 (v/v)). The work functions increase from $\Phi = 4.7\,\text{eV}$ with HYE:PFI = 10:1 (v/v) to $\Phi = 5.3\,\text{eV}$ of HYE:PFI = 10:4 (v/v) (Figure 8.3), rendering these hybrids well suitable to be used as anode without the need for an additional HIL. The corresponding OLEDs are fabricated and the characteristics are depicted in Figure 8.4.
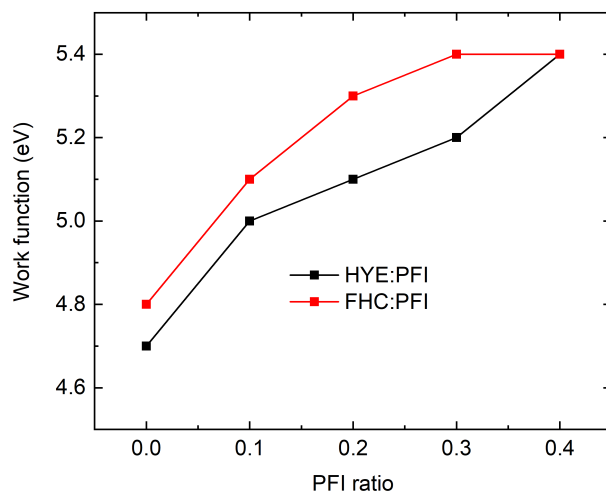
Figure 8.3: The work functions of HYE:PFI and FHC:PFI increases with increasing PFI concentration. The volume fraction of HYE and FHC changes from 10:0 to 10:4 (v/v), denoting the PFI ratio changes from 0 to 0.4.
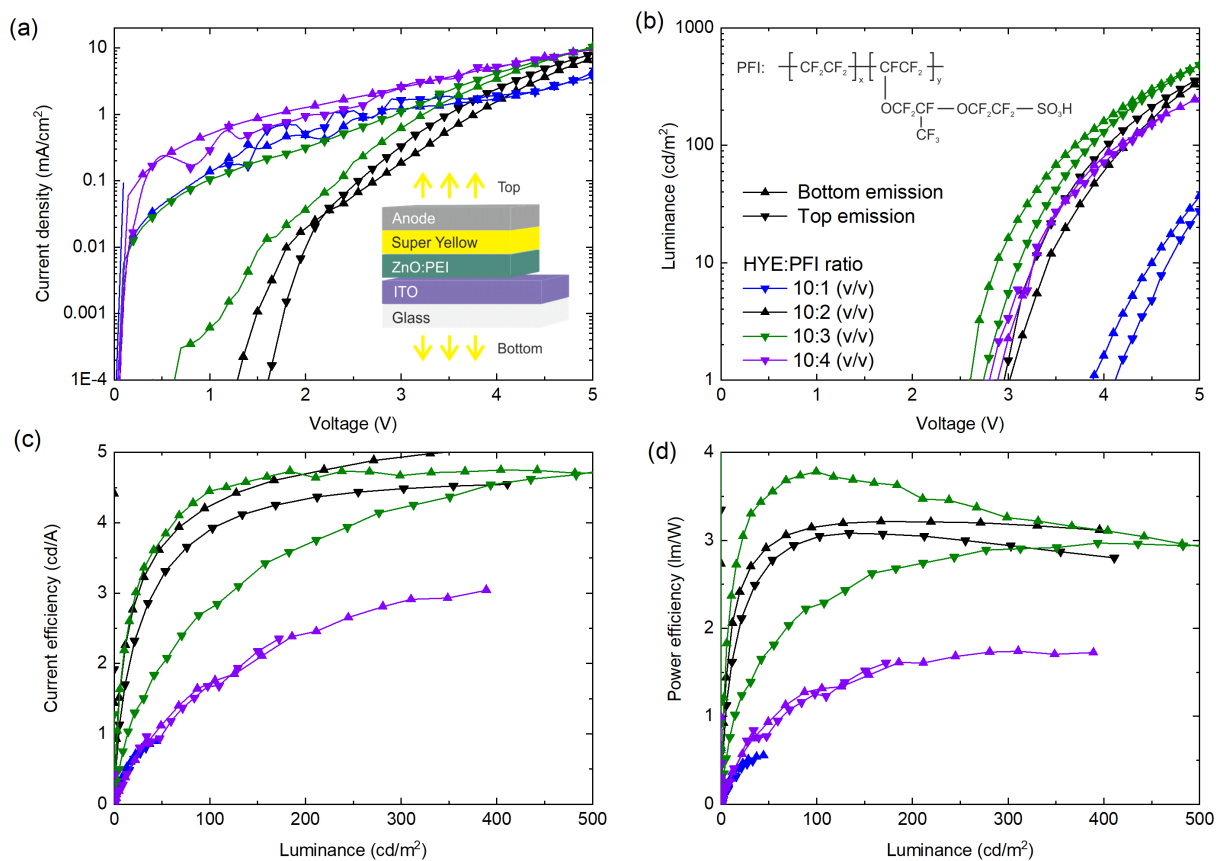
Figure 8.4: (a) J-V curves of inverted OLEDs incorporating HYE:PFI as top electrode. The ratio of HYE and PFI changes from 10:1 (v/v) to 10:4 (v/v). Inset: device architecture. As both electrodes are transparent, the emission is detected from both top and bottom directions. (b) V-L curves, where the onset voltage values of the devices at $1\,\mathrm{cd/cm^2}$ are implied. Inset: Molecular structure of PFI. (c) Current efficiency versus luminance. (d) Power efficiency versus luminance.

Since both electrodes of the OLEDs are transparent, photon emission occurs towards both bottom and top direction. The bottom emissions from the OLEDs are firstly measured, then the substrates are rotated for the second measurement to determine the top emission. The corresponding bottom and top luminances are calculated separately. Compared to the OLEDs with pure HYE as electrodes, where $V_{on} = 6.6\,V$, all devices comprising HYE:PFI electrodes exhibit lower onset voltage ($V_{on} = 2.6 - 4.1\,V$) due to the presence of PFI which in turn increases the anode's work function and facilitates hole injection. As observed in the J-V curves, all OLEDs experience unexpected high current at voltage below $2\,V$, except the OLEDs with HYE:PFI = 10:2 (v/v) which achieve an onset voltage of $V_{on} = 3\,V$. The onset voltage is comparable to the reference device with a VPAI 4083/Ag electrode ($V_{on} = 2.9\,V$). The current efficiencies based on bottom and top emission can reach up to $\eta_{c,bottom} = \eta_{c,top} = 4.5\,cd/A$ at $500\,cd/cm^2$. Thus, the current efficiency combining the light from both directions is roughly $\eta_{c,total} = 9\,cd/A$ at $1000\,cd/cm^2$. The total power efficiency considering both bottm and top emission is $\eta_{p,total} = 6\,lm/W$. Although more PFI tends to produce higher work function, the deposited films become less homogeneous towards increasing PFI concentration, which in turn reduces the device performance.

In fact, identical J-V curves are expected regardless whether the measurement is conducted from the bottom or top direction. But the two measurements are conducted sequentially. Hence, if the two J-V curves differ after rotating the device, this must be caused by the unstable device properties. Figure 8.5 shows the picture of one working OLED pixel and a microscope image of HYE:PFI electrode atop Super Yellow. Although the OLED pixel appears homogeneous at $4\,V$, the microscope image reveals the inhomogeneity of the anode caused by the agglomeration of AgNWs in HYE. The left side of Figure 8.5b shows the top electrode obtained from isopropanol solution atop Super Yellow, while, at the right side, the layer is removed by using dicing tape, leaving the Super Yellow film unscathed. The randomly distributed AgNWs agglomerates are likely to cause an inhomogeneous interface between the anode and Super Yellow, which may result in unevenly distributed thermal stress over the entire light emitting area during device operation, leading to fast degradation of the OLED pixel.

To overcome this issue, another highly conductive PEDOT:PSS (Clevios FHC Solar, henceforth referred to as "FHC") without any AgNW is investigated as replacement for HYE. The work function $\Phi = 4.8\,eV$ of pure FHC is measured with PESA which is similar to HYE. Again, isopropanol is added to the FHC:PFI solution to achieve better adhesion on Super Yellow, and the ratio between FHC and isopropanol is kept at 1:2 (v/v). By blending FHC and PFI at different volume ratios of 10:1, 10:2, 10:3, 10:4 (v/v), the work function of the film increases from $\Phi = 5.1\,eV$ to $\Phi = 5.4\,eV$ (Figure 8.3), proving the principle usability of FHC:PFI film as anode. Increasing the PFI concentration results in a
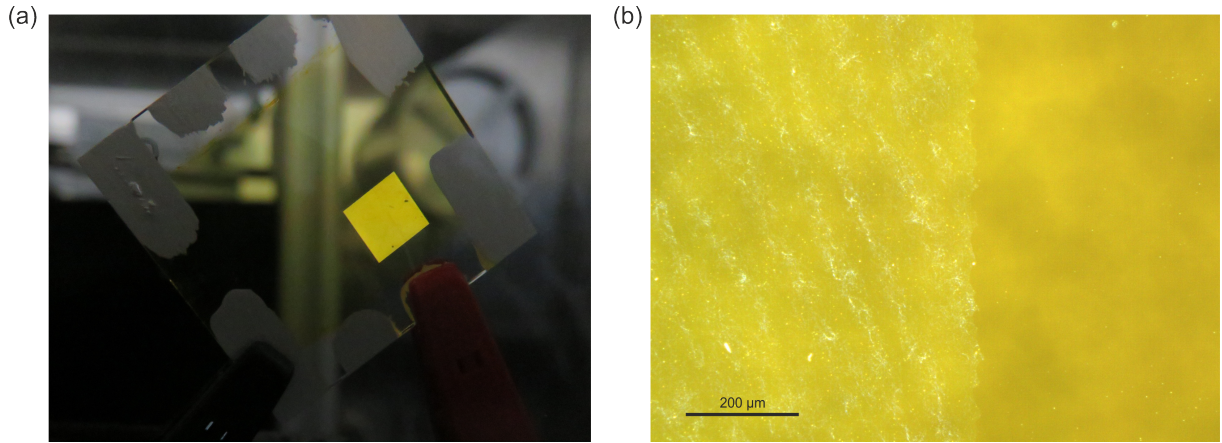
Figure 8.5: (a) Photo of a Representative OLED with HYE:PFI anode, operated at 4 V. The photo shows the emission from top direction. The device is transparent when it is switched off. (b) Microscope picture of a HYE:PFI film atop Super Yellow layer. The right part of the layer is removed with dicing tape, leaving Super Yellow undamaged.

higher work function of the mixed layer. However, when the volume ratio of PFI and FHC is beyond 4:10 (v/v), inhomogeneous films form. The corresponding OLEDs comprising electrodes with various FHC:PFI compositions are fabricated. As reference, the OLEDs with VPAI 4083 inserted between emitter and neat FHC anode are also produced. All the measurement results are plotted in Figure 8.6.

Since all J-V curves in Figure 8.6a are identical regardless of the device orientation, the devices seem to exhibit improved stability compared to OLEDs with HYE:PFI. The onset voltage of OLEDs with neat FHC anode (FHC:PFI = 10:0 (v/v)) is the highest ($V_{on} = 3.4$ V) among all OLEDs, caused by its intrinsic low work function. The current efficiency and power efficiency calculated from bottom luminance are $\eta_c = 2.5$ cd/A and $\eta_p = 1.5$ lm/W at 100 cd/m^2. By introducing VPAI 4083 layer between Super Yellow and FHC, the onset voltage decreases to $V_{on} = 2.9$ V. Both the current and power efficiencies based on bottom emission are improved to $\eta_c = 4$ cd/A and $\eta_p = 2.6$ lm/W at 100 cd/m^2. With an increasing concentration of PFI in the composite, from FHC:PFI = 10:1 (v/v) to FHC:PFI = 10:4 (v/v), the onset voltage remains constant at $V_{on} = 2.5$ V. The best performance ($\eta_c = 6$ cd/A and $\eta_p = 4.5$ lm/W at 100 cd/m^2) is accomplished with FHC:PFI = 10:4 (v/v) (red curves). A further increase of the PFI concentration leads to inhomogeneous layers that are not completely closed. Thus they are not investigated in OLEDs.

The emissions from both top and bottom directions are measured, and the electrical properties (J-V curves) of the OLED are not damaged after one measurement. The combination of both top and bottom luminances can be considered as the total luminance of the transparent OLED. The calculated combination of the optimal OLEDs with FHC:PFI = 10:4 (v/v) are plotted together with the curves based on top and
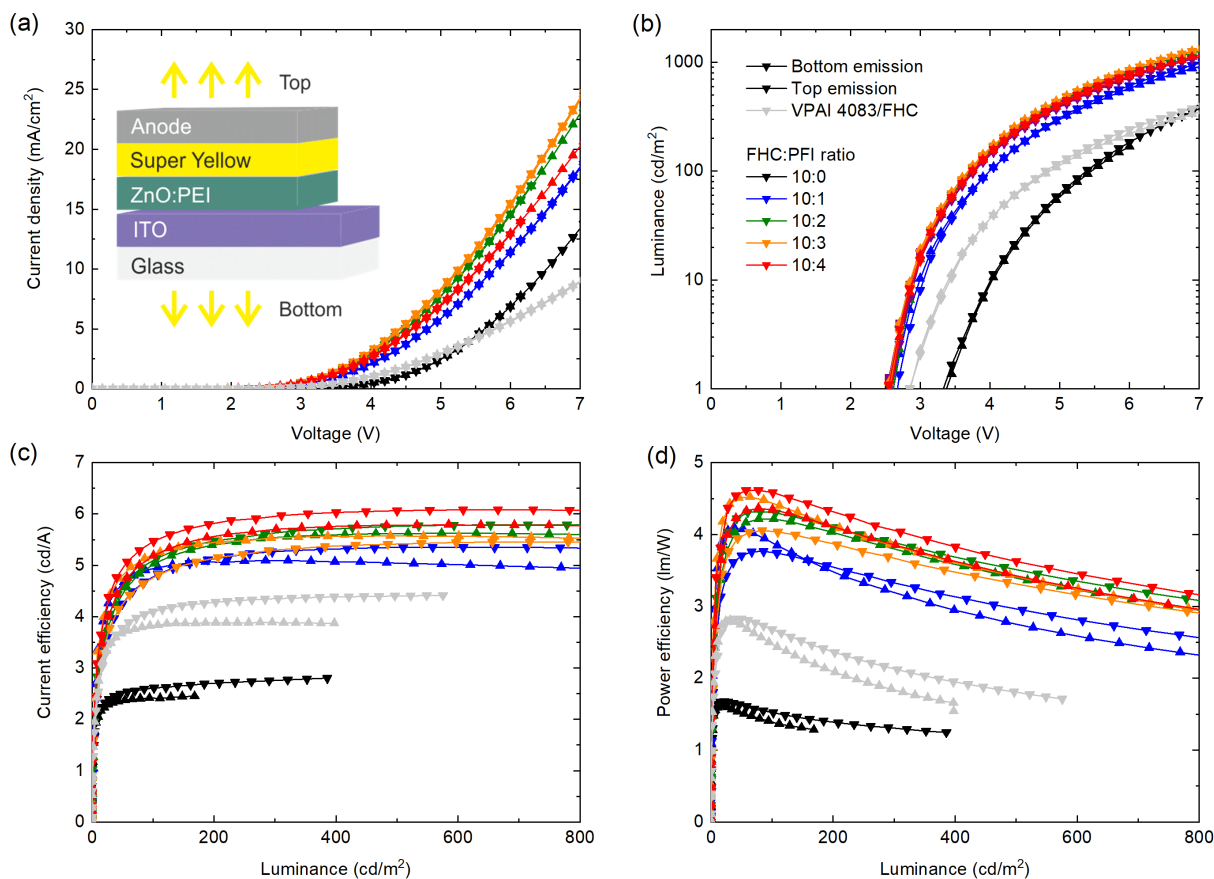
Figure 8.6: (a) J-V curves of transparent OLEDs employing the VPAI 4083/FHC bilayer or a single FHC:PFI layer to inject holes. The ratio between FHC and PFI is variated according to the legend in (b). Inset: device architecture. Light emission from both bottom and top directions are measured. (b) V-L curves, where the onset voltage values of the devices at $1\,\mathrm{cd/cm^2}$ are also indicated. (c) Current efficiency versus luminance. (d) Power efficiency versus luminance.
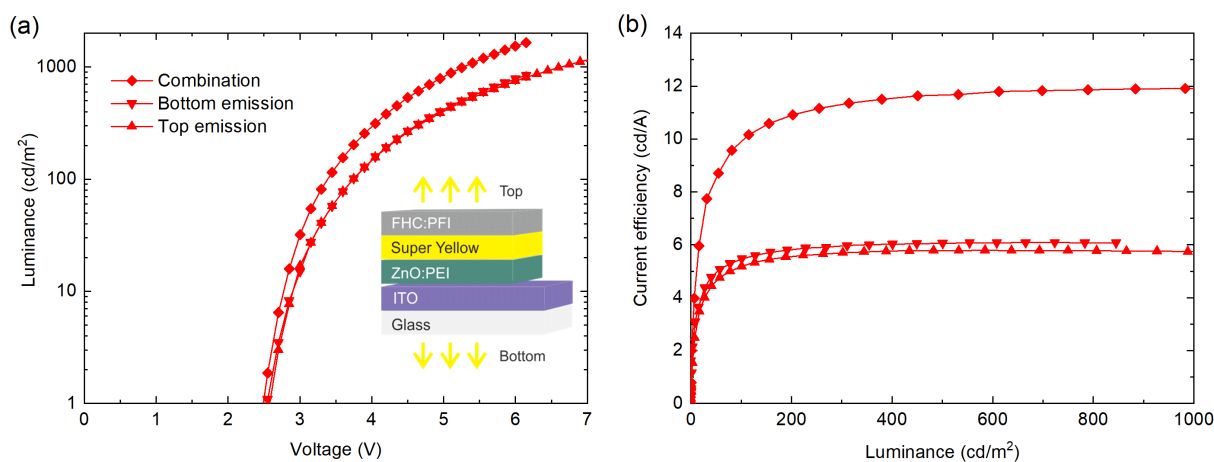
Figure 8.7: (a) L-V curves of the OLED with FHC:PFI = 10:4 (v/v) as top electrode. The total luminance (diamond) is calculated by adding the emissions from both bottom (down-triangle) and top (up-triangle) directions at the same current. (b) After combining the luminances from both top and bottom directions, the current efficiency of the transparent OLED is approximately $\eta_\mathrm{c} = 12\,\mathrm{cd/A}$ at $1000\,\mathrm{cd/m^2}$.

(a)

(b)

10 µm

282 µm

200 µm

500 µm
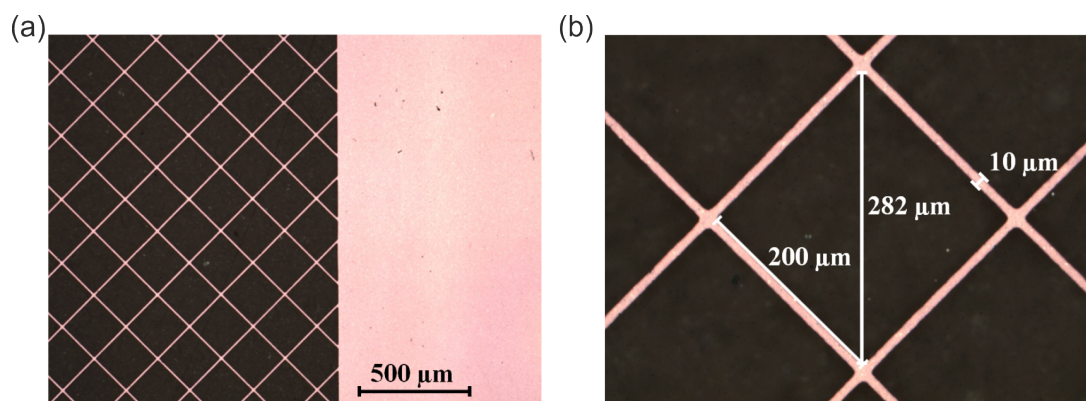
Figure 8.8: Optical microscope images of the pre-patterned silver mesh on flexible PET substrate with (a) 153 and (b) 736 times magnification.

bottom luminances in Figure 8.7. The onset voltage of the transparent OLED is only $V_{on} = 2.5\,V$ and the calculated total current efficiency is $\eta_c = 12\,cd/A$ at $1000\,cd/m^2$. The performance is comparable to the opaque OLED with evaporated silver top electrode ($V_{on} = 2.9\,V$, $\eta_c = 12.5\,cd/A$). Thus it can be concluded that the FHC:PFI anode leads to decent OLED performance. Since only one annealing step at $100\,°C$ is required, this process is also compatible with plastic substrates.

8.1.2 All-solution Processed Transparent Flexible OLEDs

After successfully demonstrating a FHC:PFI top electrode for transparent OLEDs, a bottom electrode atop a flexible substrate is required to replace the ITO coated glass substrate. Czolk et al. reported flexible solar cells with a commercially available PET substrate, on which the pre-patterned, micro silver mesh (PolyTC, PolyIC GmbH & Co. KG) is printed. The sheet resistance of the silver mesh on PET (AgPET) is $R_\square = 16\,\Omega$, which is similar to the resistance of ITO on glass. Two optical microscope photos of the AgPET are shown in Figure 8.8. The $10\,µm$ wide and $40\,nm$ thick silver lines with diagonal spacing of $282\,µm$ are almost invisible (Figure 8.8b). In order to fill the voids between the silver mesh to prevent short circuit, a layer of FHC is deposited on top. Then all-solution processed transparent OLEDs are fabricated onto the flexible AgPET substrates using the layout described in Chapter 4.2.

The OLED architecture and characteristics are depicted in Figure 8.9. The light emissions from both bottom and top sides are measured, and the data is used for calculating the total performance. The onset voltage of the OLED is $V_{on} = 2.7\,V$, indicating efficient charge carrier injection. The calculated total current efficiency is roughly $\eta_c = 9\,cd/A$ at $2500\,cd/m^2$, while the power efficiency is around $\eta_p = 4.5\,lm/W$. The flexible OLED performance is inferior to the rigid OLED performance. Yet plastic substrates allow for bending and folding of the devices as the transparent OLED pixel on the AgPET
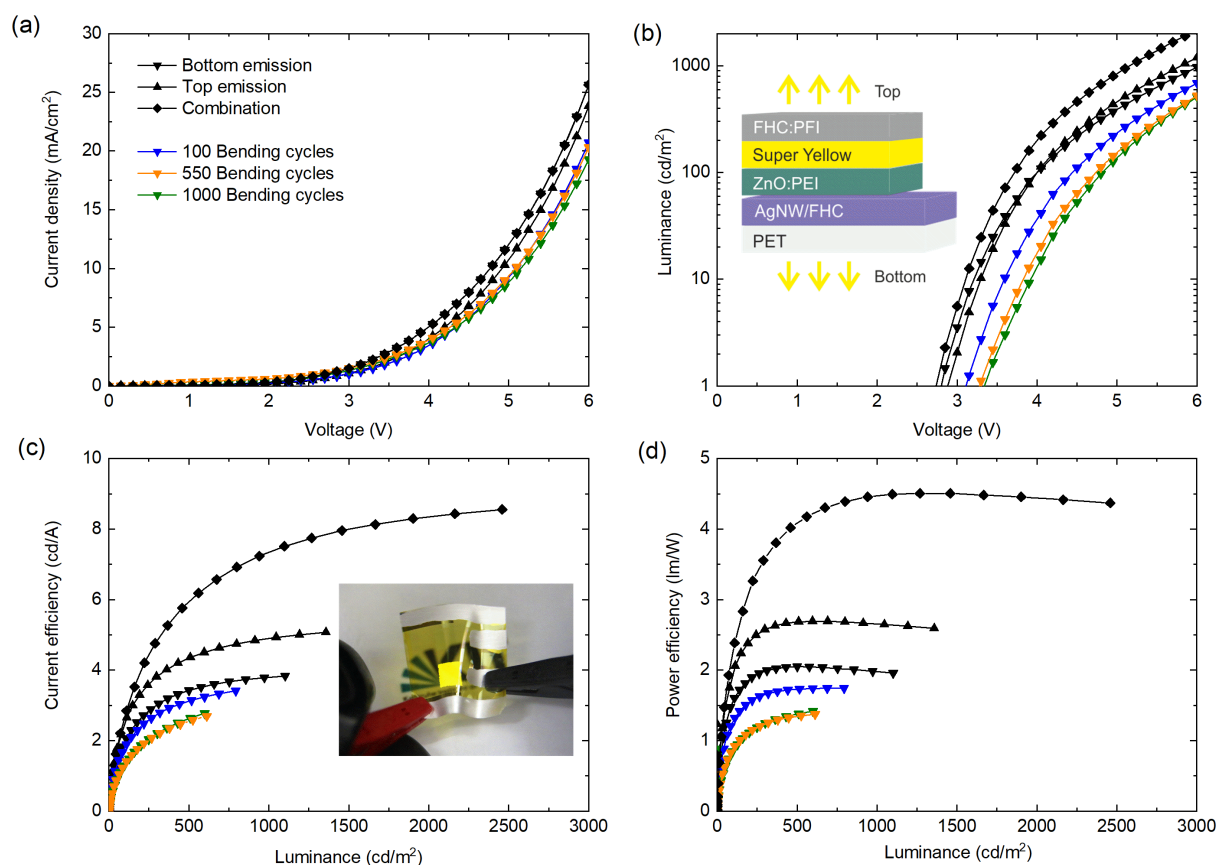
Figure 8.9: Characteristics of the all-solution processed transparent OLEDs on AgPET substrates. The emissions are measured from both top (up-triangle) and bottom (down-triangle) directions, and the total emission (diamond) is calculated. Mechanical bending tests are conducted. The device properties are recorded after 100, 550 and 1000 cycles of bending. (a) J-V curves. (b) L-V curves. (c) Current efficiency versus luminance. Inset: a photo of an OLED pixel driven at 3 V. (d) Power efficiency versus luminance.

substrate in Figure 8.9c (inset). Additional bending experiments are conducted to test the robustness of the flexible OLEDs. During the bending tests, the devices are bent manually over a rod with a bending radius $r_b = 1.7$ mm and released thereafter. The luminance in bottom direction is recorded after 100, 550 and 1000 cycles of bending. After 100 cycles of bending, less current is injected at the same voltage, and the onset voltage increases, leading to decreased efficiencies. More obvious damages, i.e. higher onset voltages and lower efficiencies are observed in the first 550 bending cycles. Afterwards the OLEDs are not influenced by bending anymore. Even after 1000 bending cycles, the OLEDs still yield a power efficiency of 67% of its initial value, verifying the OLEDs' mechanical robustness.

8.2 OLEDs with ZrO$_2$:PEI Composite

The use of ZnO:PEI has been successfully demonstrated in transparent OLEDs. To confirm the universality of generating low work function electron injection layers by adding
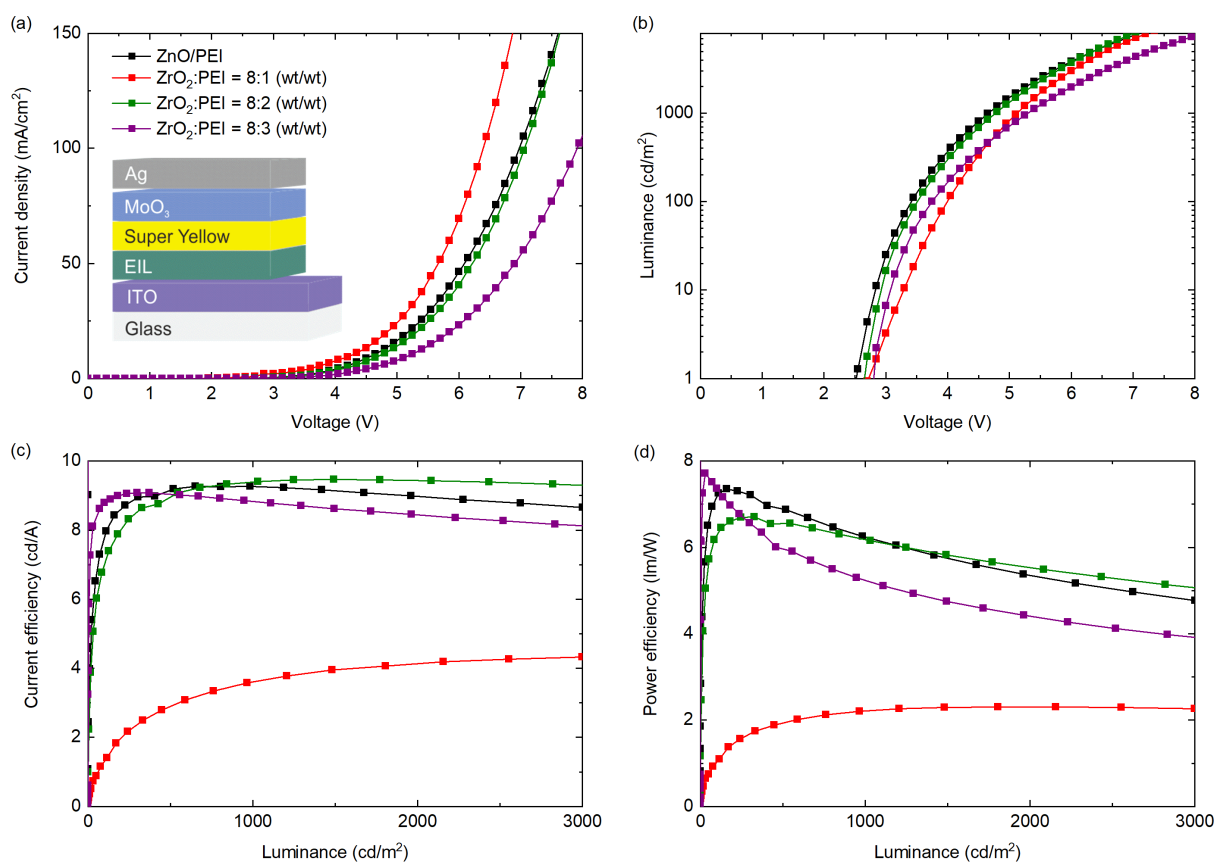
Figure 8.10: (a) J-V curves of inverted OLEDs incorporating either ZnO/PEI bilayers as reference or the mixture ZrO$_2$:PEI as EIL. Inset: OLED architecture. The weight ratio of ZrO$_2$ and PEI changes from 8:1 (wt/wt) to 8:3 (wt/wt). (b) L-V curves. (c) Current efficiency versus luminance. (d) Power efficiency versus luminance.

PEI to metal oxide, another metal oxide ZrO$_2$ is optimized and investigated in both inverted and regular architectures.

First, ZrO$_2$:PEI is incorporated into the standard inverted OLED architecture (Figure 8.10a inset). The ZnO/PEI bilayer is employed as reference, and EILs comprising different ZrO$_2$ to PEI ratios are investigated. The ZrO$_2$:PEI layers are achieved from a filtered solution (PTFE, 0.2 µm), which is formed by blending ZrO$_2$ nanoparticles dispersions (1 wt.% in isopropanol, Avantama AG) with PEI solution (1 mg/mL, 2 mg/mL or 3 mg/mL, 1-propanol). The corresponding characteristics are summarized in Figure 8.10.

The OLEDs with EILs comprising ZrO$_2$:PEI mixtures exhibit similar low onset voltages ($V_{on} = 2.5 - 2.7$ V) as the reference devices with ZnO/PEI bilayers ($V_{on} = 2.5$ V at 1 cd/m^2), hinting at efficient electron injection. The best device performances are archived if the weight ratio of ZrO$_2$ and PEI is 8:2 (wt/wt). They are almost identical in all aspects, including J-V curves, onset voltage ($V_{on} = 2.5$ V), current efficiency ($\eta_c = 9$ cd/A at 1000 cd/m^2) and power efficiency ($\eta_p = 6.5$ lm/W at 1000 cd/m^2). In addition, the work function ($\Phi = 3.5$ eV) of ZrO$_2$:PEI layers (8:2 wt/wt) is similar to ZnO/PEI. Its

(a)

41.6 nm

1.0 µm

(b)

60.8 nm

2.0 µm
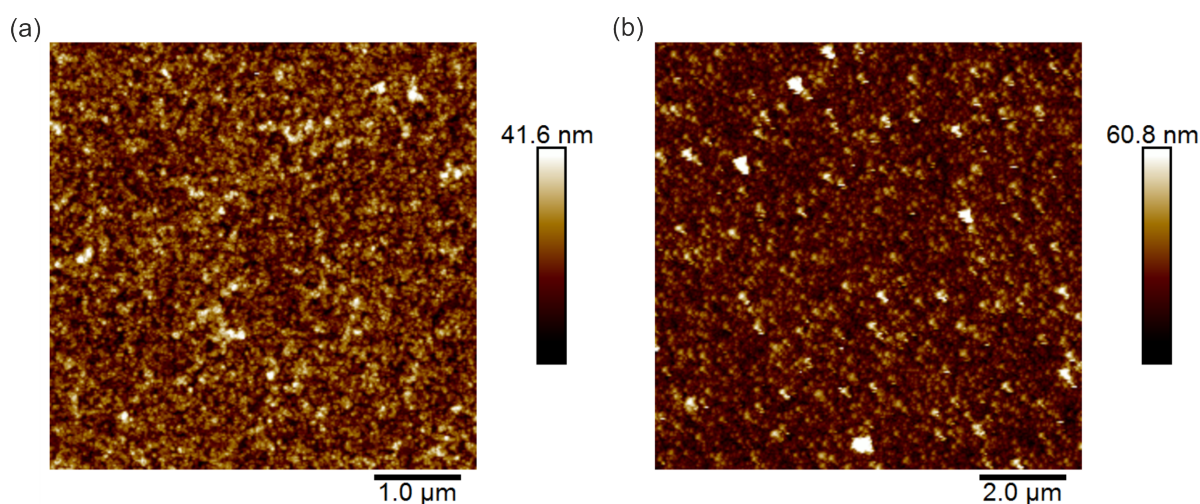
Figure 8.11: AFM image of a mixed EIL comprising (a) ZnO and PEI, (b) ZrO_2 and PEI with a weight ratio of 8:2 (wt/wt) on top of the ITO electrode. The ZrO_2:PEI film exhibits a mean root square roughness of $R_q = 8\,nm$, while the ZnO:PEI film show a roughness of $R_q = 6\,nm$.

homogeneity is confirmed by the AFM image shown in Figure 8.11b. For comparison, the AFM image of a ZnO:PEI film is also shown. The root mean square roughness of the ZrO_2:PEI film ($R_q = 8\,nm$) is slightly higher than the roughness of ZnO:PEI film ($R_q = 6\,nm$).

Its electron injection ability is verified in the inverted OLED layout, but solution deposited regular OLEDs with the architecture shown in Figure 8.12a inset become also feasible. VPAI 4083 is applied as HIL and Super Yellow is employed as emitter. The measured characteristics are illustrated in Figure 8.12.

Notably, once again, the excellent electron injection ability of ZrO_2:PEI is confirmed by the identical onset voltage compared to the reference ($V_{on} = 2.2\,V$). Among all the various weight ratios of ZrO_2 and PEI, the best device performances are still accomplished at a ZrO_2:PEI ratio of 8:2 (wt/wt). At $1000\,cd/m^2$, a high current efficiency of $\eta_c = 12\,cd/A$ and a power efficiency of $\eta_p = 11\,lm/W$ are obtained in OLEDs with solution processed EILs, which are also comparable to the reference with evaporated LiF ($\eta_c = 12\,cd/A$, $\eta_p = 12.5\,lm/W$). Accordingly, with a low work function of $\Phi = 3.5\,eV$, the solution processable electron injection layer comprising ZrO_2 nanoparticle dispersions and PEI solutions is suitable for both regular and inverted OLED architectures with Super Yellow as the emission layer.

Experimental: The KPFM measurements use HOPG as reference. All OLEDs are characterized in the integrating sphere setup. All electron injection layers are obtained by spincoating the solutions atop ITO (4000rpm, 30 s), followed by annealing ($100\,°C$,
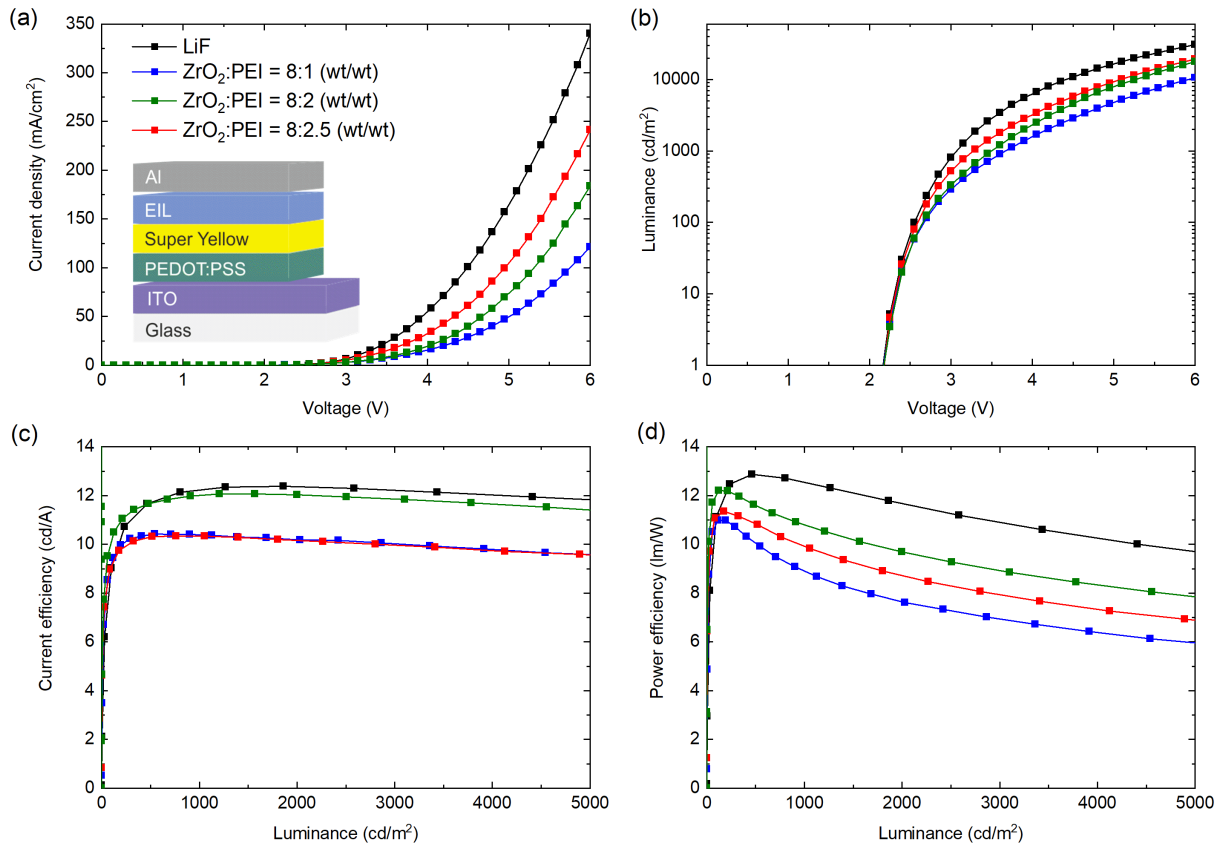
Figure 8.12: (a) J-V curves of regular OLEDs incorporating either evaporated LiF for reference or the mixture of ZrO$_2$ and PEI. Inset: regular OLED architecture. The weight ratio of ZrO$_2$ and PEI changes from 8:1 (wt/wt) to 8:2.5 (wt/wt). (b) V-L curves. (c) Current efficiencies at various luminances. (d) Power efficiency versus luminance.

10 min). As the emission layer, a 70 nm-thick Super Yellow layer is coated (1000 rpm, 45 s; 4000 rpm, 3 s) and then annealed (80 °C, 10 min).

To fabricate the top electrode of the inverted devices, 10 nm MoO$_3$ and 100 nm Ag are vacuum deposited. Afterwards, the MoO$_3$ is replaced by VPAI 4083, which is diluted in methanol and isopropanol with a volume ratio of 1:1:4 (v/v/v), then spin cast (4000 rpm, 30 s) and annealed (100 °C, 10 min). In the transparent devices, the top electrode solutions are spin cast (1000 rpm, 45 s), followed by an annealing step at 100 °C for 10 min. For the fabrication of the bottom electrode of the flexible OLEDs, FHC is mixed with isopropanol and water at a volume ratio of 1:1:1.5 (v/v/v) before spincoating (1000 rpm, 60 s) and annealing (100 °C, 30 min). For the fabrication of the regular OLED architecture, VPAI 4083 is diluted with ethanol (1:3 (v/v)), spincoated (500rpm, 3 s; 4000 rpm, 25 s) and annealed (100 °C, 10 min) to achieve a 25 nm-thick layer. 1 nm LiF is vacuum deposited for reference. Finally, the top electrode (200 nm aluminum) is vacuum deposited onto all regular devices.

9 Conclusions and Outlook

This thesis focused on the development of efficient solution processed electron injection layers for advanced OLED architectures incorporating various emission layers. Most importantly, in order to facilitate electron injection into the emission layer, the electron injection material should exhibit a low work function. Thus approaches to produce low work function EILs are proposed. These novel electron injection materials enable advanced architectures, such as tandem OLEDs, and facile but efficient all-solution processed, mechanically flexible OLEDs.

Most commercially used OLED emitters are either fluorescent or phosphorescent, whereas thermally activated delayed fluorescent emitters are still being researched. The quantum efficiency of fluorescent emitters is intrinsically limited because the triplet excitons are not exploited. Phosphorescent emitters with heavy metal elements can utilize both singlet and triplet excitons, however, their material costs are rather high. In Chapter 5, third generation OLEDs with TADF emitters are deposited from solutions. Two different types of TADF emitters are investigated. One of them is a blue-emitting pure organic TADF emitter Tetrazole-xy. It is incorporated into a regular OLED architecture, with the HIL and the emission layer spincoated from solution, while the electron transport layer and the cathode are evaporated. Various hosts for the emitter are investigated, neat mCP, neat 26DCzppy or a mixture of mCP and 26DCzppy. The best device performance with a low onset voltage of $V_{on} = 3\,V$ and a high EQE of 10% are achieved with the mixed host. This EQE is beyond the theoretical limit of traditional fluorescent OLEDs. The other solution deposited TADF emitter is a green-emitting copper(I) complex which is formed from CuI and MePyrPHOS. It is initially integrated into OLED arrays with changing emission layer thicknesses to determine the optimal layer thickness. Then the OLEDs with five solution processed functional layers are fabricated, where the electron injection layer consists of a ZrO_2:Y/PEI bilayer with a low work function of $\Phi = 3.5\,eV$. Because of efficient charge carrier injections, the OLEDs showed a low onset voltage of $V_{on} = 3\,V$ and a high current efficiency of $\eta_c = 20\,cd/A$ at $1000\,cd/m^2$.

In order to prolong the lifetime of OLEDs, it is essential to reduce the operating current while maintaining the luminance. One approach to address the lifetime issue is to fabricate tandem OLEDs. The electron injection layer (ZrO_2:Y/PEI) proposed in Chapter 5 enables both regular and inverted tandem architectures because ZrO_2:Y

is stable in acidic environment, i.e. in PEDOT:PSS. Chapter 6 presents a universal charge generation layer for highly efficient tandem OLEDs fabricated from solution. This CGL consists of four layers WO_3/PEDOT:PSS/ZrO_2:Y/PEI, allowing for both inverted and regular tandem OLED architectures, where a fluorescent polymer (Super Yellow), a phosphorescent small molecule (SM-green-A) or a TADF copper(I) complex (CuI:MePyrPHOS) is employed as emitter. In addition, the hole blocking material TPBi or the electron blocking material mCP is employed in regular or inverted tandem architectures, respectively. Altogether up to 11 functional layers are sequentially processed from solutions in the tandem architecture. The tandem OLEDs require only half of the current of the single devices to achieve the same luminance, although the onset voltages of the tandem OLEDs are twice the onset voltages of the single references. For example, the onset voltage of the single junction OLEDs with SM-green-A emitter is $V_{on,single} = 3.1\,V$, while in the tandem OLEDs that value doubles ($V_{on,tandem} = 6.2\,V$). The single-junction references reach up to a current efficiency of $\eta_{c,single} = 92\,cd/A$ at $500\,cd/m^2$. Accordingly, the current efficiency of the tandem devices is $\eta_{c,tandem} = 184\,cd/A$ at $1000\,cd/m^2$. Additional lifetime measurements are conducted on the phosphorescent OLEDs. Starting with the same initial luminance of $1000\,cd/m^2$, the tandem OLEDs show remarkable lifetime ($LT_{80} = 1700\,h$), outperforming the single OLED references ($LT_{80} = 150\,h$).

Advanced tandem OLEDs with up to 11 layers processed from solutions are developed by incorporating ZrO_2:Y/PEI. Yet, the deposition of this EIL combines a metal oxide and an ultra-thin PEI layer, which is quite difficult to integrate into the future roll-to-roll printing. Thus a simplified electron injection layer is demonstrated in Chapter 7. This single EIL is obtained by adding cesium fluoride into ZnO which significantly reduces the work function of the EIL from $\Phi_{ZnO} = 3.9\,eV$ of pure ZnO to $\Phi_{ZnO:CsF} = 3.1\,eV$ of the composite. Due to the low work function of this EIL, inverted OLEDs incorporating the commercially available fluorescent polymer Super Yellow exhibit excellent performance with a low onset voltage of $V_{on} = 2.6\,V$ and a high current efficiency of $\eta_c = 17\,cd/A$ at $3000\,cd/m^2$. In addition to fluorescent OLEDs, phosphorescent OLEDs are fabricated by comprising a red-emitting small molecule $Ir(MDQ)_2(acac)$, where ZnO:CsF mixture is applied as EIL. The devices show a rather high current efficiency of $\eta_c = 17\,cd/A$ at $6000\,cd/m^2$. This method to generate low work function EIL by blending CsF into metal oxide is not only designed for ZnO, it is further confirmed by employing another metal oxide ZrO_2 and ZrO_2:Y. By introducing CsF, the work function $\Phi_{ZrO_2} = 4\,eV$ of ZrO_2 is effectively decreased to $\Phi_{ZrO_2:CsF} = 3.2\,eV$. Likewise, the work function of the composite of ZrO_2:Y and CsF is $\Phi_{ZrO_2:Y:CsF} = 3.2\,eV$, while the neat ZrO_2:Y film exhibits a high work function of $\Phi_{ZrO_2:Y} = 4.1\,eV$. By incorporating these two mixtures as EIL, the Super

Yellow OLEDs show an extremely low onset voltage of $V_{on} = 2.2\,V$ and a high current efficiency of about $\eta_c = 20\,cd/A$.

Although blending CsF into metal oxides can produce low work function EILs, CsF is not stable in air. Consequently in Chapter 8, another simple approach is illustrated to result in low work function EIL, where ZnO, is mixed with PEI. The work function of ZnO:PEI is only $\Phi_{ZnO:PEI} = 3.4\,eV$, which is identical to the ZnO/PEI bilayer. Besides the incorporation in the opaque OLEDs, it is also used in transparent OLEDs which have the potentials to be embedded into windows or transparent displays. In the transparent OLEDs, a high work function anode ($\Phi = 5.4\,eV$) is incorporated by adding PFI into a highly conductive PEDOT:PSS (FHC Solar). Thus the hole injection layer is omitted. Accordingly, this simplified transparent OLED architecture consists of only 4 layers, including the cathode (ITO), the EIL (ZnO:PEI), the emission layer (Super Yellow) and the anode (FHC Solar:PFI). By taking account of the light emissions from both bottom and top sides of the transparent OLED, the devices show a low onset voltage of $V_{on} = 2.5\,V$ and a high current efficiency $\eta_c = 12\,cd/A$ which are similar to the reference opaque OLEDs with additional HILs. Moreover, all-solution processed OLEDs are realized by replacing the ITO coated glass substrates with PEDOT:PSS (FHC Solar) atop AgPET substrates. The flexible OLEDs show a low onset voltage of $V_{on} = 2.7\,V$ and a current efficiency of $\eta_c = 9\,cd/A$. In addition to ZnO, PEI is also mixed with ZrO_2 to produce an efficient EIL with a work function of $\Phi_{ZrO_2:PEI} = 3.5\,eV$. This low work function EIL is further demonstrated in both regular and inverted OLED architectures.

In the future, the simplified EILs and solution processable electrodes can be incorporated into the tandem architecture, further enabling all-solution processed OLEDs exhibiting long lifetime. In addition to tandem OLEDs where both emission layers are identical, two emission layers with complementary colors can be incorporated to realize white-emitting tandem OLEDs. By introducing another light emitting unit to the tandem architecture, triple-OLEDs with three layers emitting in primary colors (red, green, blue) can be further developed. Each sub-OLED can be adjusted and optimized separately to achieve a white appearance with high color rendering index. The transmittance of investigated transparent OLEDs is limited by the emission layer. Thus, if the yellow-emitting polymer is replaced by other emitting materials with large optical band gaps, the OLEDs can, therefore, achieve higher transparency.

A Work Function Overview of the Electron Injection Layers

Material	Work function (eV)
ZnO	3.9
ZnO/PEI	3.4
ZnO:CsF	3.1
ZnO:PEI	3.4
ZrO_2	4.1
ZrO_2:CsF	3.2
ZrO_2:PEI	3.5
ZrO_2:Y	4.1
ZrO_2:Y/PEI	3.5
ZrO_2:Y:CsF	3.2

B Acronyms

AFM	atomic force microscopy
AgNW	silver nanowire
AMOLED	active matrix organic light emitting diode
CGL	charge generation layer
CIE	Comission internationale de l'Eclairage
CPD	contact potential difference
CT	charge transfer
DOS	density of state
EBL	electron blocking layer
EIL	electron injection layer
EML	emission layer
EQE	external quantum efficiency
ETL	electron transport layer
FN	Fowler-Nordheim
HBL	hole blocking layer
H-dipping	horizontal dipping
HIL	hole injection layer
HOMO	highest occupied molecular orbital
HOPG	highly oriented pyrolytic graphite
HTL	hole transport layer
IC	internal conversion
IOLED	inverted organic light emitting diode
IQE	internal quantum efficiency
ISC	internal system crossing
KPFM	Kelvin probe force microscope
LCD	liquid crystal display
LTI	Light Technology Institute
LUMO	lowest unoccupied orbital
MO	molecular orbital
MZE	Material Research Center for Energy Systems

OCS	optoelectronic characterization setup
OFET	organic field effect transistor
OLED	organic light emitting diode
OPAMP	operational amplifier
PESA	photoelectron spectroscopy in air
PLQY	photoluminescence quantum yield
RISC	reverse intersystem crossing
SMU	source measurement unit
SP	surface plasma
SPA	singlet–polaron annihilation
SSA	singlet–singlet annihilation
STA	singlet–triplet annihilation
TADF	thermally activated delayed fluorescent
TPA	triplet–polaron annihilation
TTA	triplet–triplet annihilation
UV	ultraviolet

C Materials

26DCzppy	2,6-bis(3-(carbazol-9-yl)phenyl)pyridine
4CzIPN	2,4,5,6-tetra(carbazol-9-yl)-1,3-dicyanobenzene
Ag	silver
Al	aluminum
Alq_3	tris(8-hydroxyquinoline)aluminum
AZO	aluminum doped zinc oxide
B3PYMPM	bis-4,6-(3,5-di-3-pyridylphenyl)-2-methylpyrimidine
Ba	barium
BPhen	bathophenanthroline
Ca	calcium
CBP	4,4-bis(carbazol-9-yl)biphenyl
Cs	cesium
Cs_2CO_3	cesium carbonate
CsF	cesium fluoride
CuI	copper iodide
F_4TCNQ	2,3,5,6-tetrafluoro-7,7,8,8-tetracyanoquinodimethane
F8BT	poly(9,9-dioctylfluorene-alt-benzothiadiazole)
$FeCl_3$	iron(III) chloride
HOPG	highly oriented pyrolytic graphite
$Ir(MDQ)_2(acac)$	iridium-(III)bis (2-methyldibenzo-[f,h] quinoxaline) (acetylacetonate)
$Ir(ppy)_3$	tris[2-phenylpyridinato-C2,N]iridium(III)
ITO	indium tin oxide
Li	lithium
LiF	lithium fluoride
Liq	8-quinolinolato lithium
mCP	N,N-dicarbazoyl-3,5-benzene
MePyrPHOS	4-methyl-2-(diphenylphosphino)-pyridine
MoO_3	molybdenum oxide
O_2	oxygen

OXD-7	1,3-bis[2-(4-tert-butylphenyl)-1,3,4,-oxadiazo-5-yl]
PDMS	polydimethylsiloxane
PEDOT:PSS	poly(3,4-ethylenedioxythiophene):polystyrene sulfonate
PEI	polyethylenimine
PEIE	polyethylenimine ethoxylated
PET	polyethylene terephthalate
PFI	perfluorinated ionomoer
Pt	platinum
PVK	poly(N-vinylcarbazole)
SPS	sodium polysterene sulfonate
TAZ	3-phenyl-4-(1'-naphthyl)-5-phenyl-1,2,4-triazole
TCTA	tris(4-carbazoyl-9-ylphenyl)amine
Tetrazole-xy	3-(1-allyl-1H-tetrazole-5-yl)-2,4,5,6-tetra(carbazole-9-yl)benzonitrile
TPBi	2,2,2''-(1,3,5-benzinetriyl)-tris(1-phenyl-1-H-benzimidazole)
THF	tetrahydrofuran
TiO_2	titanium oxide
Ir	iridium
ITO	indium doped tin oxide
V_2O_5	vanadium oxide
WO_3	tungsten oxide
ZnO	zinc oxide
ZrO_2	zirconium oxide
ZrO_2:Y	yttrium doped zirconium oxide

Bibliography

[1] C. W. Tang and S. A. Vanslyke. Organic electroluminescent diodes. *Applied Physics Letters*, 51(12):913–915, 1987.

[2] AMOLED shipment revenue forecast, http://www.oled-info.com, October 2017.

[3] Foldable TV folds, can still TV afterward, https://www.insidehook.com/nation/lg-foldable-tv, January 2018.

[4] LG OLED light, http://www.lgoledlight.com, October 2017.

[5] L. S. Liao, K. P. Klubek, and C. W. Tang. High-efficiency tandem organic light-emitting diodes. *Applied Physics Letters*, 84(2):167–169, 2004.

[6] H. Kanno, R.J. Holmes, Y. Sun, S. Kena-Cohen, and S.R. Forrest. White stacked electrophosphorescent organic light-emitting devices employing MoO_3 as a charge-generation layer. *Advanced Materials*, 18(3):339–342, 2006.

[7] A. Köhler and H. Bässler. *Electronic processes in organic semiconductors*. Wiley-VCH Verlag GmbH & Co. KGaA, 2015.

[8] M. B. Smith and J. March. *March's advanced organic chemistry*. John Wiley & Sons, Inc., 2006.

[9] W. Brütting. *Physics of organic semiconductors*. Wiley-VCH Verlag GmbH & Co. KGaA, 2006.

[10] S. S. Deshpande. Principles and applications of luminescence spectroscopy. 41(3): 155–224, 2010.

[11] M. A. Baldo, M. E. Thompson, and S. R. Forrest. Phosphorescent materials for application to organic light emitting devices. *Pure and Applied Chemistry*, 71(11): 2095–2106, 1999.

[12] M. Schwoerer and H. C. Wolf. *Organic molecular solids*. Wiley-VCH Verlag GmbH, 2008.

[13] M. Pope and C.E. Swenberg. *Electronic processes in organic crystals and polymers.* Clarendon Press, 1982.

[14] G. Odian. *Principles of polymerization.* John Wiley & Sons, Inc.

[15] S.-S. Sun and L. R. Dalton. *Introduction to organic electronic and optoelectronic materials and devices (optical science and engineering series).* CRC Press, Inc., 2008.

[16] B. Choudhury. *Organic light emitting devices (OLEDs) and structurally integrated photoluminescence based chemical and biological sensors excited by OLEDs.* PhD thesis, Iowa State University, 2005.

[17] C.G. Granqvist and A. Hultåker. Transparent and conducting ITO films: New developments and applications. *Thin Solid Films*, 411(1):1–5, 2002.

[18] S. Höfle, M. Pfaff, H. Do, C. Bernhard, D. Gerthsen, U. Lemmer, and A. Colsmann. Suppressing molecular aggregation in solution processed small molecule organic light emitting diodes. *Organic Electronics*, 15(1):337–341, 2014.

[19] B.W. D'Andrade, R.J. Holmes, and S.R. Forrest. Efficient organic electrophosphorescent white-light-emitting device with a triple doped emissive layer. *Advanced Materials*, 16(7):624–628, 2004.

[20] J. S. Kim, M. Granström, R. H. Friend, N. Johansson, W. R. Salaneck, R. Daik, W. J. Feast, and F. Cacialli. Indium–tin oxide treatments for single- and double-layer polymeric light-emitting diodes: The relation between the anode physical, chemical, and morphological properties and the device performance. *Journal of Applied Physics*, 84(12):6859–6870, 1998.

[21] D. J. Milliron, I. G. Hill, C. Shen, A. Kahn, and J. Schwartz. Surface oxidation activates indium tin oxide for hole injection. *Journal of Applied Physics*, 87(1): 572–576, 2000.

[22] S. Höfle, A. Schienle, M. Bruns, U. Lemmer, and A. Colsmann. Enhanced electron injection into inverted polymer light-emitting diodes by combined solution-processed zinc oxide/polyethylenimine interlayers. *Advanced Materials*, 26(17):2750–2754, 2014.

[23] J. Meyer, P. Görrn, S. Hamwi, H.-H. Johannes, T. Riedl, and W. Kowalsky. Indium-free transparent organic light emitting diodes with Al doped ZnO electrodes grown by atomic layer and pulsed laser deposition. *Applied Physics Letters*, 93(7):073308, 2008.

[24] A. Kumar and C. Zhou. The race to replace tin-doped indium oxide: Which material will win? *ACS Nano*, 4(1):11–14, 2010.

[25] Z. Yu, L. Hu, Z. Liu, M. Sun, M. Wang, G. Grüner, and Q. Pei. Fully bendable polymer light emitting devices with carbon nanotubes as cathode and anode. *Applied Physics Letters*, 95(20):203304, 2009.

[26] S. Bae, H. Kim, Y. Lee, X. Xu, J.-S. Park, Y. Zheng, J. Balakrishnan, T. Lei, H. R. Kim, Y. I. Song, Y.-J. Kim, K. S. Kim, B. Özyilmaz, J.-H. Ahn, B. H. Hong, and S. Iijima. Roll-to-roll production of 30-inch graphene films for transparent electrodes. *Applied Physics Letters*, 5(8):574–578, 2010.

[27] F. Zhang, M. Johansson, M. R. Andersson, J. C. Hummelen, and O. Inganäs. Polymer photovoltaic cells with conducting polymer anodes. *Advanced Functional Materials*, 14(9):662–664, 2002.

[28] S.-I. Na, S.-S. Kim, J. Jo, and D.-Y. Kim. Efficient and flexible ITO-free organic solar cells using highly conductive polymer anodes. *Advanced Materials*, 20(21): 4061–4067, 2008.

[29] M. Zhang, S. Höfle, J. Czolk, A. Mertens, and A. Colsmann. All-solution processed transparent organic light emitting diodes. *Nanoscale*, 7:20009–20014, 2015.

[30] M. Reinhard, R. Eckstein, A. Slobodskyy, U. Lemmer, and A. Colsmann. Solution-processed polymer-silver nanowire top electrodes for inverted semi-transparent solar cells. *Organic Electronics*, 14(1):273–277, 2013.

[31] K. Walzer, B. Maennig, M. Pfeiffer, and K. Leo. Highly efficient organic devices based on electrically doped transport layers. *Chemical Reviews*, 107(4):1233–1271, 2007.

[32] A. Elschner. *PEDOT : Principles and applications of an intrinsically conductive polymer.* CRC Press, 2011.

[33] T.-W. Lee, Y. Chung, O. Kwon, and J.-J. Park. Self-organized gradient hole injection to improve the performance of polymer electroluminescent devices. *Advanced Functional Materials*, 17(3):390–396, 2007.

[34] S. Tokito, K. Noda, and Y. Taga. Metal oxides as a hole-injecting layer for an organic electroluminescent device. *Journal of Physics D: Applied Physics*, 29(11): 2750–2753, 1996.

[35] Y. Guo and J. Robertson. Origin of the high work function and high conductivity of moo3. *Applied Physics Letters*, 105(22):222110, 2014.

[36] A. Buckley. *Organic light-emitting diodes (OLEDs): Materials, devices and applications.* Woodhead Publishing, 2013.

[37] M. T. Greiner, L. Chai, M. G. Helander, W.-M. Tang, and Z.-H. Lu. Metal/metal-oxide interfaces: How metal contacts affect the work function and band structure of MoO_3. *Advanced Functional Materials*, 23(2):215–226, 2013.

[38] S. Höfle, H. Do, E. Mankel, M. Pfaff, Z. Zhang, D. Bahro, T. Mayer, W. Jaegermann, D. Gerthsen, C. Feldmann, U. Lemmer, and A. Colsmann. Molybdenum oxide anode buffer layers for solution processed, blue phosphorescent small molecule organic light emitting diodes. *Organic Electronics*, 14(7):1820–1824, 2013.

[39] S. Höfle, M. Bruns, S. Strässle, C. Feldmann, U. Lemmer, and A. Colsmann. Tungsten oxide buffer layers fabricated in an inert sol-gel process at room-temperature for blue organic light-emitting diodes. *Advanced Materials*, 25(30): 4113–4116, 2013.

[40] R. Ganesan and A. Gedanken. Synthesis of WO_3 nanoparticles using a biopolymer as a template for electrocatalytic hydrogen evolution. *Nanotechnology*, 19(2):025702, 2008.

[41] J. Meyer, R. Khalandovsky, P. Görrn, and A. Kahn. MoO_3 films spin-coated from a nanoparticle suspension for efficient hole-injection in organic electronics. *Advanced Materials*, 23(1):70–73, 2011.

[42] J. M. Ziebarth and M. D. McGehee. A theoretical and experimental investigation of light extraction from polymer light-emitting diodes. *Journal of Applied Physics*, 97(6), 2005.

[43] N. Tokmoldin, N. Griffiths, D. D. C. Bradley, and S. A. Hague. A hybrid inorganic-organic semiconductor light-emitting diode using ZrO_2 as an electron-injection layer. *Advanced Materials*, 21(34):3475–3478, 2009.

[44] C. Qiu, Z. Xie, H. Chen, M. Wong, and H. S. Kwok. Comparative study of metal or oxide capped indium-tin oxide anodes for organic light-emitting diodes. *Journal of Applied Physics*, 93(6):3253–3258, 2003.

[45] F. C. Chen, S. C. Chien, and Y. S. Chen. Single-layer triplet white polymer light-emitting diodes incorporating polymer oxides: Effect of charge trapping at phosphorescent dopants. *Applied Physics Letters*, 94(4):13–16, 2009.

[46] J. H. Burroughes, D. D. C. Bradley, A. R. Brown, R. N. Marks, K. Mackay, R. H. Friend, P. L. Burns, and A. B. Holmes. Light-emitting diodes based on conjugated polymers. *Nature*, 347(6293):539–541, 1990.

[47] A. Jolt Oostra, P. W M Blom, and J. J. Michels. Prevention of short circuits in solution-processed OLED devices. *Organic Electronics*, 15(6):1166–1172, 2014.

[48] G. E. Jabbour, B. Kippelen, N. R. Armstrong, and N. Peyghambarian. Aluminum based cathode structure for enhanced electron injection in electroluminescent organic devices. *Applied Physics Letters*, 73(9):1185–1187, 1998.

[49] B. Lüssem, M. Riede, and K. Leo. Doping of organic semiconductors. *physica status solidi (a)*, 210(1):9–43, 2013.

[50] M. Kröger, S. Hamwi, J. Meyer, T. Dobbertin, T. Riedl, W. Kowalsky, and H. H. Johannes. Temperature-independent field-induced charge separation at doped organic/organic interfaces: Experimental modeling of electrical properties. *Physical Review B - Condensed Matter and Materials Physics*, 75(23):1–8, 2007.

[51] S. Hamwi, J. Meyer, M. Kröger, T. Winkler, M. Witte, T. Riedl, A. Kahn, and W. Kowalsky. The role of transition metal oxides in chargegeneration layers for stacked organic light-emitting diodes. *Advanced Functional Materials*, 20(11): 1762–1766, 2010.

[52] S. Olthof, R. Meerheim, M. Schober, and K. Leo. Energy level alignment at the interfaces in a multilayer organic light-emitting diode structure. *Physical Review B - Condensed Matter and Materials Physics*, 79(24):1–7, 2009.

[53] M. T. Greiner, M. G. Helander, W. M. Tang, Z. B. Wang, J. Qiu, and Zheng H. Lu. Universal energy-level alignment of molecules on metal oxides. *Nature Materials*, 11(1):76–81, 2012.

[54] H. J. Bolink, E. Coronado, J. Orozco, and M. Sessolo. Efficient polymer light-emitting diode using air-stable metal oxides as electrodes. *Advanced Materials*, 21 (1):79–82, 2009.

[55] Y. Zhou, C. Fuentes-Hernandez, J. Shim, J. Meyer, A. J. Giordano, H. Li, P. Winget, T. Papadopoulos, H. Cheun, J. Kim, M. Fenoll, A. Dindar, W. Haske, E. Najafabadi, T. M. Khan, H. Sojoudi, S. Barlow, S. Graham, J.-L. Bredas, S. R. Marder, A. Kahn, and B. Kippelen. A universal method to produce low-work function electrodes for organic electronics. *Science*, 336(6079):327–332, 2012.

[56] S. W. Tsang. *Charge carrier transport and injection across organic heterojunctions.* PhD thesis, University of Toronto, 2009.

[57] H. Bässler. Charge transport in disordered organic photoconductors a monte carlo simulation study. *physica status solidi (b)*, 175(1):15–56, 1993.

[58] H. Park, D.-S. Shin, H.-S. Yu, and H.-B. Chae. Electron mobility in tris(8-hydroxyquinoline)aluminum (Alq$_3$) films by transient electroluminescence from single layer organic light emitting diodes. *Applied Physics Letters*, 90(20):202103, 2007.

[59] Z. Shen, P. Burrows, V. Bulovic, D. McCarty, M. Thompson, and S. Forrest. Temperature dependency of current transport and electroluminescence in vacuum deposited organic light emitting devices. *The Japan Society of Applied Physics*, 35-2 (3B):L401–L404, 1996.

[60] J. Staudigel, M. Stößel, F. Steuber, and J. Simmerer. A quantitative numerical model of multilayer vapor-deposited organic light emitting diodes. *Journal of Applied Physics*, 86(7):3895–3910, 1999.

[61] S. M. Sze and K. K. Ng. *Physics of semiconductor devices.* John Wiley & Sons, Inc., 2006.

[62] S. Höfle. *Flüssigprozessierte organische Tandem-Leuchtdioden.* PhD thesis, Karlsruhe Institute of Technology, 2015.

[63] S. D. Baranovskii. Theoretical description of charge transport in disordered organic semiconductors. *physica status solidi (b)*, 251(3):487–525, 2014.

[64] C. Tanase. *Unified charge transport in disordered organic field-effect transistors and light-emitting diodes.* PhD thesis, University of Groningen, 2005.

[65] T. Tsujimura. *OLED displays.* John Wiley & Sons, Inc., 2012.

[66] Vadim I. Adamovich, Steven R. Cordero, Peter I. Djurovich, Arnold Tamayo, Mark E. Thompson, Brian W. D'Andrade, and Stephen R. Forrest. New charge-carrier blocking materials for high efficiency OLEDs. *Organic Electronics*, 4(2-3): 77–87, 2003.

[67] M. Ikai, S. Tokito, Y. Sakamoto, T. Suzuki, and Y. Taga. Highly efficient phosphorescence from organic light-emitting devices with an exciton-block layer. *Applied Physics Letters*, 79(2):156–158, 2001.

[68] D. F. O'Brien, M. A. Baldo, M. E. Thompson, and S. R. Forrest. Improved energy transfer in electrophosphorescent devices. *Applied Physics Letters*, 74(3):442–444, 1999.

[69] S. Reineke, M. Thomschke, B. Lüssem, and K. Leo. White organic light-emitting diodes: Status and perspective. 85, 2013.

[70] H. Choukri, A. Fischer, S. Forget, S. Chénais, M.-C. Castex, D. Adès, A. Siove, and B. Geffroy. White organic light-emitting diodes with fine chromaticity tuning via ultrathin layer position shifting. *Applied Physics Letters*, 89(18):183513, 2006.

[71] Y.-C. Tsai and J.-H. Jou. Long-lifetime, high-efficiency white organic light-emitting diodes with mixed host composing double emission layers. *Applied Physics Letters*, 89(24):243521, 2006.

[72] M. A. Baldo, S. R. Forrest, D. F. O 'Brien, Y. You, A. Shoustikov, S. Sibley, M. E. Thompson, and S. R. Forrest. Highly efficient phosphorescent emission from organic electroluminescent devices. *Nature*, 395:151–154, 1998.

[73] M. A. Baldo, M. E. Thompson, and S. R. Forrest. High-efficiency fluorescent organic light-emitting devices using a phosphorescent sensitizer. *Nature*, 403(6771):750–753, 2000.

[74] H. Yersin. *Highly efficient OLEDs with phosphorescent materials*. Wiley-VCH Verlag GmbH & Co. KGaA, 2008.

[75] S. Reineke, K. Walzer, and K. Leo. Triplet-exciton quenching in organic phosphorescent light-emitting diodes with Ir-based emitters. *Physical Review B - Condensed Matter and Materials Physics*, 75(12):1–13, 2007.

[76] H. Sasabe, N. Toyota, H. Nakanishi, T. Ishizaka, Y.-J. Pu, and J. Kido. 3,3-bicarbazole-based host materials for high-efficiency blue phosphorescent OLEDs with extremely low driving voltage. *Advanced Materials*, 24(24):3212–3217, 2012.

[77] G. He, M. Pfeiffer, K. Leo, M. Hofmann, J. Birnstock, R. Pudzich, and J. Salbeck. High-efficiency and low-voltage p-i-n electrophosphorescent organic light-emitting diodes with double-emission layers. *Applied Physics Letters*, 85(17):3911–3913, 2004.

[78] K.-H. Kim and J.-J. Kim. Highly efficient OLEDs using exciplex hosts. *Society for Information Display*, 48:746–749, 2017.

[79] Y. Seino, H. Sasabe, Y. J. Pu, and J. Kido. High-performance blue phosphorescent OLEDs using energy transfer from exciplex. *Advanced Materials*, 26(10):1612–1616, 2014.

[80] Y. S. Park, S. Lee, K. H. Kim, S. Y. Kim, J. H. Lee, and J. J. Kim. Exciplex-forming co-host for organic light-emitting diodes with ultimate efficiency. *Advanced Functional Materials*, 23(39):4914–4920, 2013.

[81] Z. Yang, Z. Mao, Z. Xie, Y. Zhang, S. Liu, J. Zhao, J. Xu, Z. Chi, and M. P. Aldred. Recent advances in organic thermally activated delayed fluorescence materials. *Chemical Society Reviews*, 46(3):915–1016, 2017.

[82] H. Tanaka, K. Shizu, H. Miyazaki, and C. Adachi. Efficient green thermally activated delayed fluorescence (TADF) from a phenoxazine–triphenyltriazine (PXZ–TRZ) derivative. *Chemical Communications*, 48(93):11392–11394, 2012.

[83] Y. Tao, K. Yuan, T. Chen, P. Xu, H. Li, R. Chen, C. Zheng, L. Zhang, and W. Huang. Thermally activated delayed fluorescence materials towards the breakthrough of organoelectronics. *Advanced Materials*, 26(47):7931–7958, 2014.

[84] K. Shizu, Y. Sakai, H. Tanaka, S. Hirata, C. Adachi, and H. Kaji. Meta-linking strategy for thermally activated delayed fluorescence emitters with a small singlet-triplet energy gap. *ITE Transactions on Media Technology and Applications*, 3(2): 108–113, 2015.

[85] H. Uoyama, K. Goushi, K. Shizu, H. Nomura, and C. Adachi. Highly efficient organic light-emitting diodes from delayed fluorescence. *Nature*, 492(7428):234–238, 2012.

[86] M. Y. Wong and E. Zysman-Colman. Purely organic thermally activated delayed fluorescence materials for organic light-emitting diodes. *Advanced Materials*, 29(22): 1605444, 2017.

[87] L. Bergmann, G. J. Hedley, T. Baumann, S. Bräse, and I. D. W. Samuel. Direct observation of intersystem crossing in a thermally activated delayed fluorescence copper complex in the solid state. *Science Advances*, 2(1):e1500889, 2016.

[88] Y. J. Cho, K. S. Yook, and J. Y. Lee. High efficiency in a solution-processed thermally activated delayed-fluorescence device using a delayed-fluorescence emitting material with improved solubility. *Advanced Materials*, 26(38):6642–6646, 2014.

[89] Q. Zhang, D. Tsang, H. Kuwabara, Y. Hatae, B. Li, T. Takahashi, S. Y. Lee, T. Yasuda, and C. Adachi. Nearly 100% internal quantum efficiency in undoped electroluminescent devices employing pure organic emitters. *Advanced Materials*, 27(12):2096–2100, 2015.

[90] S. Y. Lee, T. Yasuda, Y. S. Yang, Q. Zhang, and C. Adachi. Luminous butterflies: Efficient exciton harvesting by benzophenone derivatives for full-color delayed fluorescence OLEDs. *Angewandte Chemie International Edition*, 53(25):6402–6406, 2014.

[91] S. E. Braslavsky, E. Fron, H. B. Rodriguez, E. S. Roman, Gr. D. Scholes, G. Schweitzer, B. Valeur, and J. Wirz. Pitfalls and limitations in the practical use of Förster's theory of resonance energy transfer. *Photochemical & Photobiological Sciences*, 7:1444–1448, 2008. doi: 10.1039/B810620G.

[92] M. Klessinger and J. Michl. *Excited states and photochemistry of organic molecules.* Wiley-VCH, 1995.

[93] M. Ishii and Y. Taga. Influence of temperature and drive current on degradation mechanisms in organic light-emitting diodes. *Applied Physics Letters*, 80(18): 3430–3432, 2002.

[94] L. Ke, S.-J. Chua, K. Zhang, and N. Yakovlev. Degradation and failure of organic light-emitting devices. *Applied Physics Letters*, 80(12):2195–2197, 2002.

[95] R. Meerheim, K. Walzer, M. Pfeiffer, and K. Leo. Ultrastable and efficient red organic light emitting diodes with doped transport layers. *Applied Physics Letters*, 89(6):061111, 2006.

[96] L.S. Liao, W.K. Slusarek, T.K. Hatwar, M.L. Ricks, and D.L. Comfort. Tandem organic light-emitting diode using hexaazatriphenylene hexacarbonitrile in the intermediate connector. *Advanced Materials*, 20(2):324–329, 2008.

[97] Y. Zhang, J. Lee, and S. R. Forrest. Tenfold increase in the lifetime of blue phosphorescent organic light-emitting diodes. *Nature Communications*, 5(5008): 1–7, 2014.

[98] T. Chiba, Y. J. Pu, and J. Kido. Organic light-emitting devices with tandem structure. *Topics in Current Chemistry*, 374(3):1–17, 2016.

[99] J. Birnstock, G. He, S. Murano, A. Werner, and O. Zeika. White stacked OLED with 35 lm/W and 100,000 hours lifetime at 1000 cd/m^2 for display and lighting applications. *SID Symposium Digest of Technical Papers*, 39(1):822–825, 2008.

[100] T. Tsutsui and M. Terai. Electric field-assisted bipolar charge spouting in organic thin-film diodes. *Applied Physics Letters*, 84(3):440–442, 2004.

[101] M. Kröger, S. Hamwi, J. Meyer, T. Riedl, W. Kowalsky, and A. Kahn. Role of the deep-lying electronic states of MoO_3 in the enhancement of hole-injection in organic thin films. *Applied Physics Letters*, 95(12), 2009.

[102] J. Meyer, M. Kröger, S. Hamwi, F. Gnam, T. Riedl, W. Kowalsky, and A. Kahn. Charge generation layers comprising transition metal-oxide/organic interfaces: Electronic structure and charge generation mechanism. *Applied Physics Letters*, 96(19):193302, 2010.

[103] J. Liu, S. Huang, X. Shi, X. Wu, J. Wang, and G. He. Charge separation process in an ultrathin electron-injecting bilayer-assisted charge generation unit for tandem organic light-emitting diodes. *The Journal of Physical Chemistry C*, 117(27): 13887–13893, 2013.

[104] J. X. Sun, X. L. Zhu, H. J. Peng, M. Wong, and H. S. Kwok. Effective intermediate layers for highly efficient stacked organic light-emitting devices. *Applied Physics Letters*, 87(9):093504, 2005.

[105] H. Zhang, Y. Dai, and D. Ma. High efficiency tandem organic light-emitting devices with $Al/WO_3/Au$ interconnecting layer. *Applied Physics Letters*, 91(12):123504, 2007.

[106] H.M. Zhang, Wallace C.H. Choy, Y.F. Dai, and D.G. Ma. The structural composite effect of $Au–WO_3–Al$ interconnecting electrode on performance of each unit in stacked oleds. *Organic Electronics*, 10(3):402 – 407, 2009.

[107] C. Murawski, K. Leo, and M. C. Gather. Efficiency roll-off in organic light-emitting diodes. *Advanced Materials*, 25(47):6801–6827, 2013.

[108] A. Köhler and H. Bässler. Triplet states in organic semiconductors. *Materials Science and Engineering: R: Reports*, 66(4):71 – 109, 2009.

[109] B. H. Wallikewitz, D. Kabra, S. Gélinas, and R. H. Friend. Triplet dynamics in fluorescent polymer light-emitting diodes. *Physical Review B*, 85:045209, 2012.

[110] E. J. W. List, C.-H. Kim, A. K. Naik, U. Scherf, G. Leising, W. Graupner, and J. Shinar. Interaction of singlet excitons with polarons in wide band-gap organic semiconductors: A quantitative study. *Physical Review B*, 64:155204, 2001.

[111] M. A. Baldo, R. J. Holmes, and S. R. Forrest. Prospects for electrically pumped organic lasers. *Physical Review B*, 66:035321, 2002.

[112] W. Brütting, J. Frischeisen, T. D. Schmidt, B. J. Scholz, and C. Mayr. Device efficiency of organic light-emitting diodes: Progress by improved light outcoupling. *physica status solidi (a)*, 210(1):44–65, 2013.

[113] K. Saxena, V.K. Jain, and D. S. Mehta. A review on the light extraction techniques in organic electroluminescent devices. *Optical Materials*, 32(1):221 – 233, 2009.

[114] P. A. Hobson, J. A. E. Wasey, I. Sage, and W. L. Barnes. The role of surface plasmons in organic light-emitting diodes. *IEEE Journal of Selected Topics in Quantum Electronics*, 8(2):378–386, 2002. doi: 10.1109/2944.999193.

[115] Light and vision, http://www.prismalenceuk.com, February 2018.

[116] CIE 1931 color space, https://en.wikipedia.org, February 2018.

[117] CIE 1931 color space, https://en.wikipedia.org, February 2018.

[118] W. D. Wright. A re-determination of the trichromatic coefficients of the spectral colours. *Transactions of the Optical Society*, 30(4):141–164, 1929.

[119] The colorimetric properties of the spectrum. *Philosophical Transactions of the Royal Society of London A: Mathematical, Physical and Engineering Sciences*, 230(681-693):149–187, 1931.

[120] K. Norrman, A. Ghanbari-Siahkali, and N. B. Larsen. 6 Studies of spin-coated polymer films. *Annual Reports Section "C" (Physical Chemistry)*, 101:174–201, 2005.

[121] F. C. Krebs. Fabrication and processing of polymer solar cells: A review of printing and coating techniques. *Solar Energy Materials and Solar Cells*, 93(4):394–412, 2009.

[122] L. D. Landau and V. G. Levich. Dragging of a liquid by a moving plate. *Acta Physicochimica URSS*, 17:42–54, 1942.

[123] S. Höfle, T. Lutz, A. Egel, F. Nickel, S. W. Kettlitz, G. Gomard, U. Lemmer, and A. Colsmann. Influence of the emission layer thickness on the optoelectronic properties of solution processed organic light-emitting diodes. *ACS Photonics*, 1 (10):968–973, 2014.

[124] Bruker Corporation. *AFM Probes*. 2013.

[125] V. Palermo, M. Palma, and P. Samori. Electronic characterization of organic thin films by Kelvin probe force microscopy. *Advanced Materials*, 18(2):145–164, 2006.

[126] H. Ago, Th Kugler, F. Cacialli, K. Petritsch, R. H. Friend, W. R. Salaneck, Y. Ono, T. Yamabe, and K. Tanaka. Workfunction of purified and oxidised carbon nanotubes. *Synthetic Metals*, 103(1-3):2494–2495, 1999.

[127] T. Pan and L. Sun. Sub-microscopic phenomena of metallic corrosion studied by a combined photoelectron spectroscopy in air (PESA) and scanning Kelvin probe force microscopy (SKPFM) approach. *International Journal of Electrochemical Science*, 7(10):9325–9344, 2012.

[128] A. Colsmann. *Ladungstransportschichten für effiziente organische Halbleiterbauelemente.* PhD thesis, Karlsruhe Institute of Technology, 2008.

[129] C. A. Parker and C. G. Hatchard. Triplet-singlet emission in fluid solutions. Phosphorescence of eosin. *Transactions of the Faraday Society*, 57:1894–1904, 1961. doi: 10.1039/TF9615701894.

[130] M. N. Berberan-Santos and J. M. M. Garcia. Unusually strong delayed fluorescence of C_{70}. *Journal of the American Chemical Society*, 118(39):9391–9394, 1996.

[131] J. R. Kirchhoff, R. E. Gamache, M. W. Blaskie, A. A. Del Paggio, R. K. Lengel, and D. R. McMillin. Temperature dependence of luminescence from $Cu(NN)_2^+$ systems in fluid solution. Evidence for the participation of two excited states. *Inorganic Chemistry*, 22(17):2380–2384, 1983.

[132] A. Endo, M. Ogasawara, A. Takahashi, D. Yokoyama, Y. Kato, and C. Adachi. Thermally activated delayed fluorescence from Sn^{4+}-porphyrin complexes and their application to organic light emitting diodes - A novel mechanism for electroluminescence. *Advanced Materials*, 21(47):4802–4806, 2009.

[133] A. Endo, K. Sato, K. Yoshimura, T. Kai, A. Kawada, H. Miyazaki, and C. Adachi. Efficient up-conversion of triplet excitons into a singlet state and its application for organic light emitting diodes. *Applied Physics Letters*, 98(8):2009–2012, 2011.

[134] R. Komatsu, H. Sasabe, S. Inomata, Y. J. Pu, and J. Kido. High efficiency solution processed OLEDs using a thermally activated delayed fluorescence emitter. *Synthetic Metals*, 202:165–168, 2015.

[135] J.-H. Jou, W.-B. Wang, S.-Z. Chen, J.-J. Shyue, M.-F. H., C.-W. Lin, S.-M. Shen, C.-J. Wang, C.-P. Liu, C.-T. Chen, M.-F. Wu, and S.-W. Liu. High-efficiency blue

organic light-emitting diodes using a 3,5-di(9H-carbazol-9-yl)tetraphenylsilane host via a solution-process. *Journal of Materials Chemistry*, 20(38):8411, 2010.

[136] Y. Seino, S. Inomata, H. Sasabe, Y. J. Pu, and J. Kido. High-performance green OLEDs using thermally activated delayed fluorescence with a power efficiency of over 100 lm W^{-1}. *Advanced Materials*, 28(13):2638–2643, 2016.

[137] J. W. Sun, J. H. Lee, C. K. Moon, K. H. Kim, H. Shin, and J. J. Kim. A fluorescent organic light-emitting diode with 30% external quantum efficiency. *Advanced Materials*, 26(32):5684–5688, 2014.

[138] Y. Tao, C. Yang, and J. Qin. Organic host materials for phosphorescent organic light-emitting diodes. *Chemical Society Reviews*, 40:2943–2970, 2011.

[139] T. Chiba, Y. J. Pu, and J. Kido. Solution-processed white phosphorescent tandem organic light-emitting devices. *Advanced Materials*, 27(32):4681–4687, 2015.

[140] C. Cai, S.-J. Su, T. Chiba, H. Sasabe, Y.-J. Pu, K. Nakayama, and J. Kido. High-efficiency red, green and blue phosphorescent homojunction organic light-emitting diodes based on bipolar host materials. *Organic Electronics*, 12(5):843 – 850, 2011.

[141] S.-J. Su, H. Sasabe, T. Takeda, and J. Kido. Pyridine-containing bipolar host materials for highly efficient blue phosphorescent OLEDs. *Chemistry of Materials*, 20(5):1691–1693, 2008.

[142] J. C. Deaton, S. C. Switalski, D. Y. Kondakov, R. H. Young, T. D. Pawlik, D. J. Giesen, S. B. Harkins, A. J. M. Miller, S. F. Mickenberg, and J. C. Peters. E-type delayed fluorescence of a phosphine-supported $Cu_2(\mu$-$NAr_2)_2$ diamond core: Harvesting singlet and triplet excitons in OLEDs. *Journal of the American Chemical Society*, 132(27):9499–9508, 2010.

[143] H. Yersin, A. F. Rausch, R. Czerwieniec, T. Hofbeck, and T. Fischer. The triplet state of organo-transition metal compounds. Triplet harvesting and singlet harvesting for efficient OLEDs. *Coordination Chemistry Reviews*, 255(21):2622 – 2652, 2011.

[144] L. Bergmann, J. Friedrichs, M. Mydlak, T. Baumann, M. Nieger, and S. Brase. Outstanding luminescence from neutral copper(I) complexes with pyridyl-tetrazolate and phosphine ligands. *Chemical Communications*, 49:6501–6503, 2013.

[145] L. Duan, L. Hou, T.-W. Lee, J. Qiao, D. Zhang, G. Dong, L. Wang, and Y. Qiu. Solution processable small molecules for organic light-emitting diodes. *Journal of Materials Chemistry*, 20(31):6392–6407, 2010.

[146] M. Wallesch, C. Verma, A.and Fléchon, H. Flügge, D. M. Zink, S. M. Seifermann, J. M. Navarro, T. Vitova, J. Göttlicher, R. Steininger, L. Weinhardt, M. Zimmer, M. Gerhards, C. Heske, S. Bräse, T. Baumann, and D. Volz. Towards printed organic light-emitting devices: A solution-stable, highly soluble cui–nhetphos. *Chemistry – A European Journal*, 22(46):16400–16405, 2016.

[147] D. M. Zink, M. Bächle, T. Baumann, M. Nieger, M. Kühn, Wang. C., W. Klopper, U. Monkowius, T. Hofbeck, H. Yersin, and S. Bräse. Synthesis, structure, and characterization of dinuclear copper (I) halide complexes with P^N ligands featuring exciting photoluminescence properties. *Inorganic Chemistry*, 52(I):2292–2305, 2012.

[148] D. Volz, D. M. Zink, T. Bocksrocker, J. Friedrichs, M. Nieger, T. Baumann, U. Lemmer, and S. Bräse. Molecular construction kit for tuning solubility, stability and luminescence properties: Heteroleptic MePyrPHOS-copper iodide-complexes and their application in organic light-emitting diodes. *Chemistry of Materials*, 25 (17):3414–3426, 2013.

[149] C. Adachi, M. A. Baldo, M. E. Thompson, and S. R. Forrest. Nearly 100% internal phosphorescence efficiency in an organic light emitting device. *Journal of Applied Physics*, 90(10):5048–5051, 2001.

[150] M. Cocchi, J. Kalinowski, L. Murphy, J. A G. Williams, and V. Fattori. Mixing of molecular exciton and excimer phosphorescence to tune color and efficiency of organic LEDs. *Organic Electronics*, 11(3):388–396, 2010.

[151] S. H. Rhee, K. b. Nam, C. S. Kim, M. Song, W. Cho, S.-H. Jin, and S. Y. Ryu. Effect of electron mobility of the electron transport layer on fluorescent organic light-emitting diodes. *ECS Solid State Letters*, 3(5):R19–R22, 2014.

[152] L. S. Liao and K. P. Klubek. Power efficiency improvement in a tandem organic light-emitting diode. *Applied Physics Letters*, 92(22):2006–2009, 2008.

[153] B. Ma, B. J. Kim, D. A. Paulsen, S. J. Pastine, and J. M J Fréchet. Multifunctional crosslinkable iridium complexes as hole transporting/electron blocking and emitting materials for solution-processed multilayer organic light-emitting diodes. *Advanced Functional Materials*, 19(7):1024–1031, 2009.

[154] C. D. Müller, A. Falcou, N. Reckefuss, M. Rojahn, V. Wiederhirn, P. Rudati, H. Frohne, O. Nuyken, H. Becker, and K. Meerholz. Multi-colour organic light-emitting displays by solution processing. *Nature*, 421(6925):829–833, 2003.

[155] Y.-H. Niu, M. S. Liu, J.-W. Ka, and A. K.-Y. Jen. Thermally crosslinked hole-transporting layers for cascade hole-injection and effective electron-blocking/exciton-confinement in phosphorescent polymer light-emitting diodes. *Applied Physics Letters*, 88(9):093505, 2006.

[156] J. Zhao, J. A. Bardecker, A. M. Munro, M. S. Liu, Y. Niu, I-K. Ding, J. Luo, B. Chen, A. K.-Y. Jen, and D. S. Ginger. Efficient CdSe/CdS quantum dot light-emitting diodes using a thermally polymerized hole transport layer. *Nano Letters*, 6(3):463–467, 2006. PMID: 16522043.

[157] F. R. P. Limberg, T. Schneider, S. Höfle, F. Reisbeck, S. Janietz, A. Colsmann, and H. Krüger. 1-Ethynyl ethers as efficient thermal crosslinking system for hole transport materials in OLEDs. *Advanced Functional Materials*, 26(46):8505–8513, 2016.

[158] S. Höfle, A. Schienle, C. Bernhard, M. Bruns, U. Lemmer, and A. Colsmann. Solution processed, white emitting tandem organic light-emitting diodes with inverted device architecture. *Advanced Materials*, 26(30):5155–5159, 2014.

[159] C.-P. Chen, Y.-D. Chen, and S.-C. Chuang. High-performance and highly durable inverted organic photovoltaics embedding solution-processable vanadium oxides as an interfacial hole-transporting layer. *Advanced Materials*, 23(33):3859–3863, 2011.

[160] K. Zilberberg, S. Trost, H. Schmidt, and T. Riedl. Solution processed vanadium pentoxide as charge extraction layer for organic solar cells. *Advanced Energy Materials*, 1(3):377–381, 2011.

[161] J. Yang, R. Zhu, Z. Hong, Y. He, A. Kumar, Y. Li, and Y. Yang. A robust inter-connecting layer for achieving high performance tandem polymer solar cells. *Advanced Materials*, 23(30):3465–3470, 2011.

[162] S. Höfle, C. Bernhard, M. Bruns, C. Kübel, T. Scherer, U. Lemmer, and A. Colsmann. Charge generation layers for solution processed tandem organic light emitting diodes with regular device architecture. *ACS Applied Materials and Interfaces*, 7(15):8132–8137, 2015.

[163] Y. J. Pu, T. Chiba, K. Ideta, S. Takahashi, N. Aizawa, T. Hikichi, and J. Kido. Fabrication of organic light-emitting devices comprising stacked light-emitting units by solution-based processes. *Advanced Materials*, 27(8):1327–1332, 2015.

[164] J. Chen, C. Shi, Q. Fu, F. Zhao, Y. Hu, Y. Feng, and D. Ma. Solution-processable small molecules as efficient universal bipolar host for blue, green and red

phosphorescent inverted OLEDs. *Journal of Materials Chemistry*, 22(11):5164–5170, 2012.

[165] H. Sasabe and J. Kido. Development of high performance OLEDs for general lighting. *Journal of Materials Chemistry C*, 1(9):1699–1707, 2013.

[166] M. Wallesch, D. Volz, D. M. Zink, U. Schepers, M. Nieger, T. Baumann, and S. Bräse. Bright coppertunities: Multinuclear CuI complexes with N–P ligands and their applications. *Chemistry – A European Journal*, 20(22):6578–6590, 2014.

[167] T. Chiba, Y. J. Pu, M. Hirasawa, A. Masuhara, H. Sasabe, and J. Kido. Solution-processed inorganic-organic hybrid electron injection layer for polymer light-emitting devices. *ACS Applied Materials and Interfaces*, 4(11):6104–6108, 2012.

[168] J. Park, T. Park, W. Jeon, R. Pode, J. Jang, J. Kwon, E. Yu, and M. Chae. Small molecule interlayer for solution processed phosphorescent organic light emitting device. *Organic Electronics*, 10(1):189–193, 2009.

[169] H. J. Bolink, H. Brine, E. Coronado, and M. Sessolo. Phosphorescent hybrid organic-inorganic light-emitting diodes. *Advanced Materials*, 22(19):2198–2201, 2010.

[170] S. Sax, N. Rugen-Penkalla, A. Neuhold, S. Schuh, E. Zojer, E. J W List, and K. Müllen. Efficient blue-light-emitting polymer heterostructure devices: The fabrication of multilayer structures from orthogonal solvents. *Advanced Materials*, 22(18):2087–2091, 2010.

[171] M. Reinhard, J. Hanisch, Z. Zhang, E. Ahlswede, A. Colsmann, and U. Lemmer. Inverted organic solar cells comprising a solution-processed cesium fluoride interlayer. *Applied Physics Letters*, 98(5):8–11, 2011.

[172] F. So, B. Krummacher, M. K. Mathai, D. Poplavskyy, S. A. Choulis, and V. E. Choong. Recent progress in solution processable organic light emitting devices. *Journal of Applied Physics*, 102(9):091101, 2007.

[173] B. C. Krummacher, V.-E. Choong, M. K. Mathai, S. A. Choulis, F. So, F. Jermann, T. Fiedler, and M. Zachau. Highly efficient white organic light-emitting diode. *Applied Physics Letters*, 88(11):113506, 2006.

[174] J. Huang, G. Li, and Y. Yang. A semi-transparent plastic solar cell fabricated by a lamination process. *Advanced Materials*, 20(3):415–419, 2008.

[175] M. C. Gather, R. Jin, J. de Mello, D. D. C. Bradley, and K. Meerholz. Highly-efficient solution-processed phosphorescent multi-layer organic light-emitting diodes investigated by electromodulation spectroscopy. *Applied Physics B*, 95(1):113–124, 2009. doi: 10.1007/s00340-009-3364-8.

[176] F. Zhao, Z. Zhang, Y. Liu, Y. Dai, J. Chen, and D. Ma. A hybrid white organic light-emitting diode with stable color and reduced efficiency roll-off by using a bipolar charge carrier switch. *Organic Electronics*, 13(6):1049–1055, 2012.

[177] P. Zacharias, M. C. Gather, M. Rojahn, O. Nuyken, and K. Meerholz. New crosslinkable hole conductors for blue-phosphorescent organic light-emitting diodes. *Angewandte Chemie - International Edition*, 46(23):4388–4392, 2007.

[178] Q. Zhang, T. Komino, S. Huang, S. Matsunami, K. Goushi, and C. Adachi. Triplet exciton confinement in green organic light-emitting diodes containing luminescent charge-transfer Cu(I) complexes. *Advanced Functional Materials*, 22(11):2327–2336, 2012.

[179] S. Burns, J. Macleod, T. Trang Do, P. Sonar, and S. D. Yambem. Effect of thermal annealing Super Yellow emissive layer on efficiency of OLEDs. *Scientific Reports*, 7:1–8, 2017.

[180] G. Zhou, W.-Y. Wong, and S. Suo. Recent progress and current challenges in phosphorescent white organic light-emitting diodes (WOLEDs). *Journal of Photochemistry and Photobiology C: Photochemistry Reviews*, 11(4):133–156, 2010.

[181] S. R. Tseng, Y. S. Chen, H. F. Meng, H. C. Lai, C. H. Yeh, S. F. Horng, H. H. Liao, and C. S. Hsu. Electron transport and electroluminescent efficiency of conjugated polymers. *Synthetic Metals*, 159(1-2):137–141, 2009.

[182] H. C. Chen, S. W. Lin, J. M. Jiang, Y. W. Su, and K. H. Wei. Solution-processed zinc oxide/polyethylenimine nanocomposites as tunable electron transport layers for highly efficient bulk heterojunction polymer solar cells. *ACS Applied Materials and Interfaces*, 7(11):6273–6281, 2015.

[183] M. Cai, Z. Ye, T. Xiao, R. Liu, Y. Chen, R. W. Mayer, R. Biswas, K. M. Ho, R. Shinar, and J. Shinar. Extremely efficient indium-tin-oxide-free green phosphorescent organic light-emitting diodes. *Advanced Materials*, 24(31): 4337–4342, 2012.

[184] A. Colsmann, M. Reinhard, T. H. Kwon, C. Kayser, F. Nickel, J. Czolk, U. Lemmer, N. Clark, J. Jasieniak, A. B. Holmes, and D. Jones. Inverted semi-transparent

organic solar cells with spray coated, surfactant free polymer top-electrodes. *Solar Energy Materials and Solar Cells*, 98:118–123, 2012.

[185] J. Czolk, D. Landerer, M. Koppitz, D. Nass, and A. Colsmann. Highly efficient, mechanically flexible, semi-transparent organic solar cells doctor bladed from non-halogenated solvents. *Advanced Materials Technologies*, 1(9):1600184, 2016.

[186] J. Huang, P. F. Miller, J. S. Wilson, A. J. De Mello, J. C. De Mello, and D. D C Bradley. Investigation of the effects of doping and post-deposition treatments on the conductivity, morphology, and work function of poly(3,4-ethylenedioxythiophene)/poly(styrene sulfonate) films. *Advanced Functional Materials*, 15(2):290–296, 2005.

[187] S. Jeong, S.-H. Woo, T.-H. Han, M-H. Park, H. Cho, Y.-H. Kim, H. Cho, H. Kim, S. Yoo, and T.-W. Lee. Universal high work function flexible anode for simplified ITO-free organic and perovskite light-emitting diodes with ultra-high efficiency. *NPG Asia Materials*, 9:e411, 2017.

List of Figures

List of Tables

Publication List

Articles in peer reviewed journals

M. Zhang, S.Höfle, J. Czolk, A. Mertens, and A. Colsmann, All-solution processed transparent organic light emitting diodes. *Nanoscale*, 7(47):20009-14, 2015. doi: 10.1039/c5nr05820a.

S. Höfle, **M. Zhang**, J. Dlugosch, M. Kuhn, M. Hamburger, and A Colsmann, Thermo-cleavable poly(fluorene-benzothiadiazole) to enable solution deposition of multi-layer organic light emitting diodes. *Organic Electronics*, 42, 355-360, 2017. doi: 10.1016/j.orgel.2016.12.060.

J. Fragoso, S.Höfle, **M. Zhang**, J. Dlugosch, T. Friedrich, S. Wager and A. Colsmann. OLED Luminaires: device arrays with 99.6% geometric fill factor structured by femtosecond laser ablation, *ACS Applied Materials & Interfaces*, 9(43):37898-37904, 2017. doi: 10.1021/acsami.7b12356.

Stefan Höfle, **M. Zhang**, N. A. Luechinger, D. Volz, B. Hartmeier, M. Schlichting, O. Falke, U. Lemmer, A. Colsmann, Universal Method to Fabricate all Solution Processed Charge Generation Layers for Highly Efficient Tandem Organic Light Emitting Diodes, *Nature Photonics*, submitted.

M. Zhang, S. Höfle, S. Gärtner, Q. Jin, C. Bremauer, T. Leonhard and A. Colsmann, Solution processable cesium fluoride for highly efficient inverted OLEDs, in preparation.

M. Zhang, K. Fischer, M. Bruns and A. Colsmann, All-solution processed transparent OLEDs on flexible substrate, in preparation.

Presentations at international conferences

M. Zhang, S.Höfle, and A. Colsmann. All solution processed transparent OLEDs, *International Symposium on flexible Organic Electronics*, Thessaloniki, Greece, 2015.

M. Zhang, S.Höfle, and A. Colsmann. Universal charge generation layer for solution processed OLEDs, *Large-area, Organic and Printed Electronics Convention (LOPEC)*, Munich, Germany, 2017.

Supervised Theses

Karen Fischer, Druckbare, transparente organische Leuchtdioden auf mechanisch flexiblen Substraten, Master thesis, Department of Electrical Engineering and Information Technology, 2018

Oliver Falke, Kupferiodid-basierte TADF-Emitter für flüssigprozessierte organische Leuchtdioden, Bachelor thesis, Department of Electrical Engineering and Information Technology, 2016

Yannick Luck, Herstellung von OLEDs aus niedermolekularen Verbindungen für flüssigprozessierte Tandemarchitekturen, Master Thesis, Department of Electrical Engineering and Information Technology, 2016

Qihao Jin, Solution-processed red phosphorescent organic light-emitting devices, Master Thesis, Karlsruhe School of Optics and Photonics (KSOP), 2015

Matthias Mitlacher, Herstellung flüssigprozessierter phosphoreszierender weißer OLEDs, Bachelor thesis, Department of Electrical Engineering and Information Technology, 2015

Christian Bremauer, Rot phosphoreszierende, flüssigprozessierte OLEDs mit invertierter Bauelement-Architektur, Bachelor thesis, Department of Electrical Engineering and Information Technology, 2015

Acknowledgements